ORNL/Sub/90-SF521/05

Final Report

Investigation of Moisture-Induced Embrittlement of Iron Aluminides

June 5, 1997

Research sponsored by the U. S. Department of Energy
Office of Fossil Energy
Advanced Research and Technology Development Materials Program

Report Prepared by
D. A. Alven and N. S. Stoloff
Rensselaer Polytechnic Institute
Materials Engineering Department
Troy, NY 12180-3590

under
19X-SF521C, WBS Element RPI-2

for

OAK RIDGE NATIONAL LABORATORY
Oak Ridge, Tennessee 37831
Managed by
LOCKHEED MARTIN ENERGY RESEARCH CORP.
for the
U. S. DEPARTMENT OF ENERGY
under contract DE-AC05-95OR22464

ORNL/Sub/90-SF521/05

Final Report

Investigation of Moisture-Induced Embrittlement of Iron Aluminides

June 5, 1997

Research sponsored by the U. S. Department of Energy
Office of Fossil Energy
Advanced Research and Technology Development Materials Program

Report Prepared by
D. A. Alven and N. S. Stoloff
Rensselaer Polytechnic Institute
Materials Engineering Department
Troy, NY 12180-3590

under
19X-SF521C, WBS Element RPI-2

for

OAK RIDGE NATIONAL LABORATORY
Oak Ridge, Tennessee 37831
Managed by
LOCKHEED MARTIN ENERGY RESEARCH CORP.
for the
U. S. DEPARTMENT OF ENERGY
under contract DE-AC05-95OR22464

Research sponsored by the U. S. Department of Energy, Fossil Energy Advanced Research and Technology Development Materials Program, DOE/FE AA 15 10 10 0, Work Breakdown Structure Element RPI-2

ABSTRACT

Iron-aluminum alloys with 28 at.% Al and 5 at.% Cr were shown to be susceptible to hydrogen embrittlement by exposure to both gaseous hydrogen and water vapor. This study examined the effect of the addition of zirconium (0.5 at.% and 1 at.%) and carbon (0.05 at.%) on the moisture-induced hydrogen embrittlement of an Fe_3Al,Cr alloy through the evaluation of tensile properties and fatigue crack growth resistance in hydrogen gas and moisture-bearing air. Susceptibility to embrittlement was found to vary with the zirconium content while the carbon addition was found to only affect the fracture toughness.

Inherent fatigue crack growth resistance and fracture toughness, as measured in an inert environment, was found to increase with the addition of 0.5 at.% Zr. The combined addition of 0.5 at.% Zr and carbon only increased the fracture toughness. The addition of 1 at.% Zr and carbon was found to have no effect on the crack growth rate when compared to the base alloy.

Susceptibility to embrittlement in moisture-bearing environments was found to decrease with the addition of 0.5 at.% Zr. In gaseous hydrogen, the threshold value of the Zr-containing alloys was found to increase above that found in the inert environment while the crack growth resistance was much lower. Increasing the moisture content in the test environment, from 21%rH to 81%rH, was found to have a small effect on the fatigue crack growth resistance of the Zr-containing alloys.

By varying the frequency of fatigue loading, it was shown that the corrosion fatigue component of the fatigue crack growth rate in an embrittling environment

displays a frequency dependence. Hydrogen transport in iron aluminides was shown to occur primarily by a dislocation-assisted transport mechanism. This mechanism, in conjunction with fractography, indicates that the zirconium-containing precipitates act as traps for the hydrogen that is carried along by the dislocations through the lattice.

1 INTRODUCTION

The interest in iron aluminides began in the 1930's when alloys with more than 18 at.% Al were shown to have excellent corrosion resistance (1, 2). The combination of excellent oxidation resistance, low density, and low cost compared to competitive alloys have rekindled the interest in iron aluminides for applications at temperatures up to 500°C. The principal reason that iron aluminides have not been used to date is the poor ductility and fracture toughness of these alloys at ambient temperatures. Similar to many other intermetallics and steels, iron aluminides have been shown to be embrittled by water vapor and gaseous hydrogen, thereby lowering room temperature ductility (3, 4, 5). The primary embrittling mechanism involves the combination of fresh aluminum surfaces with water vapor in air. This reaction produces atomic hydrogen which has been shown to have a potent embrittling effect on many materials, including iron aluminides.

Through testing in inert atmospheres, it has been shown that Fe_3Al is intrinsically ductile (5). Fe_3Al alloys have also been shown to undergo (110) ‹111› type slip, which provides for at least 5 slip systems, fracture in a transgranular manner (6), and exhibit moderate yield and tensile strength. These are all properties associated with inherently ductile materials. Accompanying an understanding of the environmental embrittlement improved ductility has been shown to result from control of composition and microstructure (7, 8, 9). As a result of these findings, iron aluminides are again being considered for applications where their excellent corrosion resistance can be utilized.

The purpose of this research was to examine the effect of small amounts of zirconium and carbon on the environmental embrittlement of an Fe_3Al.Cr base intermetallic compound. Principally, the fatigue crack growth resistance and tensile

behavior of alloys with differing zirconium levels was examined in various environments. The resulting data are used to gain insight on the role of zirconium and carbon additions in decreasing the embrittlement of iron aluminides.

2 BACKGROUND

2.1 Intermetallics

2.1.1 Intermetallic Compounds

For use as structural materials in the next generation of gas turbines, intermetallic compounds must possess certain properties which include low density, high temperature strength, slow diffusion rates and excellent oxidation resistance, but room temperature properties and cost are also critical. Many intermetallic compounds possess a number of these properties, and, as such, have received considerable attention in the research and development community.

The aerospace and power generation industries are in need of materials that can withstand the higher temperatures necessary to increase the efficiency of turbines, requiring operating temperatures exceeding 1100°C. Intermetallic alloys, with their tendency to form ordered lattices, possess very high melting temperatures. The increase in yield stress with increasing temperature demonstrated in some intermetallics, as well as their ability to retain strength at temperatures in excess of half their melting temperature, further enhances their attractiveness for such applications.

Many intermetallics, such as aluminides and silicides, have low densities compared to steels and superalloys. The densities of various intermetallics range from 4 g/cc for Ti-Al to 7.3 g/cc for Co_3Ti which is considerable lower than most nickel-based superalloys such as Udimet 500 with a density of approximately 8 g/cc and the density of cobalt-base superalloys with densities in the range of 8-9 g/cc (10). Lower densities coupled with lower cost and significantly higher corrosion resistance due to alumina formation exhibited by aluminides makes them ideal for certain structural applications.

2.1.2 The Ordered Intermetallic Lattice

Intermetallic compounds are solid solution metallic compounds which due to their widely divergent electrochemical properties have a strong tendency to form ordered crystal structures upon cooling below a certain critical temperature, T_c. Above T_c, the alloys can either possess a different ordered structure or transform to a disordered state. Long range ordering occurs at or near specific atomic ratios (i.e., line compounds), for example, AB, A_2B, A_3B, AB_3, but can exist over a range of solubility.

The driving force for the order-disorder transformation is thermodynamic in nature. Below T_c, the interaction energy, W, is much larger than the thermal energy, kT, where k is Boltzmann's constant and T is the absolute temperature. The need to minimize W, which in turn will minimize the overall internal energy, drives the atomic ordering. The minimum internal energy configuration in ordering alloys results in the periodic alternation of different kinds of atoms.

The degree of order can be expressed by Eq. 1,

$$S=\frac{r_A-F_A}{1-F_A} \qquad \text{Eq. 1.}$$

where S is the order parameter, r_A is the fraction of A sites occupied by A atoms, and F_A is the fraction of A atoms in the alloy (11). When the long range order is perfect, then r_A =1 and S =1. For a completely disordered alloy, S=0 because $r_A=F_A$. Some alloys possess an ordered state at higher temperatures that can be retained by quenching to room temperature. In these alloys, such as Fe_3Al in the range of 27% to 35% Al, the order is rarely complete.

One common group of crystal structure types found in ordered intermetallics are BCC derivatives. Fe_3Al posses the BCC derivative DO_3 structure, while FeAl possess

the B2 structure. The atom configuration of the B2 and DO_3 unit cells are shown in Fig. 2.1 (a) and (b), respectively. The B2 unit cell consists of two interpenetrating simple cubic unit cells of A and B atoms. The DO_3 unit cell has four interpenetrating FCC unit cells with A atoms on the a, b and c sites and B atoms on the d sites.

2.1.3 Dislocations in the Ordered Lattice

When a unit dislocation moves through an ordered lattice it cannot recreate the order in its wake. Therefore it leaves behind an ordered lattice that is out of phase with the original lattice. When another unit dislocation of the same sign follows the first, the order is restored. The region between these two dislocations is called an anti-phase domain (APD) and two dislocations which make up the boundary between the APD's are referred to as anti-phase boundaries (APB). An example of a unit dislocation found in a B2 ordered lattice and the disorder caused by it is shown in Fig. 2.2.. This type of APB is referred to as a nearest-neighbor APB (NNAPB)

In the B2 lattice, the APD formed by paired dislocations is shown in Fig. 2.3. By the pairing of dislocations, the only disturbance in the order is a small ribbon between the dislocations. These pairs of dislocations are referred to as superlattice dislocations and require only a small energy increase for motion as compared to the energy that would be necessary to move a unit dislocation through an ordered lattice. The energy associated with APB's is proportional to the difference in interaction energies of A-B bonds and the average of A-A and B-B bonds. This APB energy determines the spacing of the two dislocations, and the energy decreases as the spacing increases.

APB's can also be formed during heat treatment. These thermal APB's separate regions that are perfectly ordered within themselves, but are out of phase with one

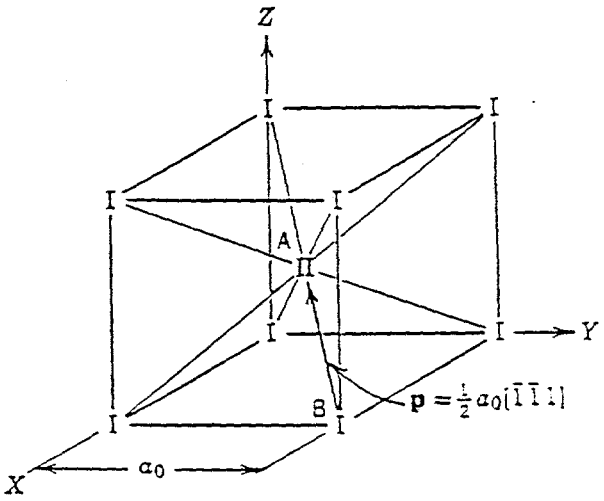

(a)

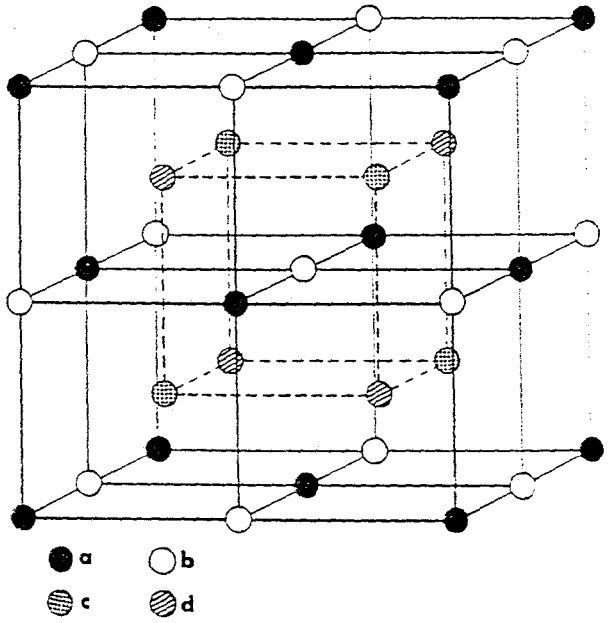

(b)

Fig. 2.1 Illustration of the (a) B2 and (b) DO_3 unit cells.

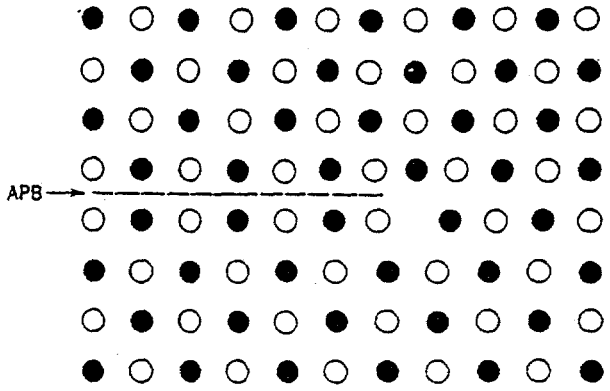

Fig. 2.2. Unit dislocation in an ordered lattice.

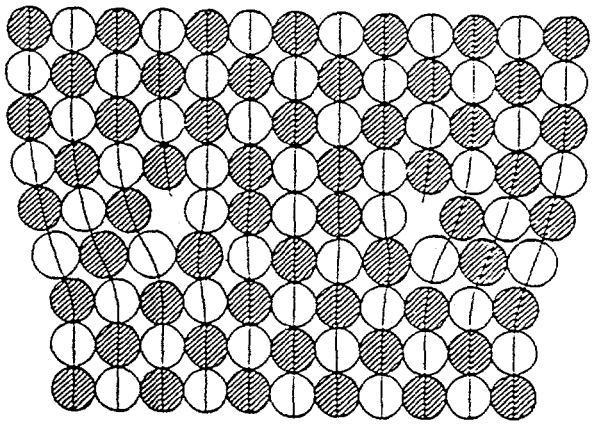

Fig. 2.3 Two-fold superlattice dislocation in a B2 ordered lattice.

another. During annealing, the thermal APB's can grow to a size limited only by the specimen size.

2.1.4 Effect of Order on Dislocation Mobility

Ordering exerts a large influence on the mechanical properties of intermetallic compounds due to the resulting superlattice dislocations. The unique characteristics of superlattice dislocations generally result in a reduction in the number of slip systems and a restriction of slip .

Superlattice dislocations of the type found in B2 ordered Fe_3Al have great difficulty in undergoing cross-slip. As the leading dislocation in a two-fold superlattice dislocation encounters the intersection of two slip planes, it may slip to the second plane. Once on the second plane, the dislocation may become sessile if the trailing dislocation does not cross slip onto the same plane. If the first dislocation becomes sessile, then a pile-up of dislocations can occur and cause a stress concentration which is a site for premature failure. In ordered alloys, APB energy influences the cross-slipping ability of superlattice dislocations. Cross-slip can occur more readily if the APD is small as the partial dislocations will be close together. In ordered alloys the APB energy is affected by both stoichiometry and composition. For example, in Fe_3Al alloys the NNAPB energy increases from 42 to 79 erg/cm^2 as the aluminum content changes from 25.5% to 28.3% (12, 13).

Slip may be inhibited by the relatively low diffusion rates in many ordered alloys. It has been shown that in intermetallic compounds, such as Ni_3Pt and Ni_3Fe (14), the diffusion rate dropped as the alloy transformed to the ordered state. A superlattice dislocation which has become sessile on one plane can become mobile if it undergoes diffusion-assisted climb to the plane containing the trailing dislocation. Due

to the lowered diffusion rate in the ordered alloys, however, the likelihood of climb is reduced, thus the dislocation remains sessile.

The unique characteristics of superlattice dislocations are also responsible for the high strain hardening rates found in many ordered intermetallics. Strain hardening results from the interactions of dislocations with each other and with barriers which impede their motion through the crystal by requiring increased stress to cause slip. Fe_3Al alloys of high aluminum content have been found to possess high strain hardening rates (15). The result of high strain hardening rates in ordered intermetallics is that they exhibit significant ductility while the fracture appearance is typical of brittle failure, such as transgranular cleavage or intergranular fracture. As the material undergoes plastic straining, the applied stress increases to the point that grain boundary or cleavage fracture occurs before ductile fracture takes place.

2.2. Fe_3Al Alloys

The presently accepted Fe-Al phase diagram is shown in Fig. 2.4. The Fe_3Al intermetallic phase exists in the aluminum range from 24% to 32%. The ordered range of the phase diagram is shown in Fig. 2.5. In the range of 24% - 32% aluminum Fe_3Al can exist in two ordered states, as well as a disordered state. The ordered B2 state is stable from 560°C to 800°C and above 800°C a disordered α phase forms. Below 560°C, the DO_3 ordered state is stable. A predominantly B2 ordered state can be retained at room temperature by quenching from above 560°C.

2.2.1 Properties of Fe_3Al Alloys

Fe_3Al alloys do not possess high room temperature ductility in air. While the ductility varies with aluminum content and state of order it generally ranges between 2

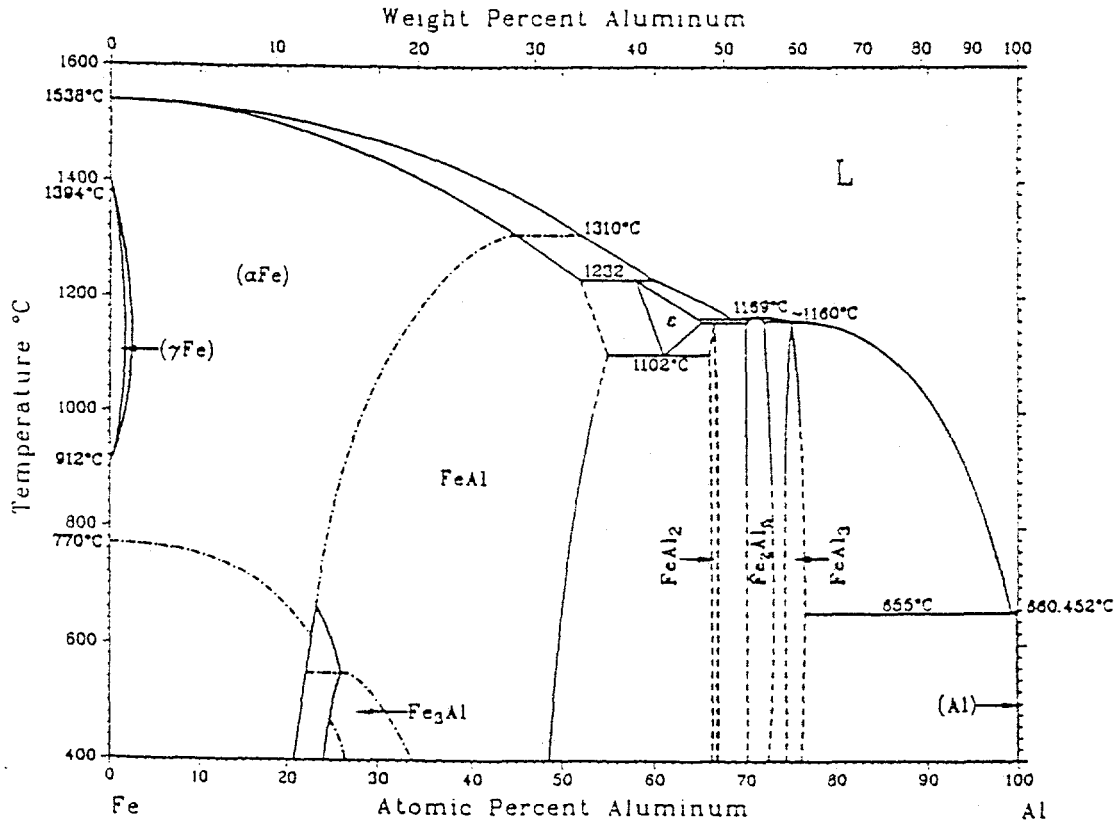

Fig. 2.4 Fe-Al phase diagram (16).

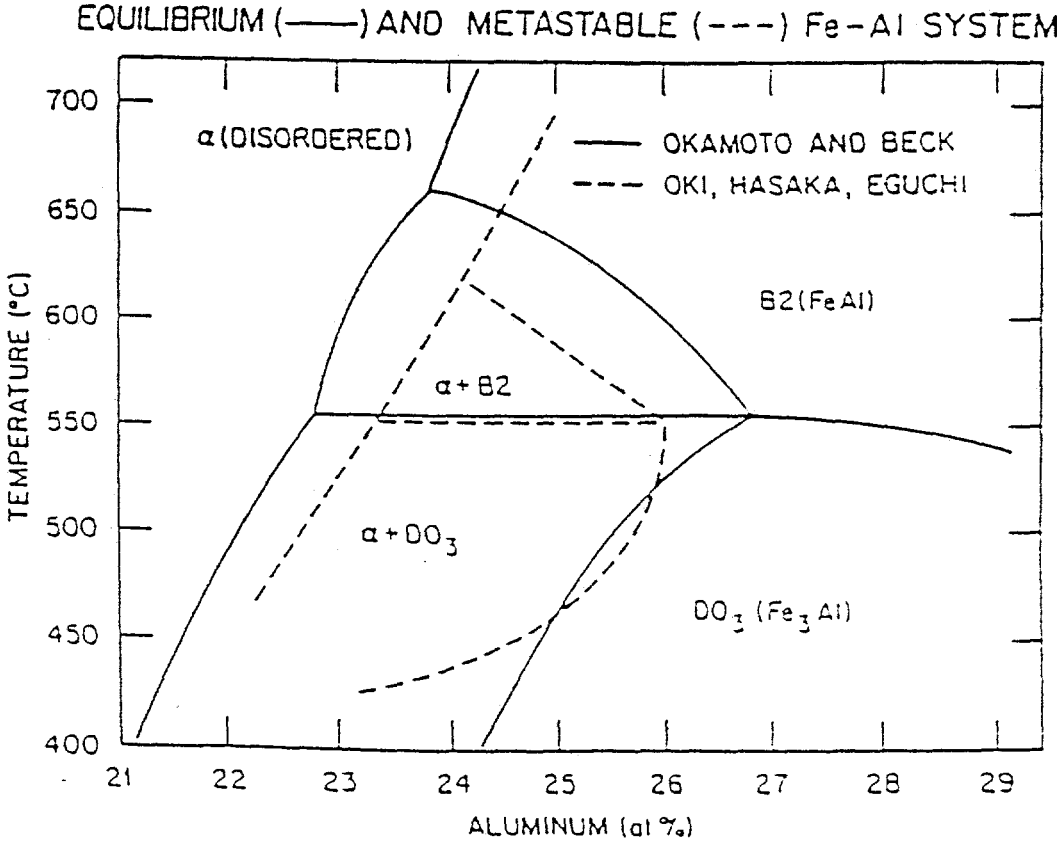

Fig. 2.5 Ordered Fe_3Al region of the Fe-Al phase diagram (17).

and 8%, with the B2 ordered state having higher ductility than the DO_3 (5). Due to the low ductility of Fe_3Al alloys it was thought that they were intrinsically brittle. Only in the last ten years was it found that iron aluminides were susceptible to environmental embrittlement.

Fe_3Al alloys have been shown to possess ductility greater than 10% when tested in vacuum or gaseous oxygen environments (5, 18, 19). Additionally, it was found that Fe_3Al alloys undergo (110)<111> type slip which provides at least 5 slip systems, exhibit moderate yield and tensile strength, and fracture in a transgranular manner (6). All of these behaviors are associated with inherently ductile materials.

The ductility of iron aluminides is very susceptible to changes in the aluminum content. Ductility in alloys with less than 20% Al is between 15% and 20% in inert environments. In the 20-27% Al range, the ductility drops to 6% or less (5, 20). In the range of 28-35% aluminum, ductility again rises to 14%. Above 35% Al, the ductility again drops to levels below 10%. Studies have shown that the most promising alloys are those with an aluminum content of 28-30% (18). This sensitivity is due to a combination of changes in ordered structure, slip mechanisms, and grain boundary chemistry.

2.2.2 Improving the Properties of Fe_3Al

Initially, improved ductility of Fe_3Al in air was accomplished through control of the composition and microstructure. An increase in the ductility of iron aluminides can be achieved by increasing the purity of the alloy. Kerr (3) showed that decreasing the carbon content increased ductility. The ductility of an Fe-25.5Al alloy, which contained 500ppm carbon had a ductility of 2.1% which increased to 4.1% after decarborization, to 50 ppm. It was found that the carbon formed a second phase, Fe_3AlC, which precipitated predominately along grain boundaries. It has also been shown that Fe_3Al

fails in an intergranular or mixed-mode manner if the alloy possesses high levels of impurities (21).

The type and degree of order has also been shown to have an effect on the ductility. Liu et al (5) found that the B2 structure had higher ductility than the DO_3 structure when tested in air. The minimization of DO_3 ordered phase was also found to reduce environmental sensitivity in tensile and fatigue tests (22, 23, 24).

Thermomechanical treatment presents a means for improving the properties of iron aluminides. McKamey and Pierce (25) showed that iron aluminides which possess a partially unrecrystallized structure, as well as a pronounced directionality to the grain orientation, have high ductility. In their study, recrystallization was controlled by varying the annealing temperature. The peak in ductility occurred at an annealing temperature of 750°C and resulted in a 10% recrystallized structure. Ductility was less for both the as-rolled and the completely recrystallized structures. Viswanathan et al (26) conducted a similar study finding that the room temperature ductility can be maximized by the presence of elongated, unrecrystallized grains.

Alloying iron aluminides with boron has been attempted to increase ductility. The practice of micro-alloying nickel aluminides with boron is well-known to dramatically increase ductility. Ni-24Al, when alloyed with 0.1 wt% B, underwent an increase in ductility from 1% to 54% (27). In the case of nickel aluminides, the fracture mode changes from one of intergranular to transgranular with boron additions. This effect has been shown to be due to the segregation of boron to grain boundaries, thereby strengthening the grain boundaries.

Similar attempts have been made to increase the ductility of iron aluminides with boron. A slight ductilizing effect of boron was found in Fe-40Al (28, 29). In both studies, the ductility was increase a few percent but still remained below 5%. Horton et al (30) attempted to ductilize Fe-25Al with 0.24%B. They found no increase in the

ductility in air nor in the fracture surface appearance. The fact that boron did not increase ductility in the Fe-25Al while it did in the Fe-40Al indicates that the ductilizing mechanism of boron is related to the availability of aluminum at the grain boundaries. As the aluminum concentration falls below 37%, the weak points change from grain boundaries to cleavage planes, thus the boron has no observable effect.

Attempts have also been made to increase the ductility of Fe_3Al by alloying with elements other than B. Gaydosh et al (31) noted an increase in room temperature tensile strength with additions of 0.1 at.% Hf or Zr to an Fe-40Al alloy. While the room temperature ductility was found to decrease with both Hf and Zr additions, the ductility at high temperatures increased significantly when compared to the binary alloy. In another study, an increase in tensile and creep strength accompanied by a drop in room temperature ductility was shown to result from the additions of Mo, Nb, Zr, and C to an Fe-28Al-5Cr alloy (32).

While room temperature ductility is decreased with alloying additions of elements such as Si, Ta, Ce, Ti, Zr, Hf, or Nb, the high temperature tensile and creep strengths have been shown to be improved (8, 9, 33, 34, 35, 36, 37). For example, additions of Mo or Nb in combination with small amounts of Zr improve the creep-rupture strength of Fe-28Al from 2-5 h up to 100-300 h life at 593°C and 207 MPa (38). The effect of these elements is due to their low solubility in iron aluminides, thus they will form as either intermetallic precipitates or carbides. These precipitates are potent strengtheners if they can be formed as fine matrix particles through heat treatments.

Surface condition has been shown to play an important role in the ductility and resistance to embrittlement. McKamey and Liu (20) found that the surface condition of an Fe-28Al-4Cr alloy was a major factor in tensile ductility. They investigated the role of a fine protective oxide layer produced by polishing the surface and annealing in air, and a coarse oxide scale produced by the thermomechanical processing. The ductility

increased in the presence of the fine layer compared to the coarse scale. The Cr addition was crucial to the results as no difference in ductility was found between oxide layers in the binary Fe-28Al alloy.

A similar result can be produced by simply coating the surface of the iron aluminide test specimen with oil, or some other protective coating. Liu et al (4) found that the ductility increased in air from 2.2% to 5.6% when a layer of silicone oil was applied to the specimen of Fe-36.5Al. While the oil coating improved the ductility, it was not completely impervious to the embrittling environment as the ductility in an oxygen environment was 11.3%.

2.2.3 Effect of Chromium Additions

Chromium, when alloyed with Fe_3Al in small amounts, has been shown to improve room temperature ductility. McKamey et al (6) found that additions of 2% chromium increased the ductility of DO_3 ordered Fe_3Al in air from 3.7% to 9.4%. The ductility decreased slightly with 4% and 6% Cr to 8.2% and 8.4%, respectively. The increase in ductility was also accompanied by a change in fracture mode from completely transgranular cleavage to mixed transgranular cleavage and intergranular fracture.

Cr additions also had effects on the yield and tensile strength. The yield strength decreased from 279 MPa to 247 MPa with a 2% Cr addition. This decrease in yield strength was attributed to a solid solution softening effect. The tensile strength increased with the same 2% Cr addition from 514 MPa to 638 MPa. This increase was attributed to the increase in cleavage stress accompanied by the Cr addition.

The beneficial effect of Cr on iron aluminides has not been fully explained, but studies so far point to several possible mechanisms. Increased cleavage strength which partially suppresses cleavage fracture, was initially suggested by McKamey et al (39). A

more detailed study led to the possibility of reduced APB energy (6). The reduction of APB increases the separation between the four superdislocations, thereby allowing easier dissociation and cross slip. Morris et al (40) also investigated the influence of Cr on the properties of Fe_3Al and found no reduction in the APB energy. Another possibility suggested was the stabilization of the B2 structure with an accompanying reduction in the DO_3 structure (41). More recently, Balasubramaniam (42, 43) proposed that it is an electrochemical passivation mechanism that is responsible for the beneficial effect of Cr on the embrittlement of iron aluminides.

2.2.4 Environmental Embrittlement in Fe_3Al

Workers at Oak Ridge National Laboratory (5) were the first to find that Fe_3Al was intrinsically ductile. The predominant embrittling mechanism in iron aluminides is believed to be similar to that of aluminum and its alloys. In these alloys, the chemical reaction that leads to embrittlement in moist air is as follows:

$$2Al + 3H_2O \rightarrow Al_2O_3 + 6H^+ + 6e^- \qquad \text{Eq. 2}$$

$$6H^+ + 6e^- \rightarrow 6H$$

This reaction causes the release of atomic hydrogen at the crack tip, which then migrates into the metal. This mechanism is possible in iron aluminides due to the large amount of aluminum present. However, it is not the only embrittling mechanism as it has also been shown that embrittlement in gaseous hydrogen can also occur (19).

Zhu et al (44) completed an Auger analysis on surface reactions of Fe_3Al with water vapor and oxygen. They found that the aluminum in Fe_3Al reacted with water vapor, leading to the formation of Al_2O_3 on fresh surfaces. In an oxygen atmosphere, the formation of Al_2O_3 was also found to occur. They also found that the initial

oxidation of Al by water vapor occurs at approximately the same exposure level as by oxygen. The fact that Al_2O_3 was found to form in a water vapor environment supports the embrittlement mechanism mentioned above.

In Fe_3Al alloys, embrittlement under monotonic tension is generally most severe in a moist air environment. It has also been shown that testing in pure oxygen environment effectively stops embrittlement and can result in ductility greater than that in vacuum (5, 45, 46). Liu et al (4) found that the lowest ductility for a B2 ordered Fe-36.5%Al alloy tested in various environments was in water vapor (2.4%) and laboratory air (2.2%). Somewhat higher ductilities were measured in an argon-hydrogen mixture (5.5%) and vacuum (5.4%), while the highest ductility was measured in oxygen (11.3%). Similar results were found in a lower aluminum alloy, FA-129. Castagna (46) found that for B2 ordered FA-129 tested in tension in laboratory air, vacuum and oxygen gas atmospheres, the lowest ductility was in air (8.8%). The ductility in vacuum was higher (13.7%), while the highest was measured in oxygen (16.2%).

An exact threshold concentration of water vapor or hydrogen gas for embrittlement of Fe_3Al alloys has not been determined, but studies have shown that the amount of moisture necessary to induce embrittlement is very small. McKamey and Lee (47) found that a partial pressure of 133 Pa caused the ductility of a Fe_3Al alloy to drop from 24.2% to 9.0%. The ductility in 30% relative humidity (rH) laboratory air was found to be similar to that of the 133 Pa of water vapor. While the threshold level of moisture needed for embrittlement appears to be very low, the concentration dependence on embrittling water vapor is weak above this level.

The kinetics of embrittlement in air in an Fe-35Al alloy were investigated by Kasul and Heldt (48). They found that baking treatments fully restored ductility in hydrogen precharged specimens. The kinetics of the recovery were shown to be consistent with the room temperature diffusion coefficient. Most importantly, they

showed that this rate is not capable of transporting hydrogen ahead of the crack moving at stage II velocity, which points to a dislocation-assisted mechanism for the embrittlement of iron aluminides.

While the environment has been shown to have a considerable effect on the ductility and fracture toughness of Fe_3Al alloys, it has been shown to have little or no effect on other mechanical properties such as yield stress and strain hardening rate. These parameters are effected more by changes in stoichiometry and alloy composition.

An important indicator of the mechanism of embrittlement is the appearance of the fracture surface. Fracture topography in Fe_3Al has been observed to be very dependent on aluminum concentration, while only slightly dependent on environment. This relationship between aluminum concentration and fracture appearance in iron aluminides has been reported in many studies.

Binary Fe_3Al alloys with aluminum contents less than 30% tested in tension exhibit a transgranular (TG) fracture mode (5, 49, 50, 51, 52). For binary alloys with aluminum concentrations of 30-37%, the fracture mode is mixed transgranular and intergranular (IG) (47, 49). For binary alloys with more than 37% aluminum, the fracture mode is IG. The shift to IG failure with increased aluminum content is believed to be the result of weakened grain boundaries as their composition changes (49, 53).

Changes in fracture mode as the environment changes have only been observed in binary alloys with aluminum contents between 35% and 36%. Binary Fe-35.5Al was found to shift from TG in air to mixed TG and IG in vacuum, and, finally, to completely IG in oxygen (4). In binary Fe-36.5Al, the fracture mode followed the same pattern. Alloys with aluminum contents above 37% failed intergranularly in air and oxygen. The comparison of the fracture modes indicates that the grain boundaries in Fe_3Al are strong enough to resist crack nucleation and propagation. The occurrence of cleavage fracture in air suggests that the cleavage planes are more susceptible to embrittlement than the

grain boundaries. When testing is carried out in a moisture-free environment, fracture occurs along the grain boundaries, which are intrinsically the weakest link in aluminides. This shift of failure mode indicates that hydrogen acts on the cleavage planes in iron-aluminum alloys.

2.3 Environmental Embrittlement

Embrittlement is the loss of ductility or fracture toughness in a material due to a reaction with an element of the external environment, or a reaction with an internal contaminant that is not an intentional constituent of the material. Embrittlement can be denoted by a loss of tensile ductility, shortened fatigue life during high or low cycle fatigue, increased crack growth rates during fatigue crack growth tests, or reduced K_c in fracture toughness tests. Figs. 2.6 and 2.7 illustrate the effect of embrittlement on the mechanical properties of Ni_3Fe (54) and FeCo-V (55), respectively. Fig. 2.6 shows the loss of ductility and decreased tensile strength of ordered and disordered Ni_3Fe when hydrogen is cathodically charged into the test specimen (54); while Fig. 2.7 illustrates the effect of hydrogen gas on the fatigue crack growth resistance of an ordered and disordered FeCo-V alloy (55). There are several types of embrittlement which fall under the heading of environmental embrittlement. They are: oxidation, sulfidation, liquid-metal embrittlement, and hydrogen embrittlement. In the context of iron aluminide alloys the most important of the external contaminants is hydrogen.

Embrittlement generally results in a material that is much harder to work with than a more ductile material. In order for the embrittlement phenomenon to be observed, a material must possess some degree of intrinsic ductility. A material that does not possess a sufficient number of slip planes or has weak grain boundaries or weak cleavage planes, and is therefore inherently brittle, may not show evidence of

embrittlement even if the requisite mechanical and chemical conditions exist for embrittlement.

Hydrogen embrittlement has been observed in many materials. It was first recognized in structural steels, and numerous studies have shown many such steels to be susceptible. It is widely recognized that many intermetallic compounds also are susceptible to hydrogen embrittlement.

The intermetallics which are most susceptible to hydrogen embrittlement are those with highly symmetric crystal structures such as the $L1_2$, B2, and DO_{19}. $L1_2$ alloys which are embrittled include Co_3Ti (45, 56, 57), nickel aluminides (58, 59, 60, 61), $(FeNi)_3V$ (55, 62), and Ni_3Fe (54). The embrittled B2 alloys include FeCo-2V (55), and Fe_3Al (20, 49, 63). DO_3 ordered Fe_3Al also has been found to be embrittled by hydrogen (4, 5, 19, 63).

2.3.1 Hydrogen Embrittlement

The process by which hydrogen embrittles a material can be broken down into a sequence of stages which include:

- transport of the hydrogen to an exposed surface
- surface reactions and/or adsorption
- transport of the hydrogen to the embrittled zone
- hydrogen-metal interaction
- fracture at load, stress intensity or deformation levels which are lower than in inert environments

Each stage is time dependent and this rate may depend on various parameters such as temperature, concentration, alloy composition, and degree of deformation. The

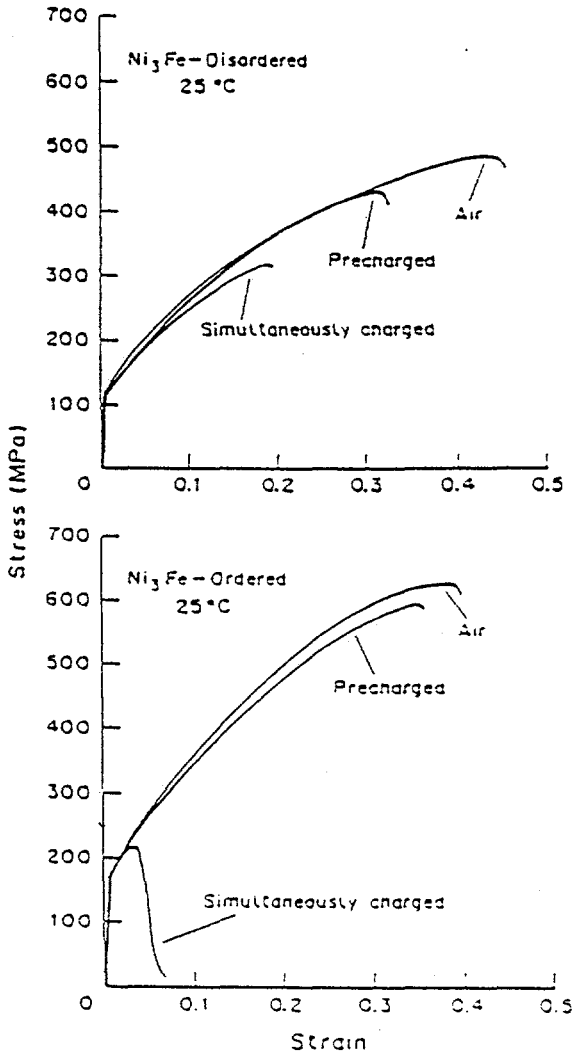

Fig. 2.6 Effect of environment on the tensile properties of Ni_3Fe (54).

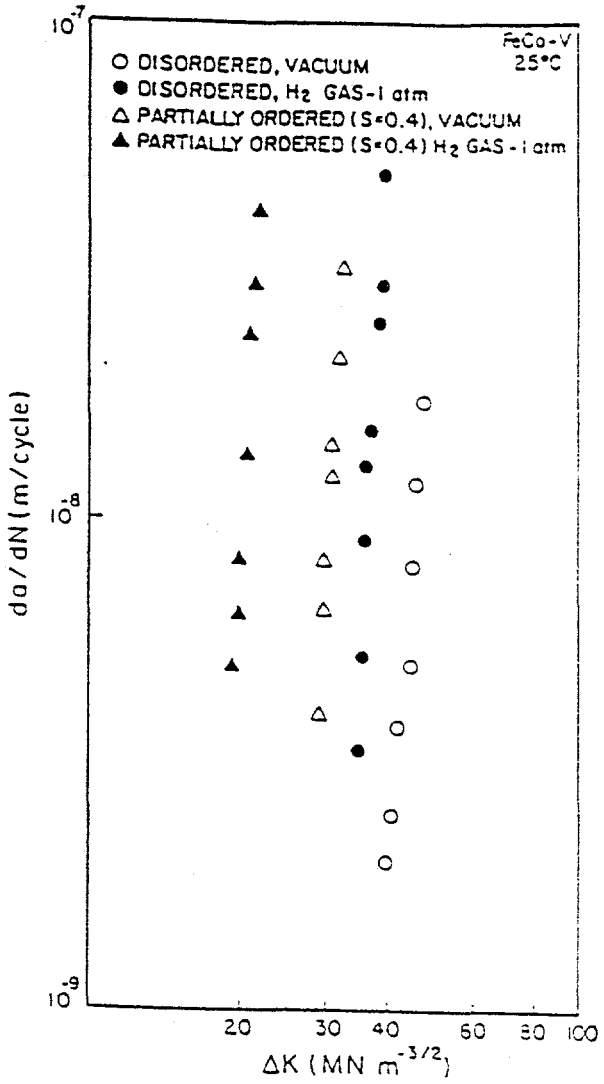

Fig. 2.7 Effect of environment on the FCG resistance of FeCo-V (55).

alloy in question, the test environment, and the loading situation will determine the rate at which each stage progresses, and each stage can often be dependent on the previous one. In some cases, one or more of the stages can be identified as the rate-limiting step in the embrittling process. The rate-limiting step dictates the rate and degree of embrittlement because it constrains all subsequent stages in the embrittlement process.

2.3.1.1 Transport to the Surface

The transport of the embrittling species to the surface of the material can occur in one of two ways; by diffusion or by mixing. The method will depend on the embrittling species and on the media through which it must be transported. In terms of hydrogen embrittlement, the diffusion of H^+ ions in H_2O occurs approximately 10 to 1000 times faster than diffusion of hydrogen atoms or molecules in a gaseous media. One reason for the slower rate in gaseous environments is that transport depends on the temperature, the partial pressure of the embrittling species, and whether there are any other gaseous species present. The presence of other species may reduce the transport rate of the embrittling species as they can compete for the same surface sites. Successful transport is the complete impingement of the embrittling species on the exposed surface such that it covers the entire surface, or a critical fraction thereof.

The difference between the chemistry on the surface and that far from the surface is responsible for the manifestation of the rate limiting phenomenon in the transport stage. This chemistry difference is especially evident within the crack tip region of a cracked material. The crack length and geometry of the specimen are also important factors in a rate limited transport stage as they will influence the distance the embrittling species must be transported, as well as the distance the chemical by-products must be transported away. Embrittlement involving a transport rate limited stage will also be expected to vary with frequency of cyclic loading.

Gudladt and Petit (64) conducted a study on the rate limiting transport stage in an aluminum alloy. In it they calculated the time to cover the exposed surface of an Al-Zn-Mg alloy with H_2O vapor in vacuum and nitrogen gas. They found that the rate at which the surface coverage occurred was decreased by a factor of 10 to 100 in a nitrogen gas environment due to the competition for active sites between H_2O and N_2. The Al alloy was also fatigued in H_2O vapor, moist N_2, and vacuum atmospheres. In the moist environments, the threshold stress intensity was low, and at low stress intensities, the Paris slope was high compared to those measured in vacuum. At higher stress intensities, the da/dN vs. ΔK curve in moist N_2 converged with that of the vacuum.

The reason for the convergence is found in the rate limiting transport stage. At low crack growth rates, the transport of H_2O vapor through the nitrogen was rapid enough to cause embrittlement. As the crack growth rate increased, the time per cycle was not enough to allow the complete transport to take place and thus transport became rate limiting.

2.3.1.2 Surface Reactions

Once the embrittling species has reached the surface of the material, it must be adsorbed or absorbed into the material. It may also have to undergo diffusion to reach the embrittled zone, and/or undergo various chemical reactions. In terms of hydrogen embrittlement, the various reactions that can take place at the surface are dependent on the form of hydrogen, i.e., as H^+ ions or as molecules.

When a chemical transformation of the embrittling species is necessary, the surface reaction stage can be rate limiting. In gaseous hydrogen, hydrogen present in the molecular H_2 form must dissociate to atomic H before adsorption can take place. In aqueous environments, such as moist air, the hydrogen must be evolved through chemical reactions with a sufficiently reactive element on the material's surface before

adsorption can take place. These elements include Al, V, Si, and Ti. Once monatomic hydrogen is formed, it is of high fugacity and can penetrate rapidly into the bulk of the material. Iron aluminides are very susceptible to this type of embrittlement (49, 51, 53) due to the significant amount of aluminum in the alloys.

An example of surface reactions being rate limiting is at elevated temperatures. At high temperatures, the dissociation of molecular H_2 to atomic H is less likely and thereby limits the amount of hydrogen available for transport into the bulk (65). Elevated temperatures are not necessary for surface reactions to be rate limiting. During the fatigue of steel in hydrogen gas, the adsorption of hydrogen at the surface has been shown to be rate limiting (66).

2..3.1.3 Bulk Transport

Bulk transport is the step responsible for conveying the embrittling species to the affected zone in the material. There are a number of mechanisms by which the embrittling species can be transported through the bulk, such as dislocation-assisted transport and diffusion.

An important requirement in hydrogen embrittlement is that the transport of hydrogen take place while the material is undergoing plastic work. Many studies have shown that steels and intermetallics are not embrittled by exposure to hydrogen prior to testing in air, or even exposure during elastic straining prior to testing in air (54, 67), while they are embrittled when hydrogen and plastic deformation are applied simultaneously.

Dislocation-assisted transport is one widely accepted theory for the transport of hydrogen through the bulk (68). In this theory, the motion of the dislocations caused by plastic deformation enhances hydrogen transport. An atmosphere of hydrogen forms about a dislocation that intersects the surface where the local hydrogen concentration is

high. During further plastic deformation, the dislocation moves away from the surface dragging the hydrogen atmosphere with it. Through this mechanism, hydrogen atoms may "ride" the dislocation further into the bulk and faster than by diffusion. The hydrogen atmospheres can then be "stripped off" or deposited at microstructural locations such as grain boundaries, inclusions, and precipitates. These locations may be critical paths for hydrogen induced fracture.

Support for this mechanism has been seen in several investigations where large increases in H_2 concentrations within steel specimens tested in tension have been found. The hydrogen was found at a depth of up to 10 times greater than diffusion could carry the atoms (69). Further proof of this mechanism was found when the same material was elastically strained in hydrogen, where slip is not operable, no H_2 concentration increase was found.

The role of diffusion is also consequential in the transport of hydrogen. Ricker and Duquette (70) found the fatigue life of an Al-Zn-Mg alloy to be considerably shortened by either fatiguing in a moist nitrogen atmosphere or pre-exposing the material to moist air for at least 30 days prior to fatiguing in a dry nitrogen atmosphere. While diffusion is not responsible for the shortened life in the moist nitrogen atmosphere, it is an active mechanism for the bulk transport of hydrogen when sufficient time is available. The damage incurred during pre-exposure was reversible, as the restoration of fatigue life was accomplished by exposing the specimen to vacuum, thereby forcing the hydrogen to diffuse out.

The dependence on the diffusion rate of hydrogen for embrittlement has been observed in several intermetallic systems that can exist in more than one ordered state. In these alloys, the bulk diffusivity of hydrogen increases as the degree of order decreases. Embrittlement is seen in ordered $(FeNi)_3V$ (55, 62, 70) and Co_3Ti (45) while little embrittlement is observed in the disordered state of these alloys. While the

observation that embrittlement increases in the ordered state seems inconsistent with decreased diffusivity, an explanation may lie in the fact that the ordered lattice is prone to regions of high hydrogen concentration, such as slip planes. In the ordered state, the hydrogen is less likely to diffuse away from these regions, as a result of decreased dislocation motion and reduced ease of cross-slip, while in the disordered state the hydrogen is able to rapidly diffuse away, or due to increased dislocation mobility is less likely to build up at highly stressed.

2.3.1.4 Hydrogen -Metal Interactions

Once the embrittling species is transported to the appropriate area, it reacts with the material such that the intrinsic strength is reduced. Several theories describing the hydrogen-metal interaction have been proposed.

One possible explanation of hydrogen-metal interactions is the pressure theory. In this theory, the driving force for crack propagation is the high pressure of internal bubbles that result from hydrogen atoms that recombine to form H_2 molecules at internal voids (71, 72). Pressures are suggested to reach thousands of MPa. While this theory is consistent with both the temperature and strain dependencies found in many studies, it cannot be the sole mechanism. One problem is that the internal pressure in the bubble would decrease rapidly in the absence of a continuous source of high fugacity hydrogen. The observation of severe hydrogen embrittlement by low pressure hydrogen gas, where high pressure bubbles cannot form (73) , supports this point.

Another theory is that hydrogen reduces the surface energy of the material, which thereby reduces the energy necessary for crack propagation (74). In this theory, dislocations could carry the hydrogen to the vicinity of a microcrack and there interact with the material to lower the surface energy. Inconsistencies of this mechanism with experimental observations have raised many objections to this theory. For example, in

gaseous H_2, crack propagation velocities measured at constant stress intensity showed an increase with test temperature (75), rather than a decrease as would be expected from a reduced surface energy theory.

A theory that provides for a more substantial contribution to embrittlement is the "decohesion" mechanism first introduced by Troiano (76), and expanded by Oriani and Josephic (73, 77). This mechanism postulates that brittle fracture occurs when the local stress exceeds the atomic bond strength and that the presence of hydrogen as a solute decreases the atomic bond strength. The basic problem associated with this theory is that evidence to support it, as well as counter evidence, has not been forthcoming. One aspect of the decohesion mechanism that has been supported by experimental evidence is the increase in hydrogen solubility in high stress regions, such as a crack tip.

Another hydrogen-metal interaction that has been well documented in titanium alloys, vanadium, niobium, and hafnium is stress induced formation of hydrides. One such intermetallic that forms hydrides is Ti_3Al (78). In this mechanism, the chemical potential of solute hydrogen at stress concentrations, such as crack tips, decreases, thereby allowing hydrogen to diffuse into these areas. Due to this excess hydrogen, precipitation of metal hydrides occurs. These hydrides are very brittle and, due to their large change in volume of formation, are incoherent in the metal lattice. This incoherency significantly reduces the effective fracture toughness in the region of the crack, thus allowing rapid crack growth in a transgranular cleavage mode. The kinetics of hydride formation in some alloys is slow enough that continuous formation ahead of an advancing crack is not possible. Therefore, when the crack extends beyond the region of hydride formation it slows.

It should be noted that in a material that is embrittled by hydrogen, more than one hydrogen-metal mechanism can be active. Fractographic observations often give an indication of the mechanism that is active, as well as the affected region (i.e., throughout

the bulk, along crystallographic planes. or along grain boundaries). But, it is not always possible to completely rule out any other type of hydrogen-metal interaction based solely on these observations.

For example, the grain boundary embrittlement of some polycrystalline materials does not imply that the same material in single crystal form is resistant to embrittlement. While these materials may be prone to embrittlement on particular cleavage planes, or localized plasticity throughout the bulk, this type of embrittlement may be hidden by a more severe embrittlement of the grain boundaries in the polycrystalline form. One such alloy that exhibits this type of behavior is Co_3Ti-Ni (45, 56, 57). In inert environments, Co_3Ti-Ni fails in a dimpled transgranular mode, but when tested in an aggressive hydrogen atmosphere, the failure mode shifts to intergranular. Liu et al (45) have shown that the single crystal form of Co-23Ti-3Ni was subject to severe embrittlement. The failure occurred on {100} cleavage facets in hydrogen gas while a dimpled surface was observed in vacuum.

2.3.2 Characteristics of Hydrogen Embrittlement

For hydrogen embrittlement mechanisms to be active, the loading conditions and the detrimental species must be applied simultaneously (79). However, hydrogen embrittlement can occur without the embrittling species present in the environment if the material has been previously exposed to such an environment and the hydrogen is retained by the material. Such is the case with cathodic pre-charging.

The dependence of embrittlement on concentration in a gaseous environment is often weak once a sufficient amount of the embrittling species is present. As the concentration is increased above this threshold level for embrittlement, no further increase in the degree of embrittlement is seen. This threshold concentration is often dependent on the deformation rate (i.e., in cyclic loading it is the frequency, while in

monotonic tension it is the strain rate). In fatigue crack growth experiments, the crack growth rate per cycle, da/dN, greatly affects the threshold concentration and concentration dependence. A material with a propagating crack may exhibit environmentally enhanced crack growth at low growth rates while the crack growth is unaffected by environment at high growth rates because the concentration threshold necessary for embrittlement was increased beyond the existing concentration.

In monotonic tensile testing, the degree of hydrogen embrittlement often increases as the strain rate decreases. This is due to the fact that one of the transport phenomena, such as surface chemical reactions or diffusion of the species to the surface, may be rate limiting. As the strain rate is decreased, the amount of time provided for the rate limiting step to be completed increases. Thus the trend for increasing ductility with increasing strain rate is evidence of a material which is environmentally embrittled.

The strain rate effect on the degree of embrittlement has been documented in numerous studies. For example, in a study on Co-23Ti. it was found that there was no change in ductility when the strain rate was decreased from $5.6x10^{-2}$/sec to $5.6x10^{-4}$/sec while testing in vacuum (57). For the same strain rate decrease for tests performed in air, the ductility decreased by 85%. In a Ni_3Al alloy an increase in ductility from 4 to 10% was found for a 1000-fold increase in strain rate (80). Fe_3Al and Fe_3Al,Cr alloys have also been shown to display similar results. Scott (81) found that in DO_3 ordered Fe_3Al an increase in strain rate from $3x10^{-8}$/sec to $1x10^{-2}$/sec increased the ductility from 1 to 8%. In Fe_3Al,Cr, the ductility increased from <2% at a strain rate of $5.5x10^{-5}$/sec to 8.8% at a strain rate of $3.3x10^{-2}$/sec (82).

Some mechanical properties of the material can affect embrittlement, such as yield and ultimate tensile strength (UTS). Yield stress has an effect on the size of the plastic zone and the magnitude of the triaxial stress ahead of the crack or notch. High

UTS materials may have faster dislocation velocities during plastic deformation which could increase embrittlement if a dislocation assisted transport mechanism is active.

Hydrogen embrittlement also exhibits a strong dependence on temperature for most embrittled alloy systems. In most cases, the maximum embrittlement occurs at room temperature with little or no embrittlement at 50 to 100°C above and below room temperature. For example, Cotterill and King (65) investigated the dependence of fatigue crack growth rates in AISI 4360 steel on temperature and environment. In air, the Paris slope was between 4.0 and 4.2 for test conducted from 25°C to 80°C. When testing was performed in hydrogen, the resulting Paris slope was 8.7 at 25°C, but as the temperature was increased, a steady decrease in the slope was exhibited due to the diminished embrittling effect. A similar trend was seen in hydrogen pre-charged martensitic steel (67). Severe embrittlement was observed near room temperature and a steady drop in embrittlement occurred as the temperature was increased to 200°C. At this point the behavior of the hydrogen charged steel was similar to that of hydrogen-free steel. This peak in embrittlement at room temperature is unfortunate as most engineering structures operate in this range.

A likely explanation of this effect is that as the diffusivity of hydrogen increases with the increase in temperature. It has been shown that hydrogen embrittlement requires the development of a critical hydrogen concentration at stress concentrations and that uniform distribution of solute hydrogen below this critical concentration sill not cause embrittlement (83). With the increased diffusivity the solute hydrogen is more likely to be uniformly distributed rather than concentrated at stress concentrations In hydride forming materials at elevated temperatures, the formation of hydrides is slowed, therefore ductile failure can occur (78).

2.4 Fatigue Crack Growth

2.4.1 Crack Growth

The fatigue process can be divided into three phases: crack initiation, crack growth, and, ultimately, catastrophic failure. Crack nucleation in fatigue is dependent on plastic deformation and dislocation interaction. The resistance to crack nucleation under cyclic loading can be increased if the material undergoes limited cross slip and has few operable slip systems. This is the case in many ordered intermetallic systems.

As previously mentioned in section 2.1.3, ordered alloys possess superlattice dislocations. Superlattice dislocations are often observed to undergo planar slip which enhances resistance to crack nucleation by slip reversibility (84). Slip reversibility occurs when slip steps, which normally form at the surface of a fatigued material and act as nucleation sites, are annihilated or do not form to the same extent. This happens because slip which occurs during the tensile portion of the loading cycle is reversed during the unloading or compressive portion. Reversibility is likely when slip is restricted to a few crystal planes or slip is planar. In ordered alloys, planar slip has been attributed to a lowered APB energy on planes in which slip does not normally take place. For example, in Cu_3Au crystals, the APB energy on {100} planes was found to be much lower than on {111} planes where slip normally takes place (85). Superdislocations tend to cross slip but become sessile on the {111} plane.

There are numerous factors that affect crack propagation in metals and alloys. These factors include, but are not limited to, grain size, dislocation structures, inclusions/precipitates, sample thickness, mean stress, frequency, temperature, and environment. The major microstructural variable that changes in an alloy which undergoes ordering is the dislocation structure. The nature of superlattice dislocations associated with an ordered lattice has significant effects on the ability to cross slip.

In a number of studies, a shift to an ordered structure has resulted in increased resistance to fatigue. Boettner et al (86) found that ordering increased the fatigue limit of FeCo-V and Ni_3Mn by approximately 20%. The increase was ascribed to a decrease in fatigue-induced surface roughness and crack nucleation sites as a result of inhibited cross slip.

It has also been shown that there is a correlation between stacking fault energy (SFE) and resistance to fatigue cracking in disordered Cu and Al alloys (84). Resistance to crack nucleation and propagation was found to increase with decreasing SFE, due to its effect on cross slip. Lower SFE, which makes cross slip less likely, also increases the resistance to subgrain formation. These subgrains can act as paths of enhanced crack growth.

2.4.2 Environmentally Assisted Crack Growth

It has been proposed that fatigue crack growth in an embrittling environment can be considered to be the superposition of crack growth in the alloy due to mechanical fatigue, crack growth due to stress corrosion cracking, and crack growth due to corrosion fatigue. This superposition can be expressed as:

$$da/dN = (da/dN)_{mech} + (da/dN)_{scc} + (da/dN)_{cf} \qquad \text{Eq. 3.}$$

Fig. 2.8 illustrates the superposition model as described by McEvily and Wei (87), where purely mechanical crack growth and purely stress corrosion crack growth are shown in Figs. 2.8a and 2.8b, respectively. It is important to note that stress corrosion cracking is not cycle dependent. Stress corrosion cracking occurs as a function of time and results from sustained load cracking at stress intensity levels above the stress corrosion crack threshold, K_{Iscc}.

Environmentally enhanced fatigue crack growth can usually be characterized in terms of one of three generic patterns of behavior illustrated in Fig 2.9. The first case (Fig. 2.9a) represents the system where both the mechanical and corrosion terms in Eq. 3 are active. In this case, there is accelerated crack growth for all stress intensity values. Fig. 2.9b illustrates the case when both the mechanical and stress corrosion cracking terms in Eq. 3. are active. The da/dN_{scc} term will not contribute to the crack growth rate until K_{Iscc} is reached, at which point the crack growth rate is enhanced above that in an inert environment. When all terms in Eq. 3 are active, the crack growth is accelerated at low stress intensity values and then enhanced further once K_{Iscc} is surpassed (Fig. 2.9c). It has been shown that many material-environment systems which exhibit corrosion fatigue behavior are not susceptible to stress corrosion cracking, or, at the stress intensity levels of interest in fatigue, do not exhibit stress corrosion cracking (88, 89).

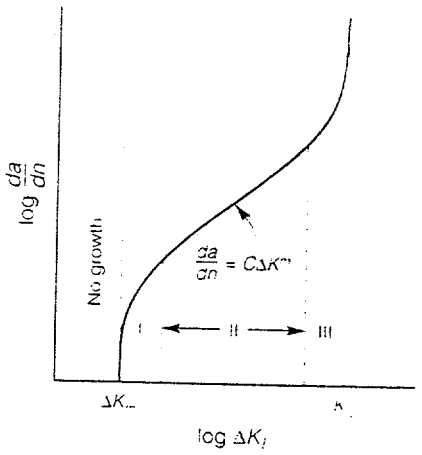

(a)

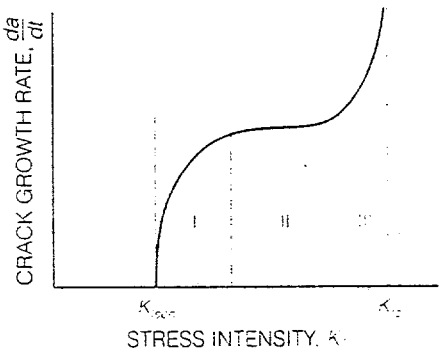

(b)

Fig. 2.8 Schematic representation of (a) purely mechanical fatigue crack growth and (b) stress corrosion cracking.

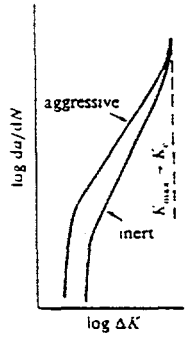

(a)

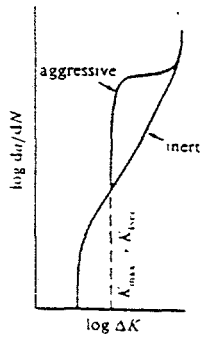

(b)

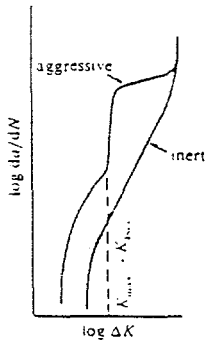

(c)

Fig. 2.9 Superposition of mechanical, stress corrosion cracking, and corrosion fatigue. (a) Mechanical fatigue and corrosion fatigue , (b) mechanical fatigue and stress corrosion cracking, (c) superposition of mechanical fatigue, corrosion fatigue, and stress corrosion cracking (87).

3 EXPERIMENTAL PROCEDURE

3.1 Alloy Composition and Heat Treatment

Four alloys were used in this study, an Fe-28%al-5%Cr alloy designated ternary, an Fe-28%al-5%Cr-1%Zr alloy designated 1%Zr, and two Fe-28%Al-5%Cr-0.5%Zr alloys, one with carbon and one without, designated 0.5%ZrC and 0.5%Zr, respectively. All the alloys are ordered Fe_3Al type intermetallics. The compositions of these alloys are listed in Table 1. All alloys were fabricated at Oak Ridge National Laboratory (ORNL) by vacuum induction melting, extrusion to 1.27 cm square bar, and hot rolling to the final thickness. The final plate thickness for all alloys used in this study was 4.75 mm. For tensile tests the material was extruded to a 1.08 cm diameter bar.

Due to the texture imparted by the rolling process the normal terms longitudinal, short transverse, and long transverse will be used to indicate the three perpendicular planes relative to the rolling direction. These planes are illustrated in Fig. 3.1, where the longitudinal plane is the rolling direction, and the short and long transverse planes are the remaining planes.

All alloys used in this study had the same B2 order. The annealing parameters for the B2 order consisted of a 700°C anneal for 1 hour with a mineral oil quench which was then repeated. This heat treatment was specified by ORNL in their research. It was used in this study so that data could be compared to those of other studies conducted by ORNL.

TABLE 1
Composition and Grain Size of Iron -Aluminide Alloys

	Atomic %			
	Ternary	1%Zr	0.5%ZrC	0.5%Zr
Fe	67.0	65.95	66.45	66.5
Al	28.0	28.0	28.0	28.0
Cr	5.0	5.0	5.0	5.0
Zr		1.0	0.5	0.5
C		0.05	0.05	
Grain Size	180μm	partially recrystallized	partially recrystallized	partially recrystallized

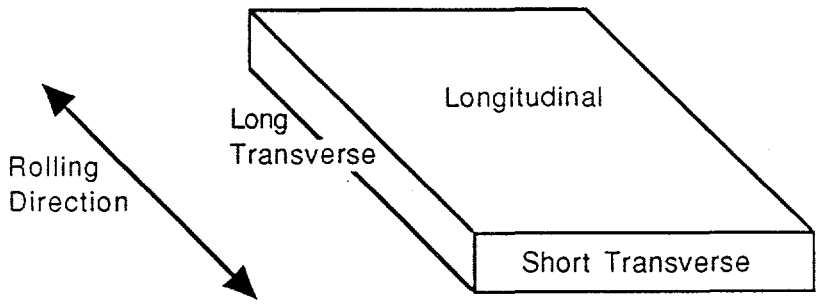

Fig. 3.1 Directional planes of a rolled plate.

Metallography

Metallography was performed on all alloys to examine the grain structure. Samples from the plates were sectioned using an abrasive wheel along longitudinal, short and long transverse directions, and then mounted in epoxy molds. Polishing was performed by first lapping the samples on a Lapmaster then on a water lubricated polishing wheel with 600 grit paper. They were then polished on cloth covered wheels containing 15μm and 9μm diamond paste, and finished on a felt covered wheel with 0.3μm alumina slurry with 10% oxilic acid. The metallographic specimens were then etched in glycerigia (30 ml glycerin, 30 ml HCl, 10 ml HNO_3) until the grain structure became visible. All photomicrographs were produced on a polarizing metallograph using Polaroid type 55 film.

3.2 Tensile Test

Tensile tests were performed on the ternary and 0.5%ZrC alloys in laboratory air, oxygen, and hydrogen, and in laboratory air only for 1%ZrC and 0.5%Zr. Tensile specimens were machined from rods with a diameter of 1.12 cm, or from plate material with a thickness of 0.5 mm with the specimen geometry shown in Fig. 3.2. The tension specimens were polished to a 0.3μm finish and ultra-sonically cleaned in acetone prior to testing.

The rod specimens were tested in a servo-hydraulic MTS machine fitted with a vacuum chamber, which allowed for testing in air, vacuum, or any controlled gas atmosphere. The samples were gripped using a split-type wedge grip shown in Fig. 3.3. The strain rate used in all tests was $3x10^{-4}$/sec. All tests were conducted at room temperature. One specimen was tested for each environment due to the limited

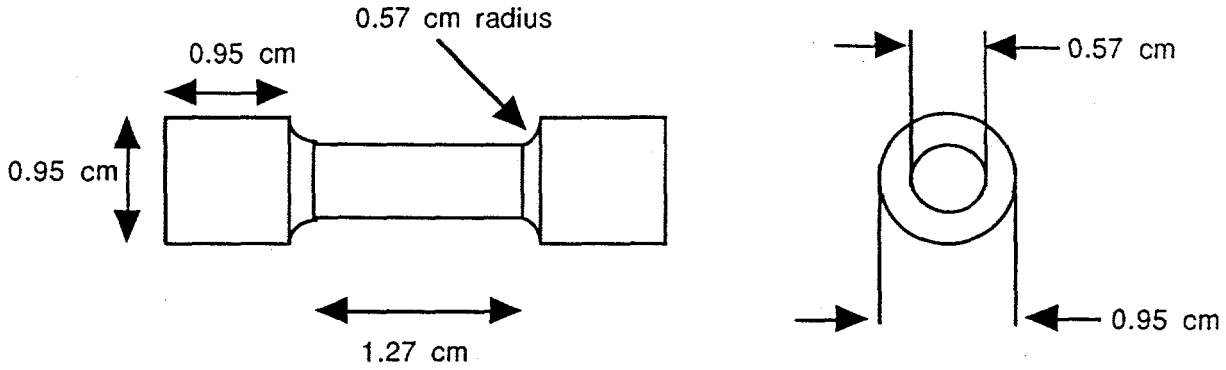

(a)

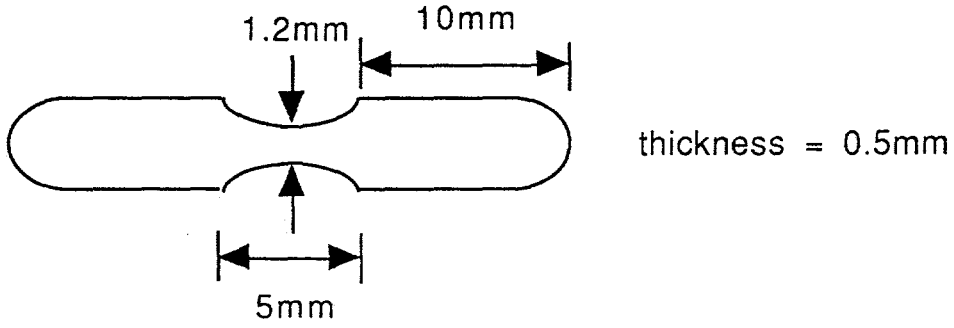

(b)

Fig. 3.2 Tensile specimen geometry for (a) the ternary and 0.5%ZrC, and (b) the 0.5%Zr and 1%ZrC alloys.

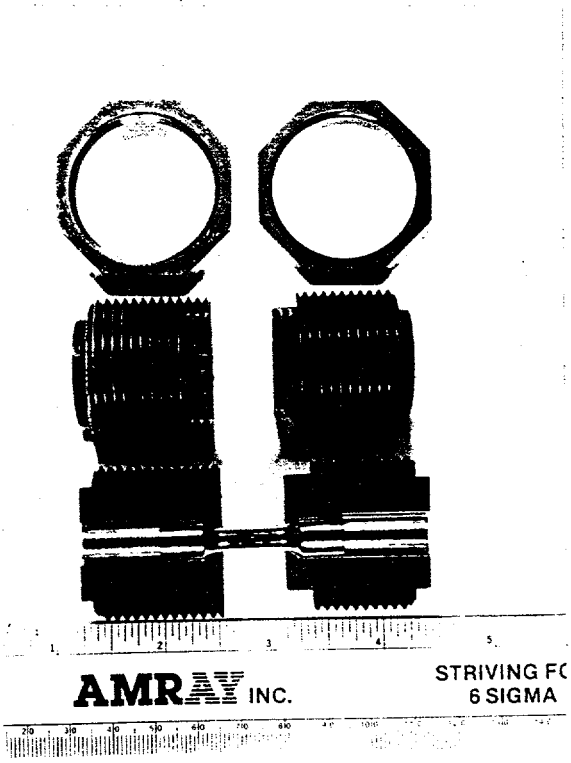

Fig. 3.3. Wedge grip used in tensile testing.

availability of material. The plate specimens were tested on a screw-driven Instron 4200 at the same strain rate.

When testing in oxygen or hydrogen gas, the environmental chamber was first evacuated to $< 6.6 \times 10^{-4}$ Pa using a diffusion pump fitted with a liquid nitrogen cold trap. The appropriate gas was then admitted to the chamber at a pressure of 2300 Pa over atmospheric pressure for 1 hour prior to testing. All gases used were of Ultra-High Purity Grade, with a maximum water vapor concentration of 3 ppm.

3.3 Fatigue Crack Growth Tests

Fatigue crack growth tests were performed on the ternary, 0.5%ZrC, 0.5%Zr, and 1%ZrC alloys in the B2 ordered state. All alloys were tested at room temperature in hydrogen gas and oxygen gas. The ternary alloy was tested in laboratory air while all other alloys were tested in constant humidity environments of 21%, 48%, and 81% relative humidity (rH).

When testing in a gaseous environment, the procedure previously described in section 3.2 for tensile tests was used. For testing in vacuum, the chamber was evacuated to $< 2 \times 10^{-3}$ Pa. For constant humidity tests, compressed air was bubbled through a closed beaker containing an aqueous solution of potassium acetate, potassium thiocyanate, or ammonium chloride which produced calculated values of 21%rH, 48%rH and 81%rH, respectively.

Compact tension specimens were used for all fatigue tests. The specimens were cut by electro-discharge machining such that the crack growth direction would be perpendicular to the rolling direction. Fig. 3.4 shows the specimen geometry. All specimens were polished to a 0.3μm finish and ultra-sonically cleaned in acetone prior to testing.

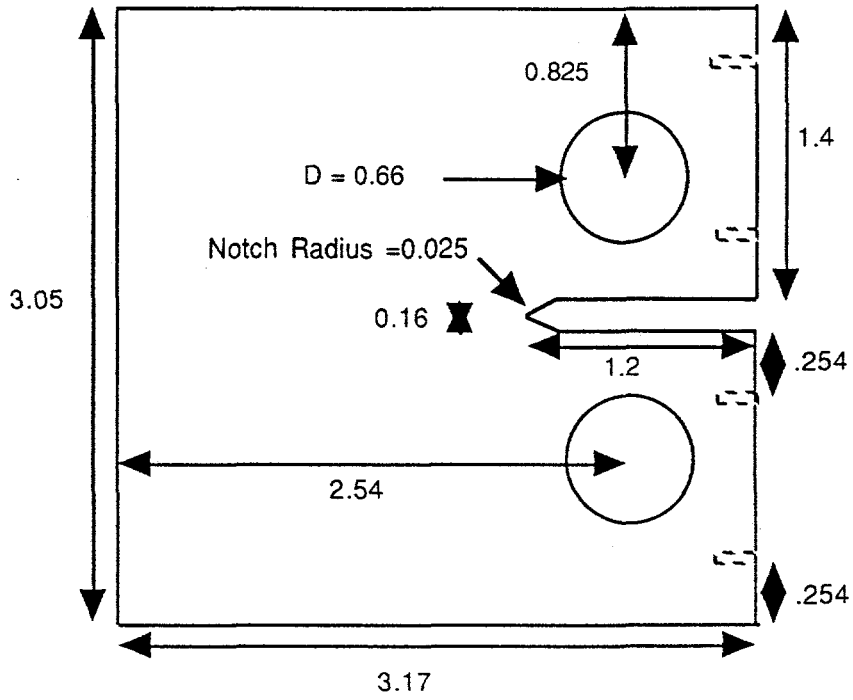

Fig. 3.4. Geometry of the compact tension specimens.

Crack length was monitored using the d.c. potential drop method. A Hewlett Packard power supply provided a 10 amp current to the specimen via two current leads positioned 11.5 mm on either side of the machined notch. The current was monitored by an IBM PC computer through a Metrabyte 12 bit analog to digital converter via a resistive shunt. The potential across the unbroken ligament was measured by two voltage probes located 2.5 mm on either side of the notch. The leads were connected to the compact tension specimen by brazing them into shallow holes drilled into the front face.

Calibration curves were generated to relate the crack length to the potential drop by optically measuring the crack length with a traveling microscope. The system was able to resolve changes in the crack length of 40 μm. The optical microscope, which had an accuracy of 20 μm, determined the accuracy of the crack measurements. Calibration curves were generated for each alloy in every test environment. An example of a calibration curve obtained for the 0.5%ZrC alloy is shown in Fig. 3.5.

The load frame used was an MTS servo-hydraulic machine with a 22,205 N load cell. Tests were run in load control using a sawtooth waveform with a frequency of 20Hz and an R ratio ($\sigma_{min}/\sigma_{max}$) of 0.5. The effect of frequency was investigated by fatiguing 0.5%ZrC at 20Hz, 2Hz, 0.2Hz and 0.08Hz.

Software written for a PC allowed a fully automated test procedure. The PC recorded load applied to the specimen, current, and voltage, and then calculated crack length, crack growth rate (da/dN), and stress intensity range (ΔK). The calculated values were used to produce the appropriate waveform. This digital waveform was then converted to analog and sent to the MTS as the load control input for the hydraulic system.

All parameters of the fatigue crack growth test followed ASTM E-647 (90) procedures. The fatigue crack growth testing procedure was as follows:

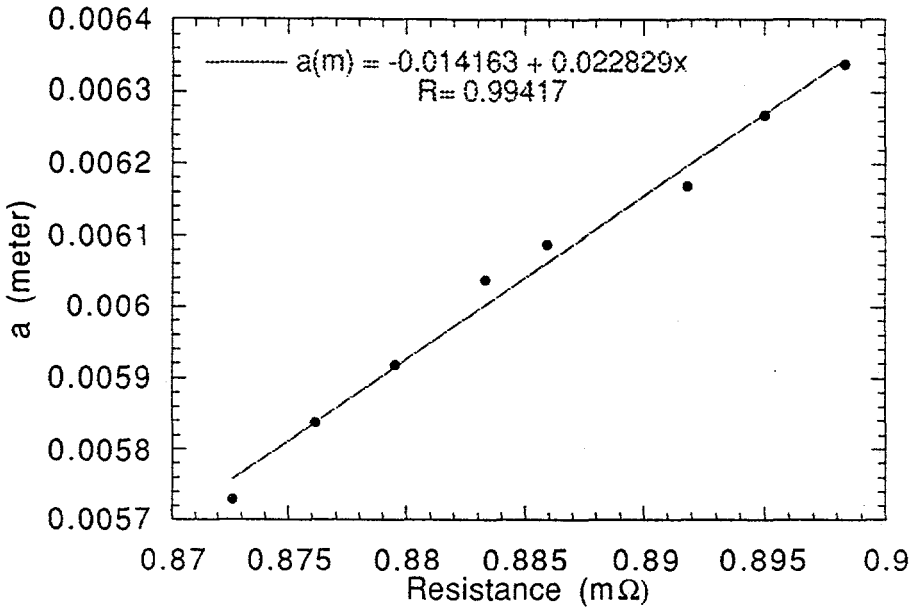

Fig. 3.5. Calibration curve relating the resistance to the crack length in 0.5%ZrC.

1) Precracking of the CT specimen by fatiguing in 20,000 cycle increments at stress intensity levels increasing by 0.5 MPa$\sqrt{m}$ until crack initiation was observed.

2) A ΔK-increasing procedure was employed until the crack had grown 1.0 mm from the 5.5 mm machined notch before data collection began.

3) A load shedding routine was then used to reduce the da/dN values back down to approximately 5×10^{-9} m/cycle to measure crack growth rates in the threshold region. This was the lowest growth rate that could be accurately and conveniently measured.

4) A ΔK-increasing routine was then continued until failure. Throughout the testing procedure, the R-ratio was held at 0.5 and total crack lengths were measured at crack growth intervals of 0.05 mm.

In accordance with ASTM E-647, the following equation for calculating stress intensity range, ΔK, was used:

$$\Delta K = \frac{\Delta P}{B\sqrt{W}} (0.886 + 4.64\alpha - 13.32\,\alpha^2 + 14.72\alpha^3 - 5.64\alpha^4) \qquad \text{Eq. 4}$$

In Eq. 4, ΔP is the cyclic load range, B is the specimen thickness, W is the specimen length from the edge to the center of the load-pin holes, and α is the ratio of crack length to W. The crack length is always measured from the center of the load-pin holes to the crack tip.

3.4 Microscopy

All specimen fracture surfaces were examined in a JOEL-840 scanning electron microscope (SEM) following failure. The fracture mode (cleavage, intergranular, dimpled, etc.) was noted. The specimens were mounted in a brass specimen holder using carbon tape to ensure electrical conductivity. The SEM was used with a working distance of 39 mm and an accelerating voltage of 20 kV. All SEM micrographs were taken with Polaroid # 55 film.

4 RESULTS

4.1 Grain Structure

The 1 hour, 700°C anneal used for all alloys resulted in a partially recrystallized structure for all the Zr-containing alloys. The anneal resulted in an increase in recrystallization from 40% in the as received to approximately 70% The grain structure was intentionally left partially unrecrystallized as it had been found by researchers at Oak Ridge National Laboratory to result in the highest ductility. In all micrographs, the black dots are due to preferential etching of sulfur-containing stringers, as well as, pitting of some dislocations. Figure 4.1a shows the as received 0.5%ZrC, while Fig. 4.1b shows the longitudinal plane of B2 ordered 0.5%ZrC. Figs. 4.2a and 4.2b show the longitudinal plane of the as received and B2 ordered 0.5%Zr, while Figs. 4.3a and 4.3b show the as received and B2 ordered 1%ZrC, also in the longitudinal plane. Large round precipitates (up to 10 μm in diameter) were seen in all Zr-containing alloys as shown in Fig. 4.4a. Electron dispersive x-ray analysis (EDX) was performed in the Joel 840 SEM on the precipitates and they were found to be Zr-rich (Fig. 4.4b). The precipitates were found to be non-homogeneously scattered throughout the material.

In the case of the ternary alloy, the 700°C anneal resulted in a near fully recrystallized structure with a grain size of 180 μm. The ternary grain structure is shown in Fig. 4.5a in the as received condition and in the B2 ordered structure in Fig. 4.5b. Notice that while the ternary alloy does retain some of the grain alignment imparted by the rolling process it does not have as strong a directional aspect as the Zr-containing alloys.

(a)

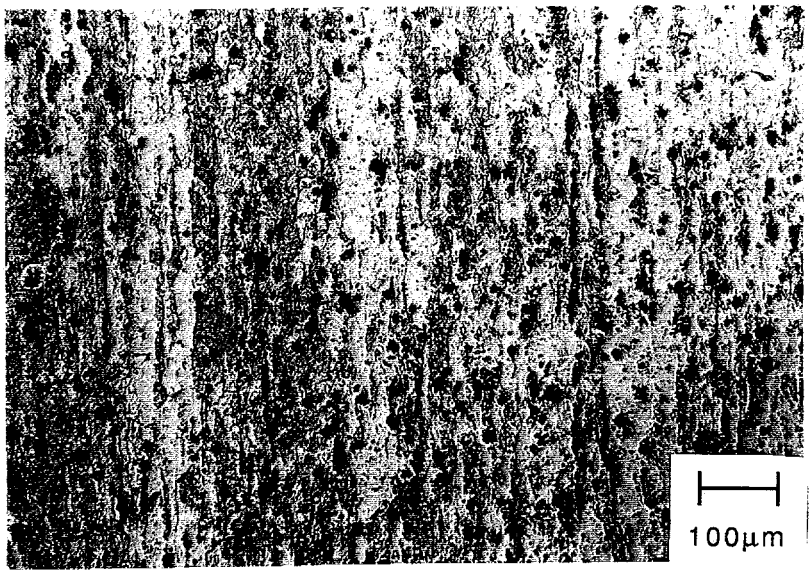

(b)

Fig. 4.1 Grain structure of the 0.5%ZrC alloy (a) in the as received condition and (b) B2 ordered.

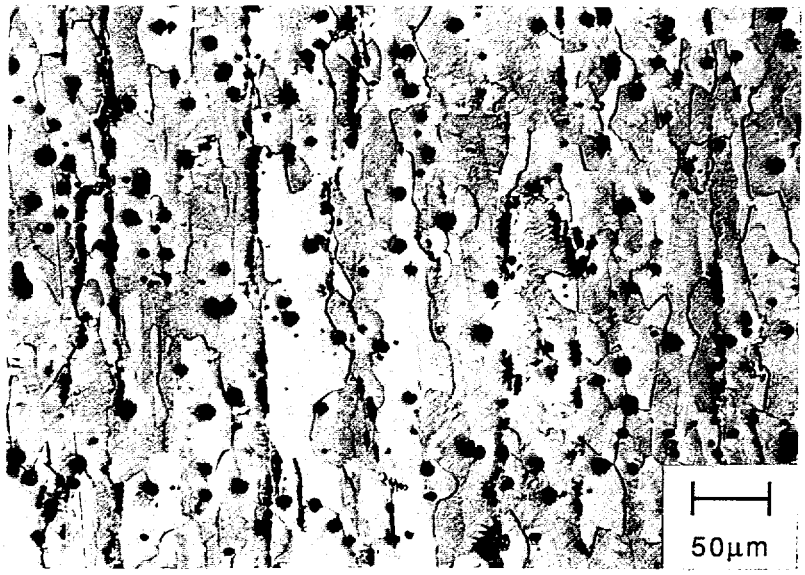

(a)

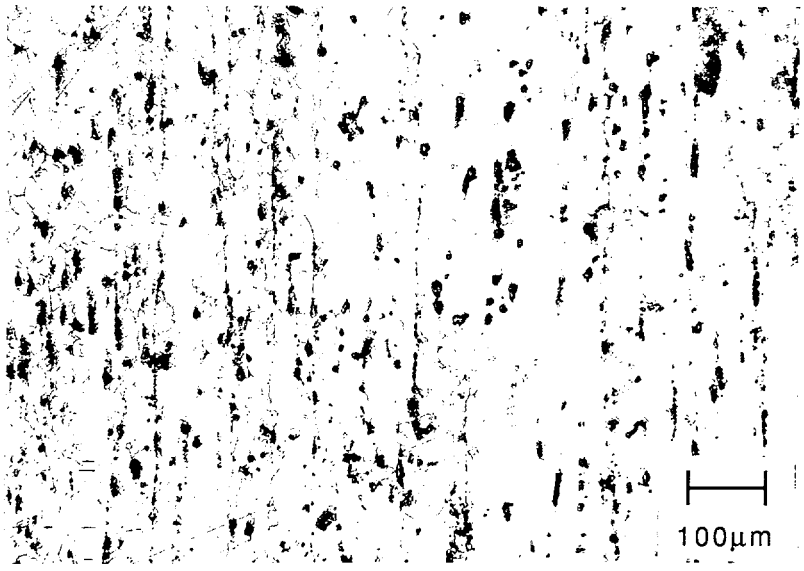

(b)

Fig. 4.2 Grain structure of the 0.5%Zr alloy (a) in the as received condition and (b) B2 ordered.

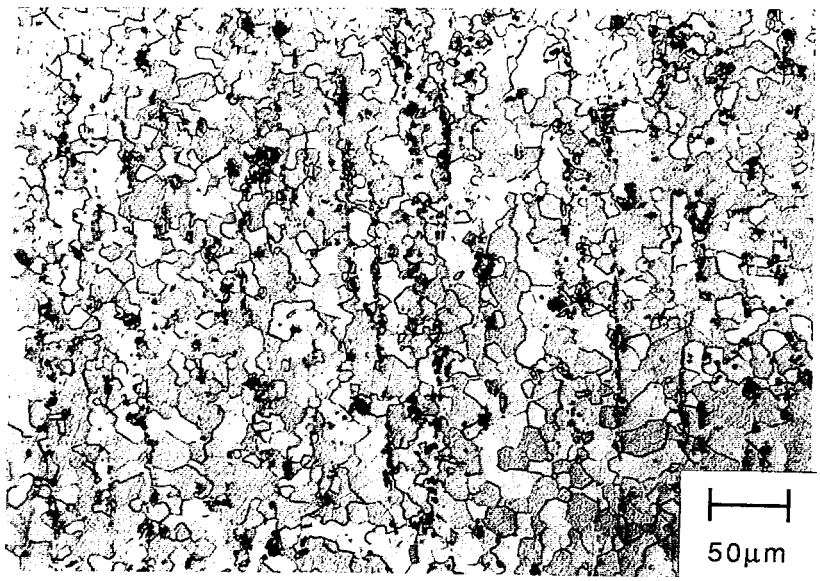

(a)

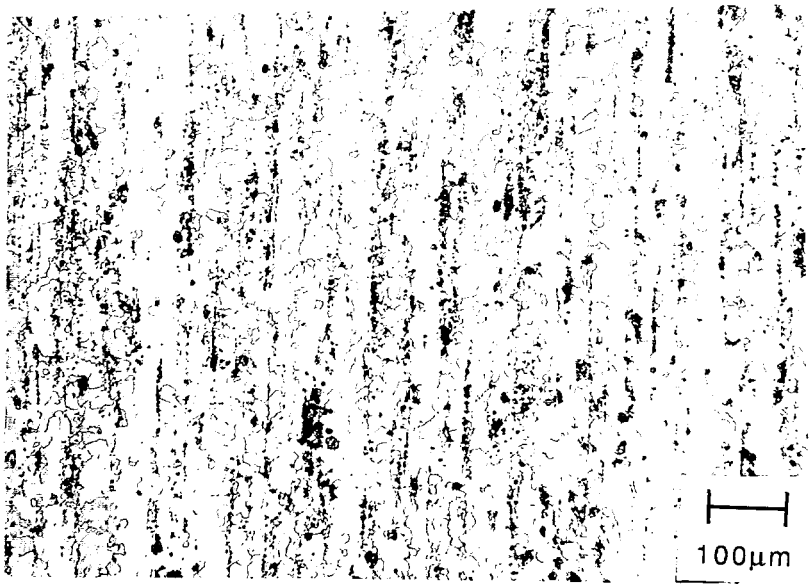

(b)

Fig. 4.3 Grain structure of the 1%ZrC alloy (a) in the as received condition and (b) B2 ordered.

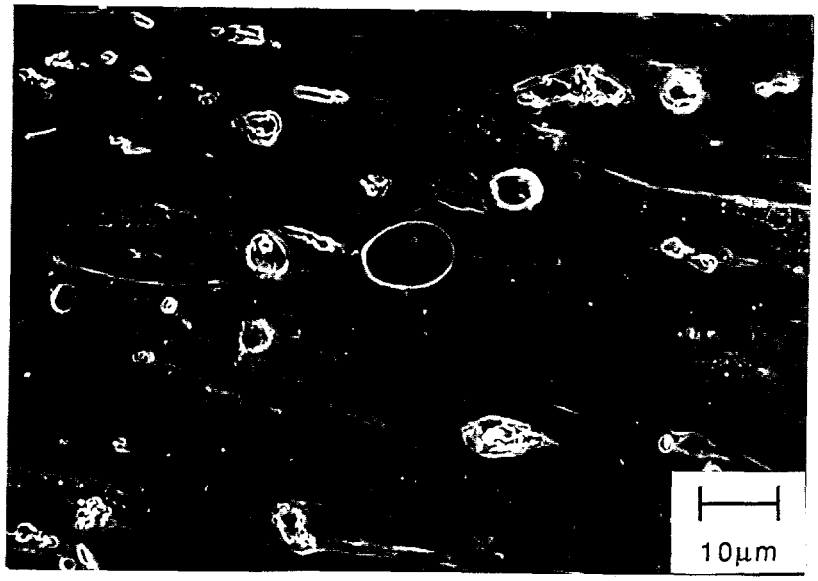

(a)

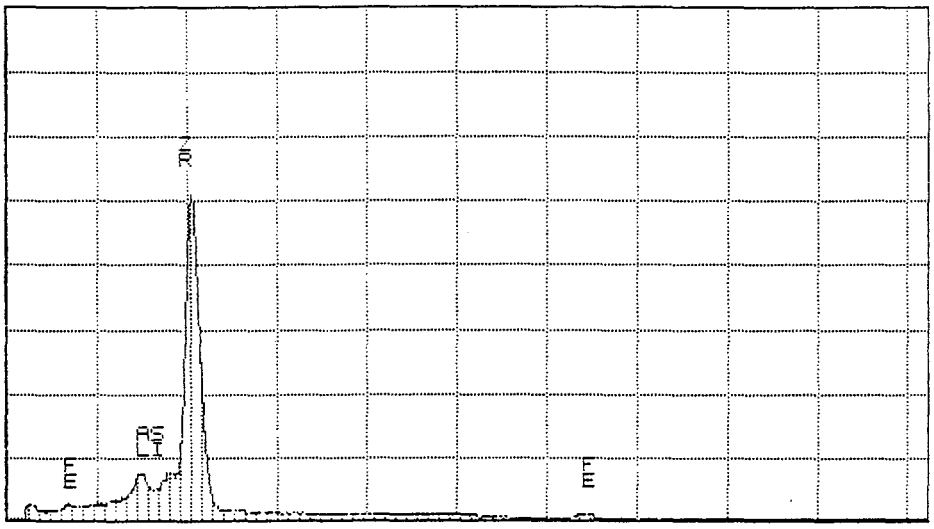

(b)

Fig. 4.4 (a) Round precipitate found in Zr-containing alloys (b) EDX spectrum showing the composition of the precipitate.

(a)

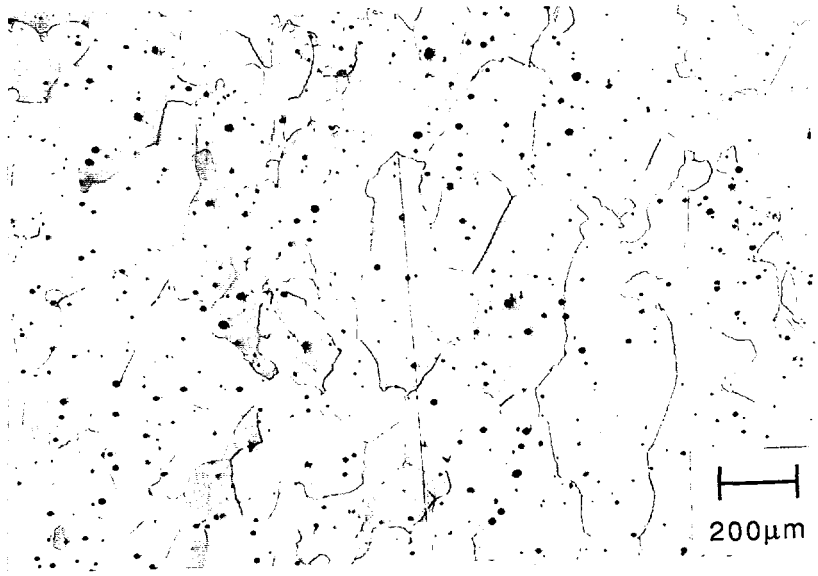

(b)

Fig. 4.5 Grain structure of the ternary alloy (a) in the as received condition and (b) B2 ordered.

4.2 Tensile Experiments

4.2.1 Tensile Properties of the Ternary Alloy

The tensile stress-strain curves for the ternary alloy tested at 25°C in air, hydrogen gas, and oxygen gas are shown in Fig 4.6. The tensile properties are summarized in Table 2.

The ductility and UTS were greatly reduced for the ternary alloy when tested in hydrogen gas as compared to testing in oxygen. The ductility in oxygen (12.0%) was reduced by 65% when tested in hydrogen (4.2%). Testing in air also resulted in a decrease of ductility compared to testing in oxygen. The ductility in air decreased from 12% in oxygen to 10.2% in air.

The UTS was significantly reduced in the embrittling environments. A decrease of 37% was observed between the oxygen (1180 MPa) and the hydrogen (740 MPa) environment. The UTS also decreased 17% between the oxygen (1180 MPa) and the air (980 MPa) environments. In all environments, the yield stress was not significantly affected.

Fracture topography was found to be relatively insensitive to environment, with the failure mode being mixed transgranular cleavage and intergranular fracture while the amount of intergranular facets increased as the environment became more aggressive. Figs. 4.7a-c show the fractography of the ternary alloy for air, oxygen gas, and hydrogen gas, respectively.

4.2.2 Tensile Properties of the Zr-Containing Alloys

The tensile stress-strain curves for 0.5%Zr and 1%ZrC tested in air at 25°C are shown in Fig 4.8, and the curves for the 0.5%ZrC alloy tested in air, hydrogen gas, and

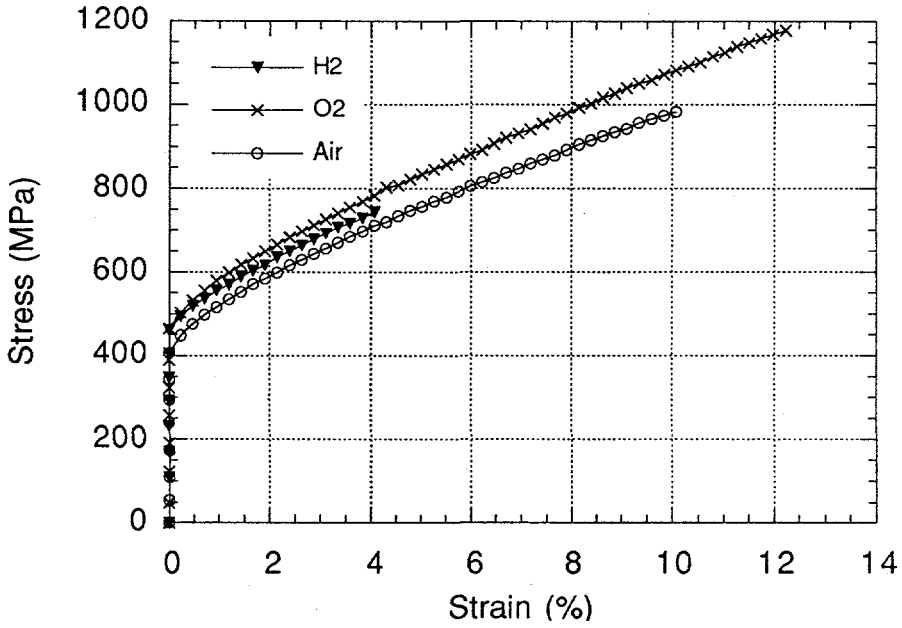

Fig. 4.6 Stress-strain curves for the ternary alloy tested in tension at 25°C.

TABLE 2
Tensile Properties of the Ternary Alloy

Environment	YS (MPa)	UTS (MPa)	Ductility (%)
Air	500	980	10.2
Oxygen	510	1180	12.0
Hydrogen	500	740	4.2

(a)

(b)

Fig. 4.7 Fracture surface of the ternary alloy tested in tension (a) in air and (b) in oxygen gas at 25°C.

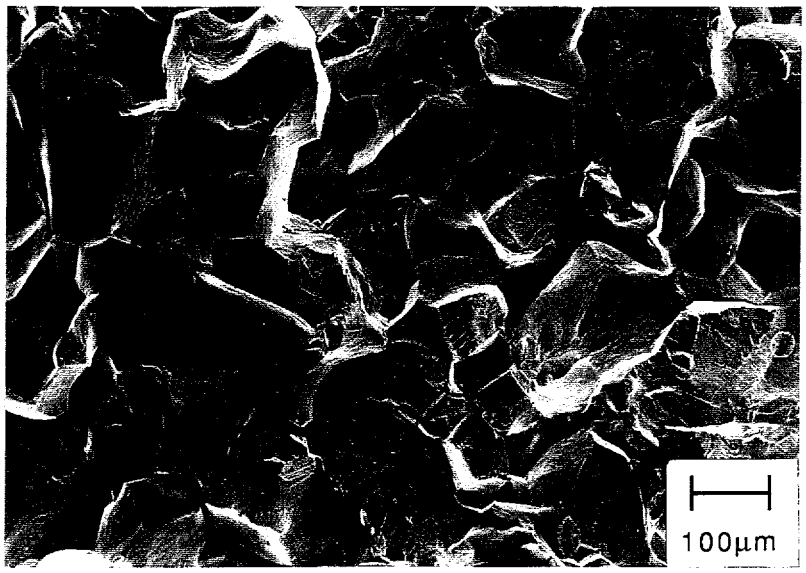

(c)

Fig. 4.7 continued — Fracture surface of the ternary alloy tested in tension in (c) hydrogen gas at 25°C.

oxygen gas at 25°C are shown in Fig. 4.9. The tensile data for the Zr-containing alloys are summarized in Table 3.

The 0.5%ZrC alloy exhibits significant embrittlement in hydrogen gas compared to testing in oxygen. The ductility in oxygen (13.1%) is reduced by over 50% when tested in hydrogen gas (6.1%). The 0.5%ZrC alloy does not show any degree of embrittlement in air, as the ductility is not significantly changed (Table 2).

The UTS was also greatly reduced by testing in hydrogen as compared to testing in oxygen. The UTS decreased 18% from 1460 MPa in oxygen to 1200 MPa in hydrogen. It was unaffected by testing in air compared to oxygen.

Increasing the amount of Zr to 1 at.% resulted in a decrease in both the ductility and the UTS when tested in air. The ductility decreased 61% from 13.8% in 0.5%ZrC to 5.3% in 1%ZrC. The UTS exhibited a decrease of 40% between 0.5%ZrC (1460 MPa) and 1%ZrC (880 MPa).

The absence of carbon in the 0.5%Zr alloy affected both the ductility and UTS in air. Without the carbon, there was a 40% drop in ductility compared to 0.5%ZrC. The UTS was decreased 31% between 0.5%ZrC (1460 MPa) and 0.5%Zr (1000 MPa).

The fracture surfaces of 0.5%ZrC in air, oxygen gas and hydrogen gas at 25°C are shown in Fig. 4.10a-c. The fracture mode of 0.5%ZrC was found to be mixed dimpled rupture and transgranular cleavage and was insensitive to environment, while the amount of transgranular cleavage increased as the environment became more aggressive. Fig. 4.11 shows that the fracture mode remained mixed dimpled rupture and transgranular cleavage in 0.5%Zr. The addition of Zr to 1 at.% resulted in a shift of fracture mode to mixed transgranular cleavage and intergranular fracture for 1%ZrC (Fig. 4.12). Fig. 4.13 shows the macroscopic appearance of a typical tensile tested specimen. The macroscopic characteristics of the fractured tensile specimens were typical of brittle failures with little

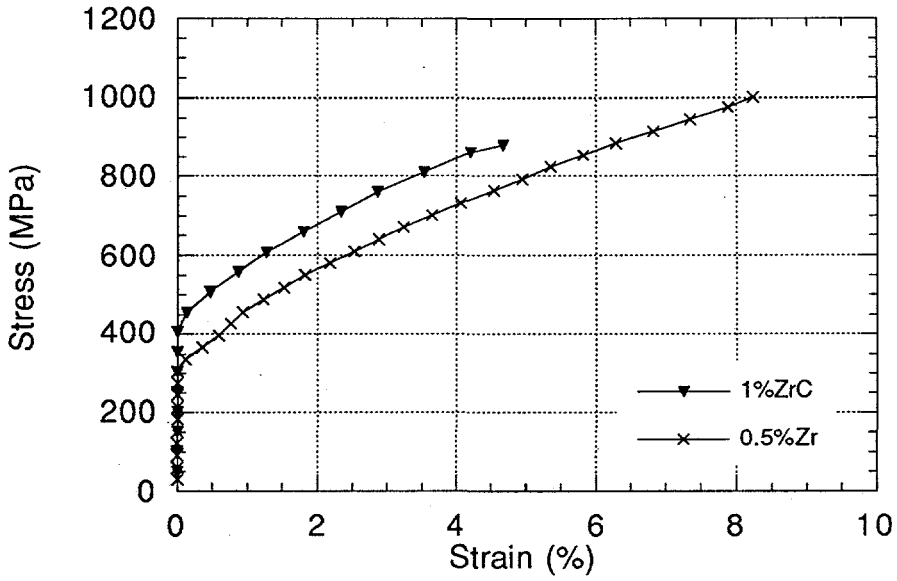

Fig. 4.8 Stress-strain curves for the 1%ZrC and the 0.5%Zr alloy tested in tension in air at 25°C.

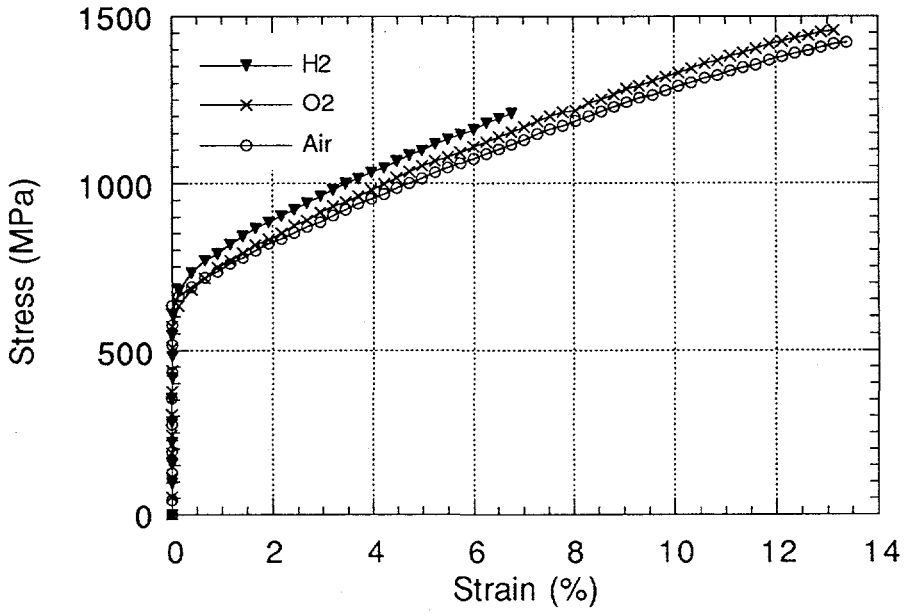

Fig. 4.9 Stress-strain curves for the 0.5%ZrC alloy tested in tension at 25°C.

TABLE 3.
Tensile Properties of Zr-Containing Alloys

Alloy	Air			O_2			H_2		
	YS (MPa)	UTS (MPa)	Ductility (%)	YS (MPa)	UTS (MPa)	Ductility (%)	YS (MPa)	UTS (MPa)	Ductility (%)
0.5%Zr *	670	1000	8.2	-	-	-	-	-	-
0.5%ZrC	690	1460	13.8	680	1460	13.1	680	1200	6.1
1%ZrC *	510	880	5.3	-	-	-	-	-	-

* Average of three tests

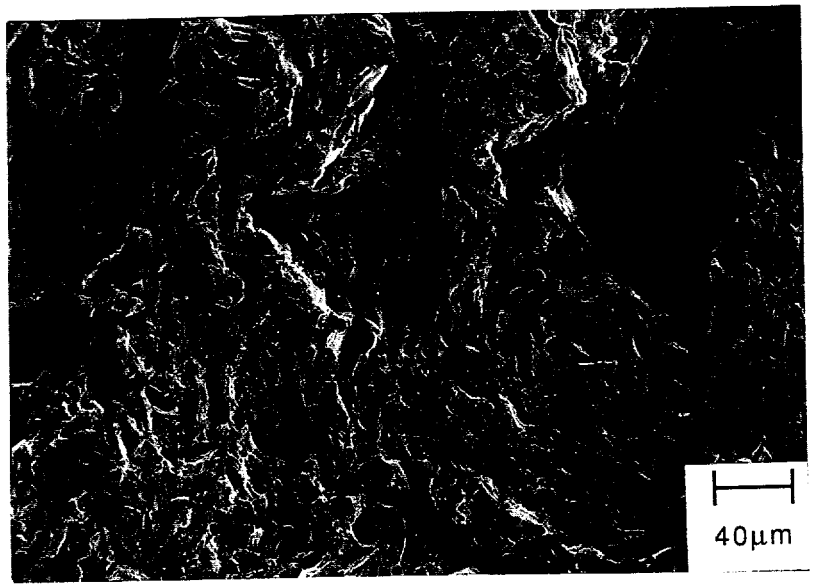

(a)

(b)

Fig. 4.10 Fracture surface of the 0.5%ZrC alloy tested in tension in (a) air and (b) in oxygen gas at 25°C.

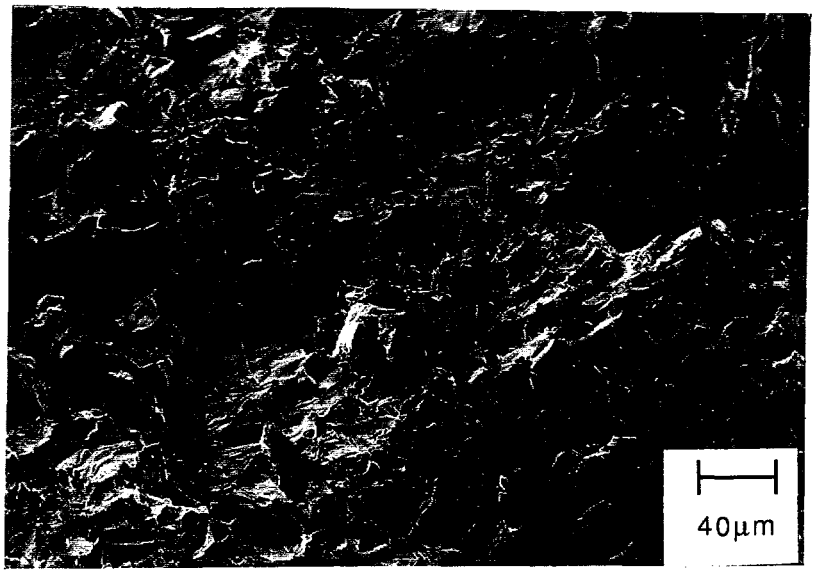

(c)

Fig. 4.10 continued Fracture surface of the 0.5%ZrC alloy tested in tension in (c) hydrogen gas at 25°C.

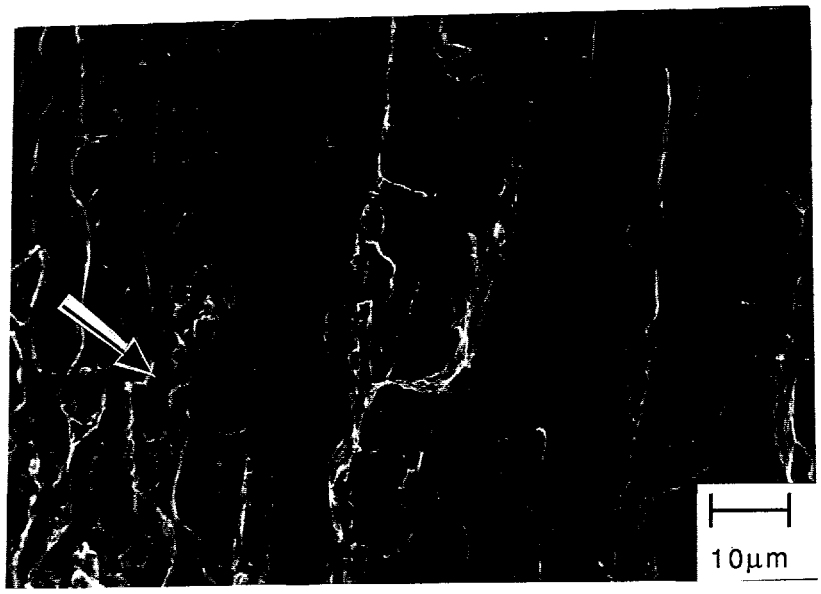

Fig. 4.11 Fracture surface of the 0.5%Zr alloy tested in tension in air at 25°C; arrow indicates dimples.

Fig. 4.12 Fracture surface of the 1%ZrC alloy tested in tension in air at 25°C.

Fig. 4.13 Macroscopic fracture surface of the 0.5%Zr alloy tested in tension in air; arrow indicates secondary cracking.

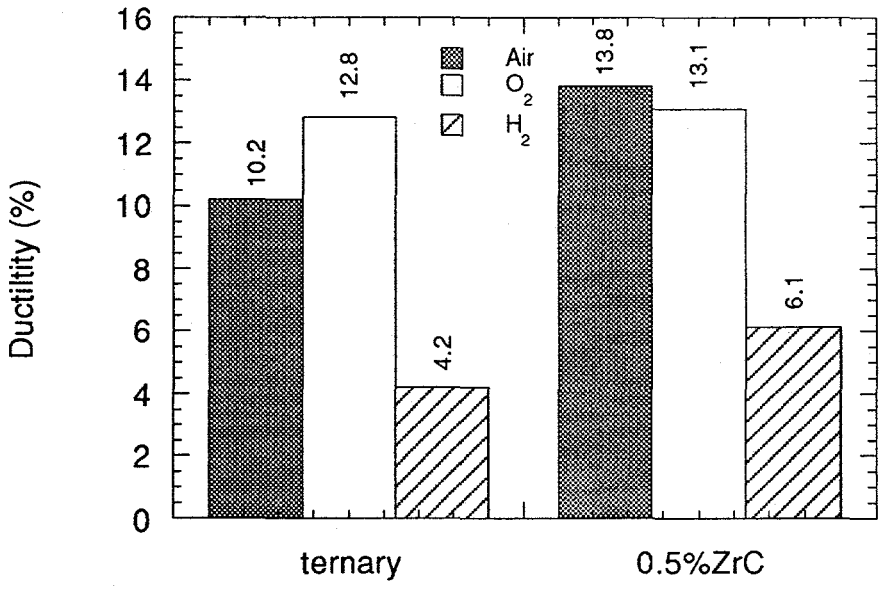

Fig. 4.14 Comparison of tensile ductility in the ternary and 0.5%ZrC alloys at 25°C.

reduction of area. Also, small secondary cracks were visible in the gauge section of the tensile specimens.

Fig. 4.14 shows a comparison of the ductility measured in the ternary and the 0.5%ZrC alloy. 0.5%ZrC exhibits a slightly higher ductility in oxygen than the ternary alloy but, unlike the ternary alloy, 0.5%ZrC is not embrittled by tensile testing in air. Similar ductilities were measured in oxygen (13.1%) and air (13.8%) for 0.5%ZrC, while a decrease between oxygen (12.0%) and air (10.2%) was measured in the ternary alloy. Both alloys were severely embrittled by tensile testing in hydrogen gas.

4.3 Fatigue Crack Growth Experiments

The threshold and critical stress intensities measured for the iron aluminides are listed in Table 4. The result of a single test is reported for each condition. The threshold stress intensity (ΔK_{th}) was taken to be the stress intensity range which produced a crack growth rate of $5x10^{-9}$ m/cycle. A linear region of the da/dN vs. ΔK curves used for the calculation of the Paris Slope, m, in:

$$da/dN = C(\Delta K)^m \qquad \text{Eq. 5}$$

could not consistently be defined. Therefore, the stress intensity necessary to produce a crack growth rate of 10^{-7} m/cycle was measured, $\Delta K(10^{-7})$, and is reported in Table 4.

4.3.1 Effect of Composition on Fatigue Crack Growth

Fatigue crack growth (FCG) curves in oxygen at room temperature for each alloy are shown in Fig. 4.15a, with duplicate tests for 0.5%ZrC in oxygen shown in Fig. 4.15b

TABLE 3.
FCG Data for the B2 Iron Aluminides

Alloy	Environment	ΔK (10^{-7}) (MPa$\sqrt{m}$)	ΔK_{TH} (MPa$\sqrt{m}$)	ΔK_C (MPa$\sqrt{m}$)
Ternary	Air (30% rH)	20.3	16.9	26.4
Ternary	O_2	38.4	24.2	42.4
Ternary	Vacuum	32.6	29.2	39.1
Ternary	H_2	15.1	14.2	19.9
0.5%ZrC	Air (21% rH)	29.0	18.0	59.4
0.5%ZrC	Air (48% rH)	27.1	18.0	47.4
0.5%ZrC	Air (81% rH)	24.3	17.9	37.2
0.5%ZrC	O_2	42.3	18.6	68.7
0.5%ZrC	Vacuum	29.0	23.2	38.0
0.5%ZrC	H_2	21.1	19.8	42.8
0.5%Zr	Air (21% rH)	28.1	18.7	39.0
0.5%Zr	Air (48% rH)	25.2	18.9	34.3
0.5%Zr	Air (81% rH)	23.9	19.2	32.2
0.5%Zr	O_2	43.3	20.0	48.9
0.5%Zr	Vacuum	32.6	32.5	46.1
0.5%Zr	H_2	21.2	20.5	38.9
1%ZrC	Air (21% rH)	22.8	16.2	27.6
1%ZrC	Air (48% rH)	21.2	16.7	27.1
1%ZrC	Air (81% rH)	20.2	17.1	23.6
1%ZrC	O_2	35.9	23.0	36.9
1%ZrC	Vacuum	30.4	26.9	35.1
1%ZrC	H_2	21.2	20.5	33.2

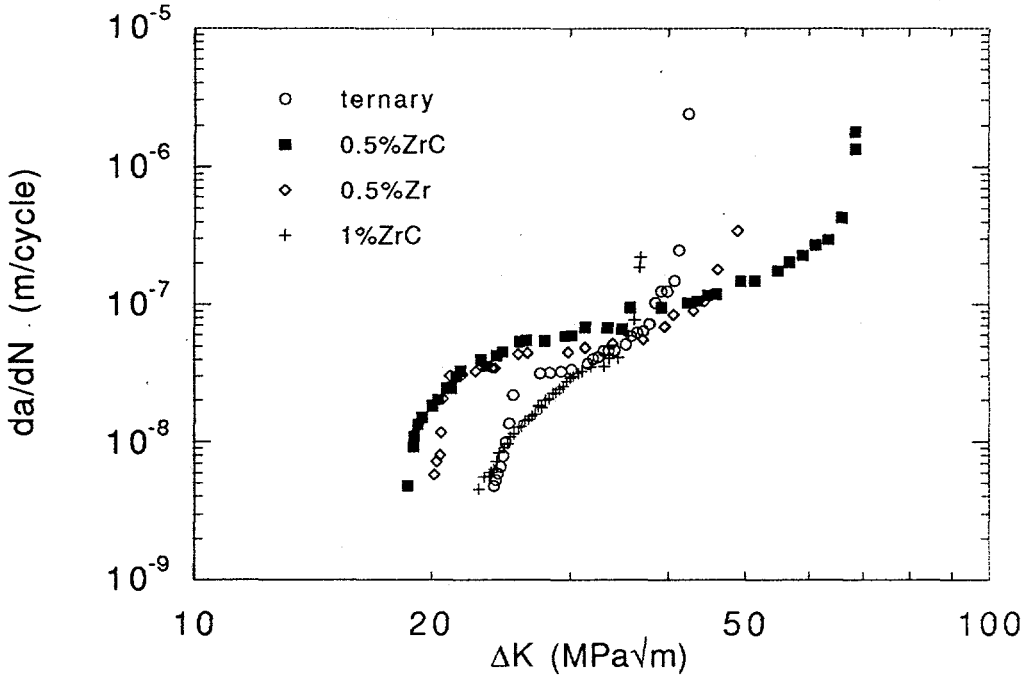

Fig. 4.15 (a) Comparison of FCG in the ternary, 0.5%ZrC, 0.5%Zr, and 1%ZrC alloys in oxygen gas at 25°C. Frequency = 20Hz, R = 0.5.

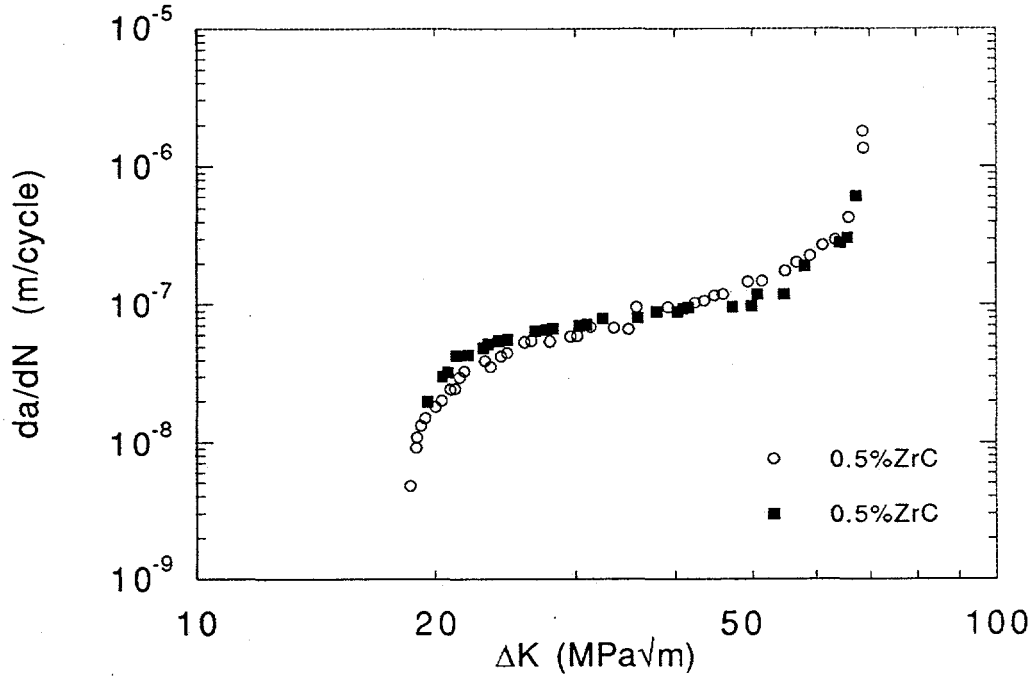

Fig. 4.15 continued (b) Duplicate FCG tests of 0.5%ZrC in oxygen gas at 25°C. Frequency = 20Hz, R = 0.5.

to illustrate the consistency of the FCG measurements. The FCG curves in oxygen are shown as it is considered to be the inert reference environment.

Fatigue crack growth resistance depends strongly on the alloy composition. 0.5%ZrC exhibited the best FCG resistance, with a ΔK_{th} of 18.6 MPa$\sqrt{m}$ and a ΔK_c of 68.7 MPa$\sqrt{m}$. Increasing the Zr content from 0.5 at.% to 1 at.% had a dramatic effect on the fatigue response. While the threshold stress intensity increased 24% in 1%ZrC, compared to 0.5%ZrC, the critical stress intensity was reduced by 46%. The absence of carbon had less of an effect on the FCG resistance. The threshold stress intensity of 0.5%Zr increased only 7% while the critical stress intensity was reduced 29%, as compared to 0.5%ZrC.

The lowest fatigue crack growth resistance was exhibited by both the 1%ZrC alloy and the ternary alloy, as they displayed very similar FCG behavior. The threshold stress intensity was higher by 30% compared to 0.5%ZrC while ΔK_c was reduced by 38% in these alloys.

4.3.2 Effect of Environment on Fatigue Crack Growth

Fatigue crack growth curves at room temperature in the four environments (laboratory air, oxygen gas, hydrogen gas, and vacuum) are shown in Fig. 4.17 for the ternary alloy; Fig. 4.18 for 0.5%ZrC, Fig. 4.19 for 0.5%Zr, and Fig. 4.20 for 1%ZrC. Fig. 4.16 show the a vs. N curves for the ternary alloy in the four environments. The data for the other alloys was not presented in the a vs. N form as it is evident that the same trend occurs for all alloys.

The higher fatigue life in oxygen as compared to all other environments is clearly shown in Fig. 4.16. In oxygen the fatigue life is 2.5×10^5 cycles while it decreased to 1.1×10^5 cycles in air. The embrittling effect of hydrogen is evident in the decrease in

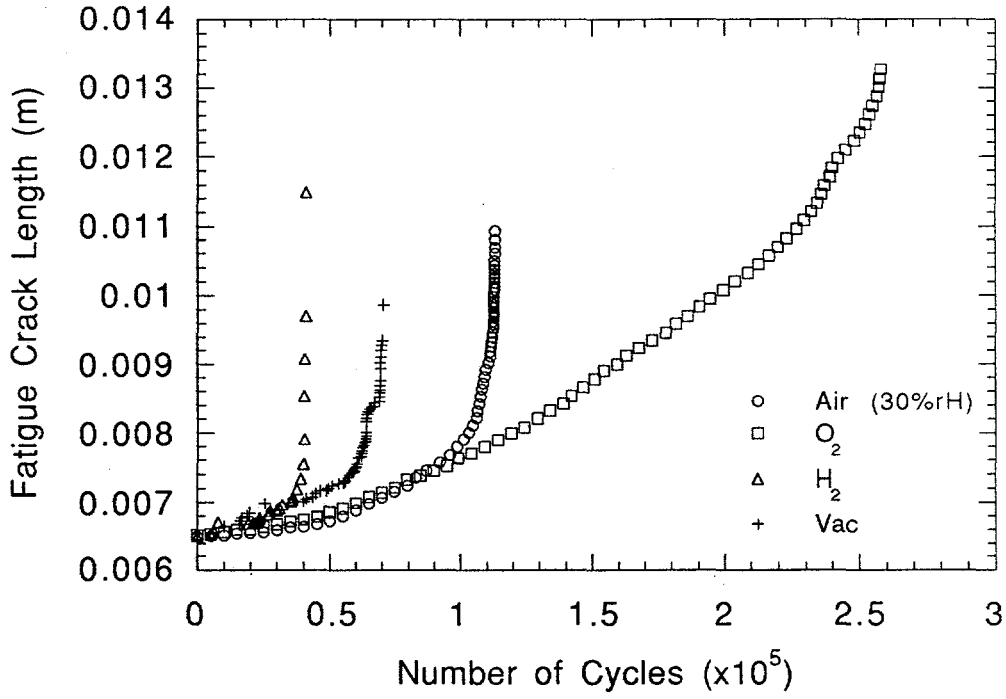

Fig. 4.16 a vs. N curves for the ternary alloy at 25°C. Frequency = 20Hz, R = 0.5.

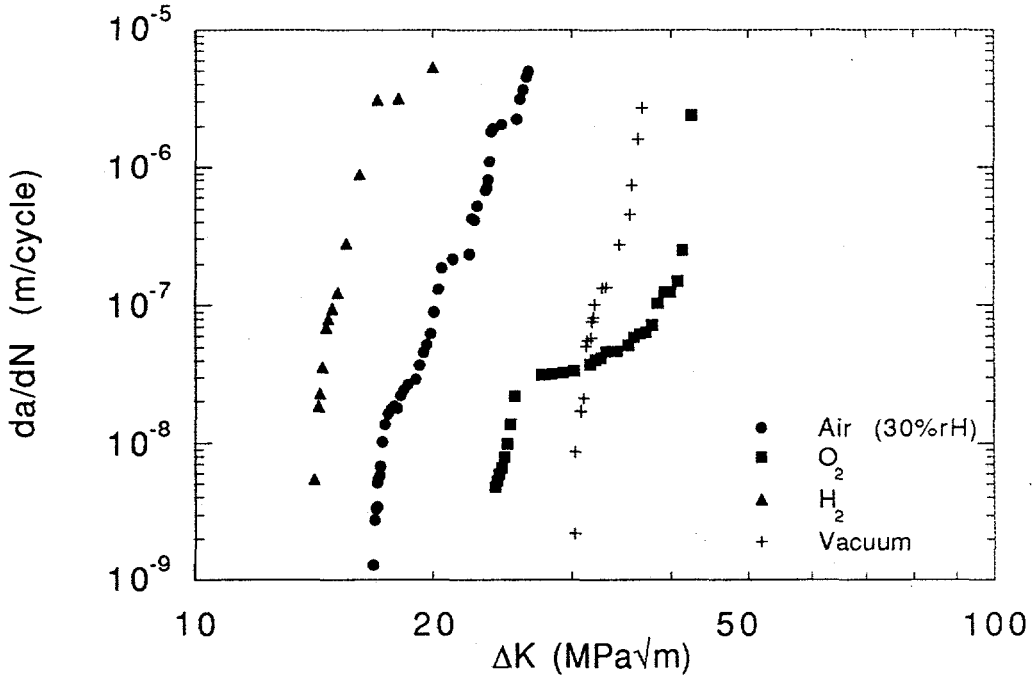

Fig. 4.17 Fatigue crack growth curves for the ternary alloy at 25°C. Frequency = 20Hz, R = 0.5.

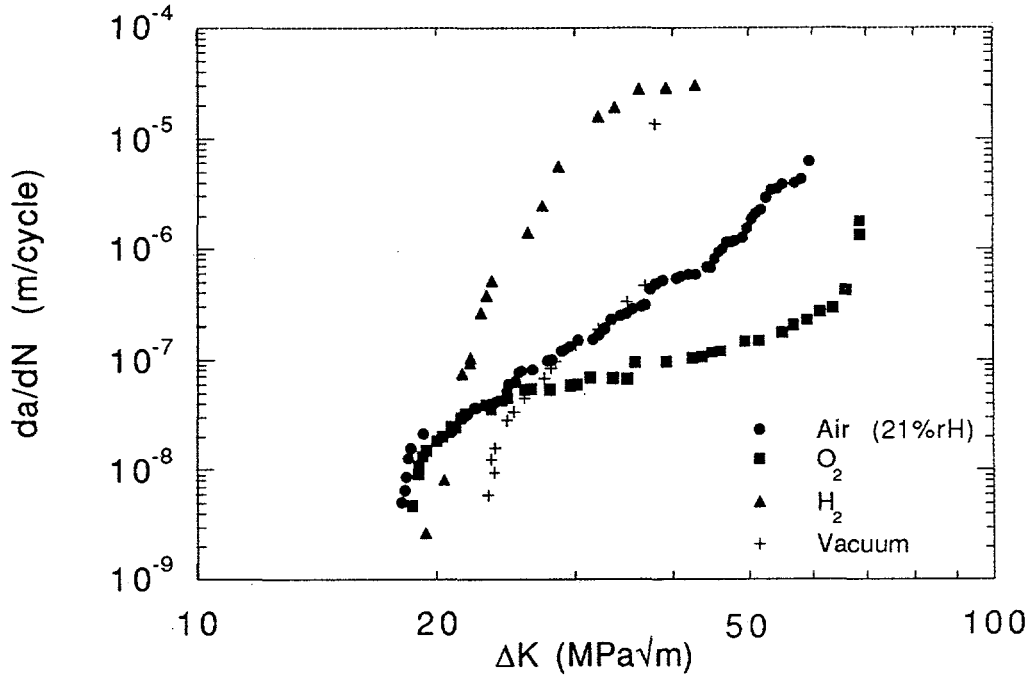

Fig. 4.18 Fatigue crack growth curves for 0.5%ZrC at 25°C. Frequency = 20Hz, R = 0.5.

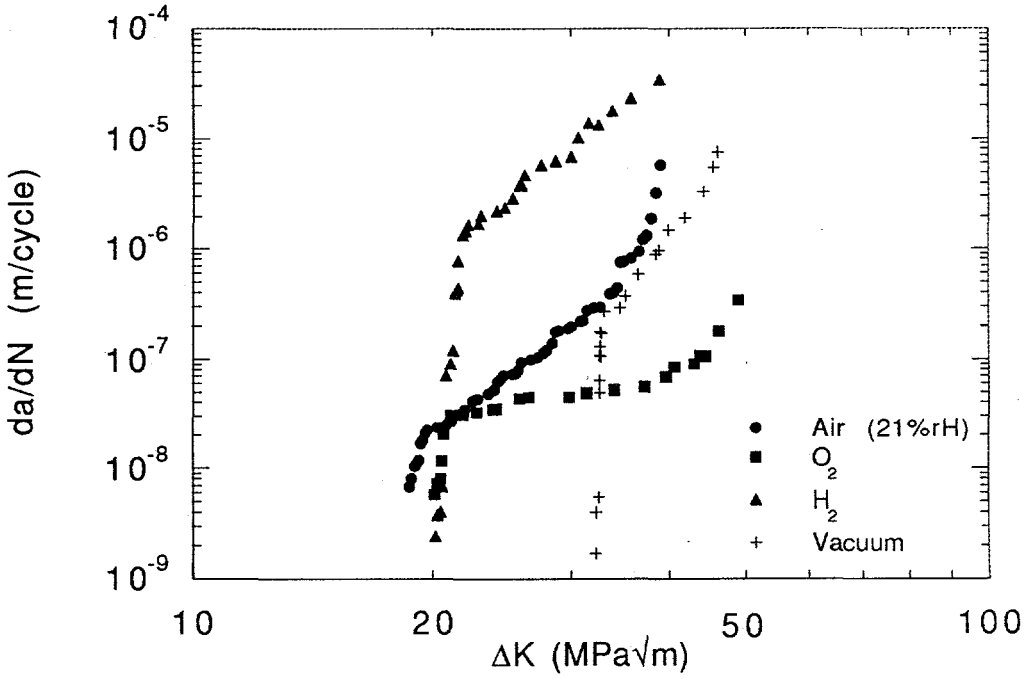

Fig. 4.19 Fatigue crack growth curves for 0.5%Zr at 25°C. Frequency = 20Hz, R = 0.5.

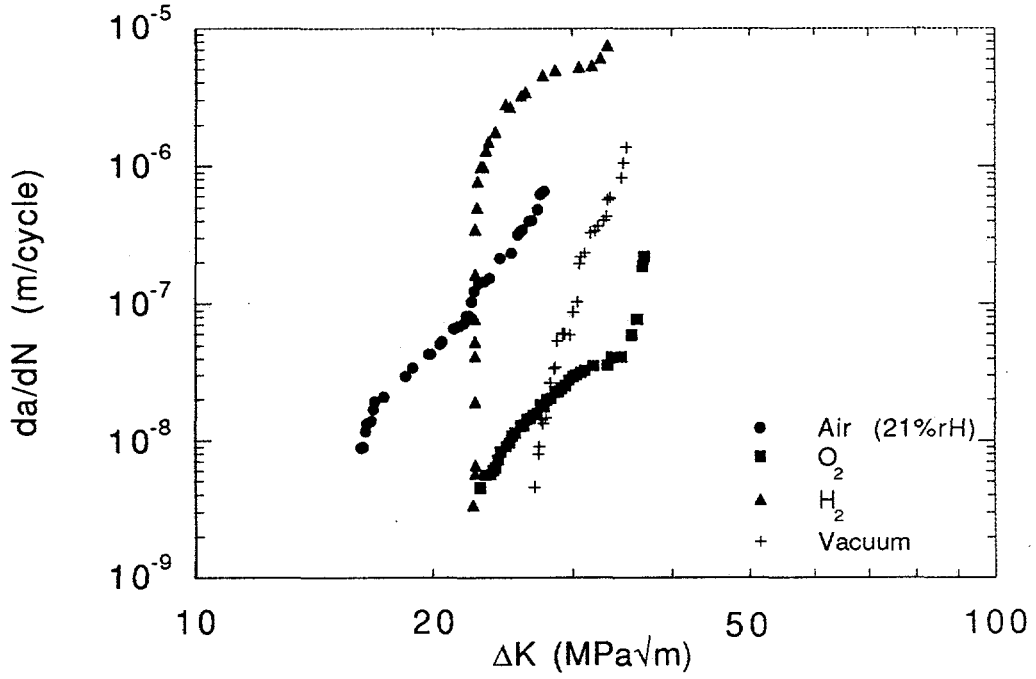

Fig. 4.20 Fatigue crack growth curves for 1%ZrC at 25°C. Frequency = 20Hz, R = 0.5.

fatigue life compared to oxygen, as well as, the low fatigue life ($0.4x10^5$ cycles) when tested in hydrogen gas.

Table 3 and Figs. 4.17-4.20 show that hydrogen is clearly an embrittling environment for FCG. In all alloys, $\Delta K(10^{-7})$ and ΔK_c are lower in hydrogen than in oxygen. While it is obvious that hydrogen gas is extremely embrittling, ΔK_{th} for all Zr-containing alloys is higher in hydrogen gas than in laboratory air. The FCG curves in hydrogen also display the typical behavior ascribed to the synergistic effects of mechanical fatigue and corrosion fatigue (Fig. 2.8a).

While testing in vacuum proved to be detrimental to the fatigue crack growth resistance for all alloys, it resulted in the highest threshold stress intensities. Figs. 4.17-4.20 clearly show the drastic increase in FCG rates in vacuum compared to oxygen. The threshold stress intensities of all alloys were higher in vacuum than in oxygen, but the fatigue crack growth resistance was much lower. In all alloys tested a cross-over was seen in the FCG curves in oxygen and vacuum. The largest effect of testing in vacuum was seen in 0.5%ZrC where the reduction in $\Delta K(10^{-7})$ was 31% and in ΔK_c was 45%.

Testing in laboratory air was found to be embrittling for all alloys as well. However, the degree of embrittlement in air was less than that in hydrogen. In 0.5%ZrC, for example, $\Delta K(10^{-7})$ and ΔK_c are reduced by 31% and 13%, respectively, in air as compared to oxygen gas. However, testing in hydrogen gas reduced $\Delta K(10^{-7})$ by 50% and ΔK_c by 38%.

The Zr-containing alloys exhibited similar degrees of embrittlement in air with a trend of increasing embrittlement with increased Zr content. ΔK_{th} was reduced 3% in 0.5%ZrC, 6% in 0.5%Zr and 30% in 1%ZrC, while ΔK_c was reduced 13% in 0.5%ZrC, 20% in 0.5%Zr, and 25% in 1%ZrC, as compared to oxygen. The ternary alloy was the most severely embrittled in air with ΔK_{th} reduced 30% and ΔK_c reduced 38%.

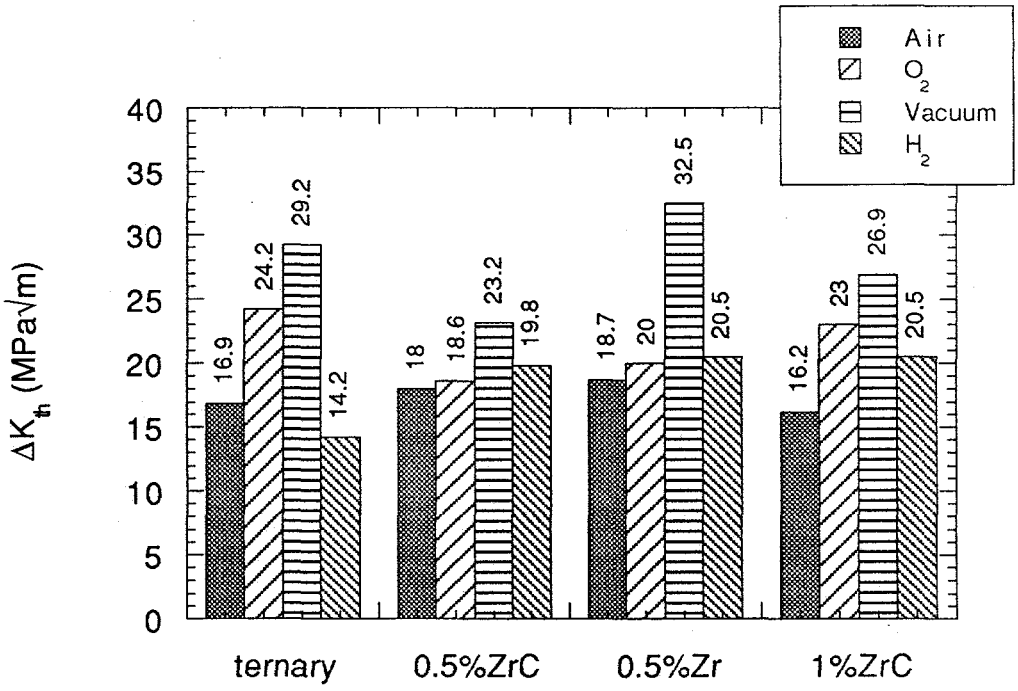

Fig. 4.21 Summary of threshold stress intensities in iron aluminides fatigued at 25°C. Frequency = 20Hz, R = 0.5.

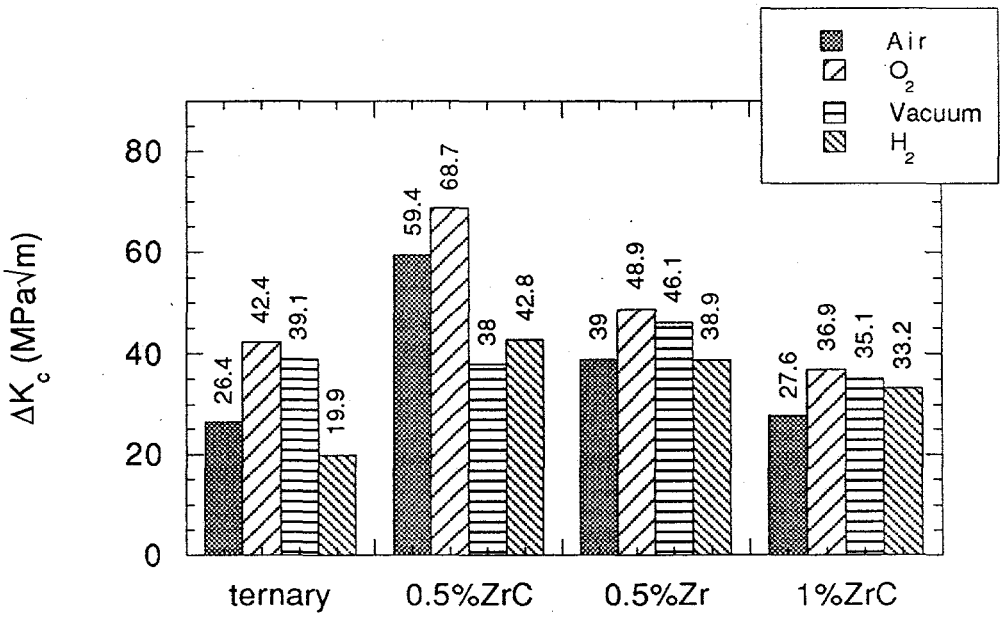

Fig. 4.22 Summary of critical stress intensities in iron aluminides fatigued at 25°C. Frequency = 20Hz, R = 0.5.

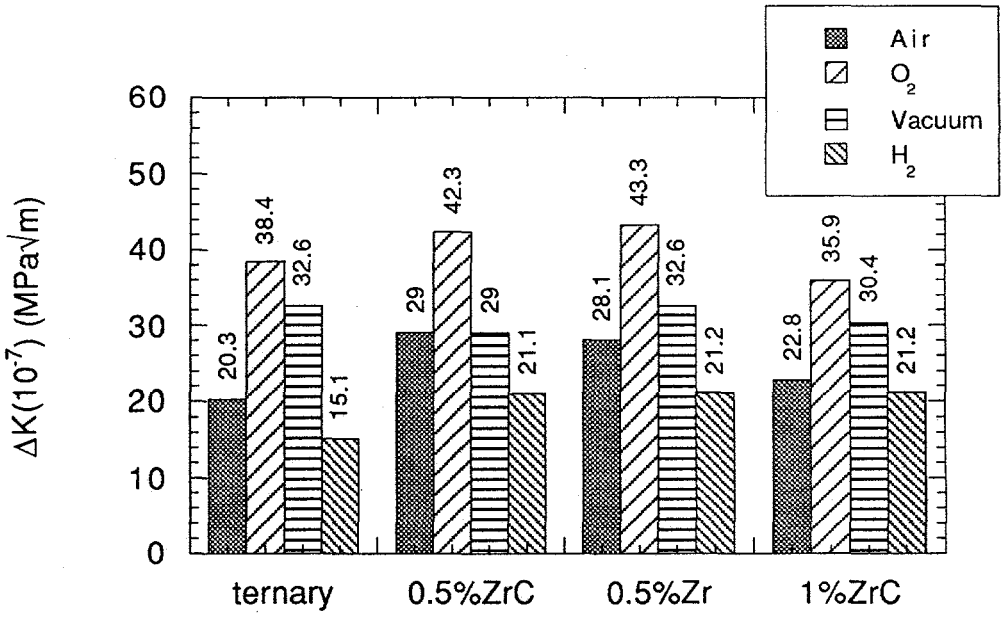

Fig. 4.23 Summary of stress intensities required to achieve a crack growth rate of 10^{-7} m/cycle in iron aluminides fatigued at 25°C. Frequency = 20Hz, R = 0.5.

Figs. 4.21 and 4.22 show a summary of ΔK_{th} and ΔK_c for each alloy in air, oxygen gas, vacuum and hydrogen gas at 25°C. A summary of $\Delta K(10^{-7})$ for each alloy in each test condition is shown in Fig. 4.23. It should be noted that ΔK_{th} and $\Delta K(10^{-7})$ were similar for each environment in both the 0.5 at.% Zr alloys, with the exception vacuum.

4.3.3 Effect of Humidity on Fatigue Crack Growth

The effect of increased humidity on the FCG resistance in 0.5%ZrC, 0.5%Zr and 1%ZrC are shown in Figs. 4.24-4.26. The fatigue tests conducted in oxygen are also shown in these figures, as it is considered the inert reference environment.

An increase in humidity level had no effect on ΔK_{th} in 0.5%ZrC (Table 4). $\Delta K(10^{-7})$ was reduced 16% from 29.0 MPa$\sqrt{m}$ in 21%rH air to 24.3 MPa$\sqrt{m}$ in 81%rH. The embrittling effect of increased humidity was evident in 0.5%ZrC as ΔK_c was reduced from 59.4 MPa$\sqrt{m}$ to 37.2 MPa$\sqrt{m}$ (Fig. 4.24).

The absence of C in 0.5%Zr resulted in a decreased degree of embrittlement with increased humidity (Fig. 4.25). ΔK_{th} was increased 3% from 21%rH to 81%rH while both $\Delta K(10^{-7})$ and ΔK_c were reduced by 16%. ΔK_c was reduced from 39 MPa$\sqrt{m}$ in 21%rH to 32.2 MPa$\sqrt{m}$ in 81%rH.

The increase in zirconium in 1%ZrC also resulted in less embrittlement as ΔK_c only decreased 14% with a change in humidity from 21%rH (27.6 MPa$\sqrt{m}$) to 81%rH (23.6 MPa$\sqrt{m}$) (Table 4). 1%ZrC also exhibited an increase in ΔK_{th} of 5% as the humidity level was increased (Fig. 4.26). $\Delta K(10^{-7})$ was reduced in 1%ZrC from 22.8 MPa$\sqrt{m}$ to 20.2 MPa$\sqrt{m}$ in 21%rH and 81%rH, respectively.

4.3.4 Effect of Frequency on Fatigue Crack Growth

The effect of decreasing the test frequency for the 0.5%ZrC alloy is shown in Fig. 4.27. All tests were run at a constant humidity level of 21%rH. Also shown is the fatigue

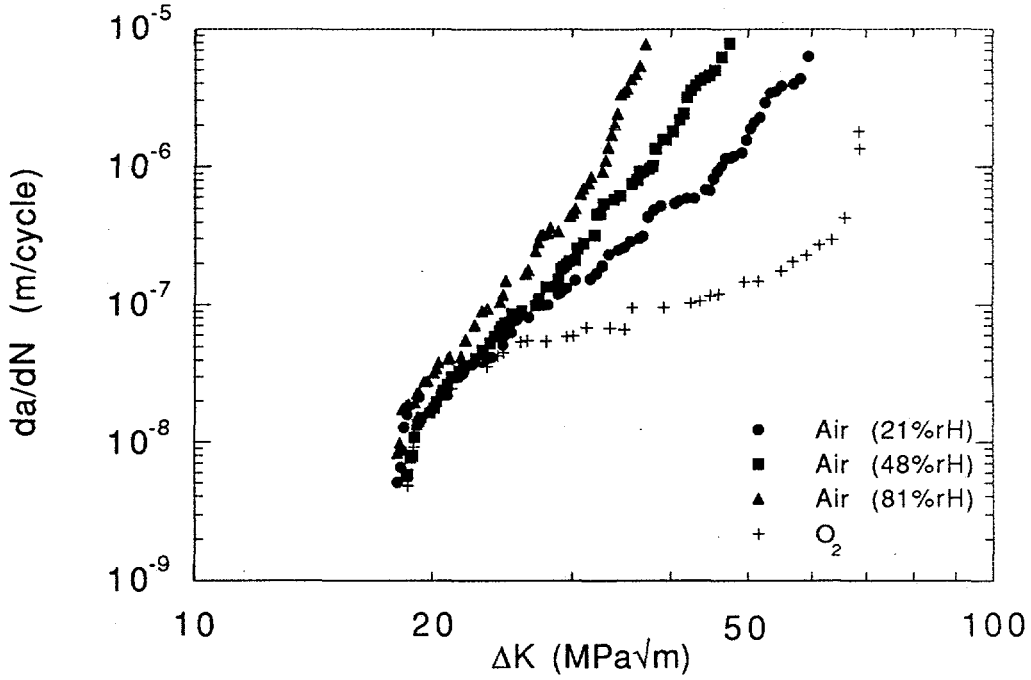

Fig. 4.24 Fatigue crack growth curves for 0.5%ZrC in air at 25°C.

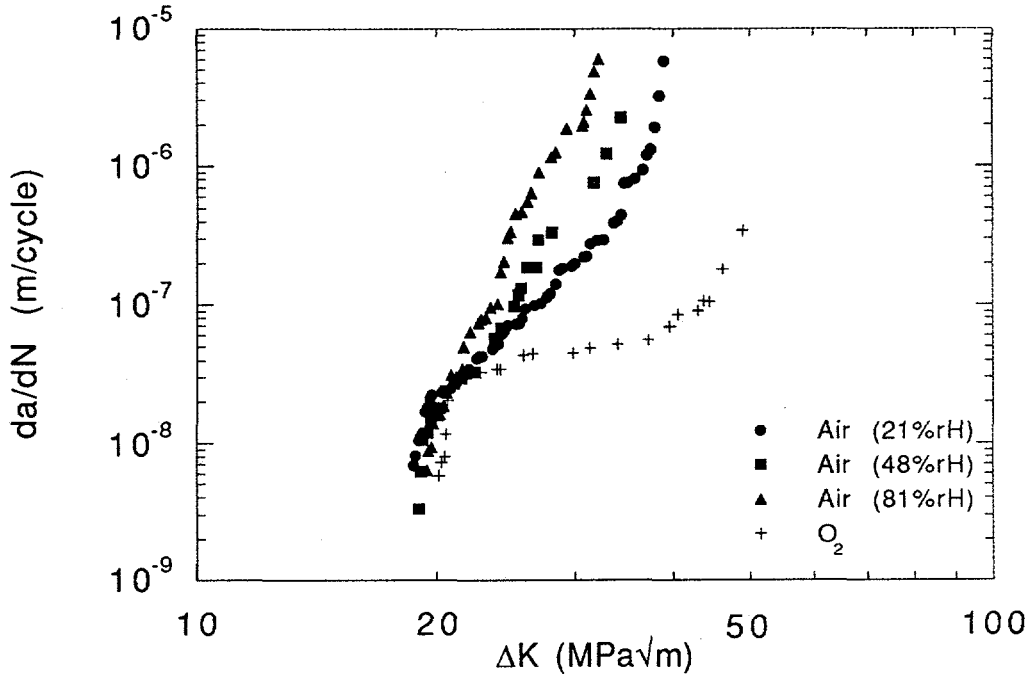

Fig. 4.25 Fatigue crack growth curves for 0.5%Zr in air at 25°C.

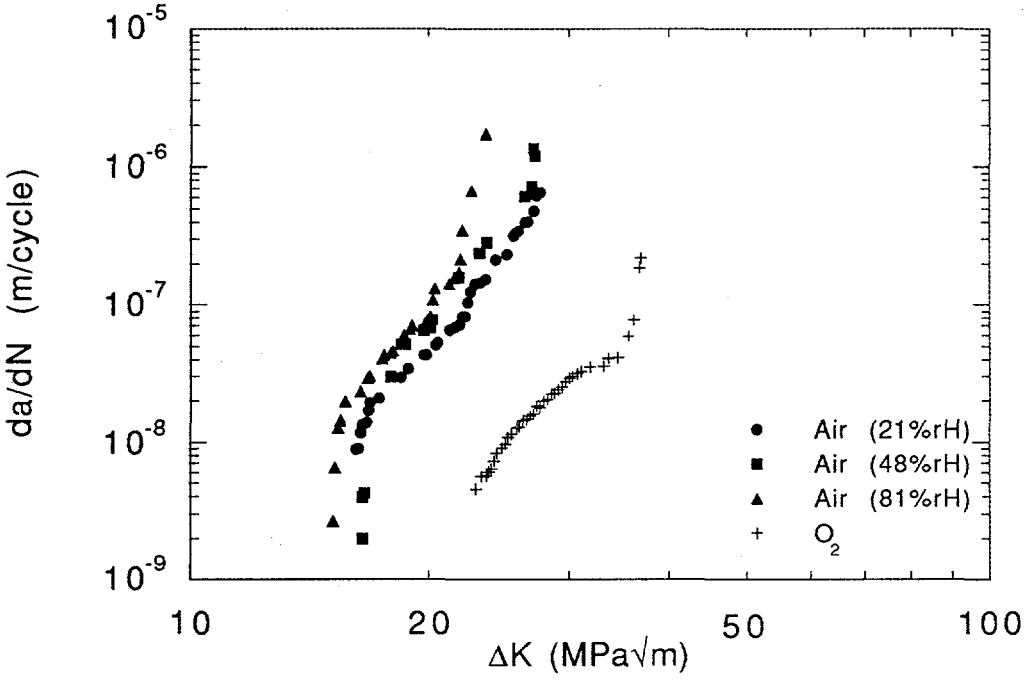

Fig. 4.26 Fatigue crack growth curves for 1%ZrC in air at 25°C.

test conducted in oxygen, which is considered the inert environment for determining the magnitude of crack growth enhancement.

As can be seen in Fig. 4.27, the lower frequencies enhanced fatigue crack growth, as well as had a significant effect on both the threshold and critical stress intensities. The largest decrease in FCG resistance was seen between 20Hz and 2Hz with the curves for 2Hz, 0.2Hz and 0.08Hz falling close together. While the FCG resistance and ΔK_c decreased as the frequency was lowered, ΔK_{th} increased.

The lowest ΔK_{th}, 18.0 MPa$\sqrt{m}$, was found at the highest frequency, 20Hz, and it increased to 24.1 MPa$\sqrt{m}$ at 0.08Hz. The largest decrease in ΔK_c was from 59.4 MPa$\sqrt{m}$ at 20Hz to 42.5 MPa$\sqrt{m}$ at 2Hz after which a less drastic drop to 35.8 MPa$\sqrt{m}$ at 0.08Hzwas noted. The curves for 2Hz, 0.2Hz and 0.08Hz underwent a cross-over when the stress intensity range reached $2x10^{-7}$ - $3x10^{-7}$ m/cycle.

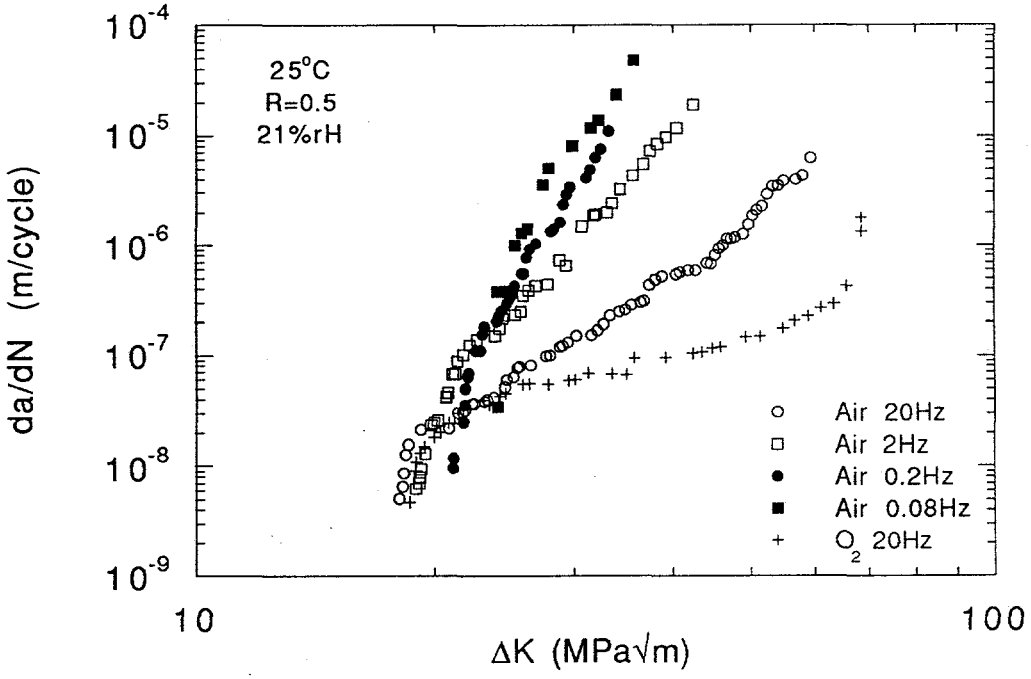

Fig. 4.27 Effect of frequency on 0.5%ZrC fatigued in 21%rH air at 25°C. R = 0.5.

4.4 Fractography of FCG Specimens

The crack propagation direction in all fracture surfaces shown in this section is horizontal from left to right.

Fig. 4.28 shows a typical crack path for the iron aluminides tested. The crack path was found to be transgranular with very little crack branching. In all tests reported the crack path displayed similar characteristics.

The fracture surface of the fatigued iron aluminides was found to be dependent on alloy composition. The fracture mode in the ternary alloy was mixed transgranular cleavage and intergranular failure in all environments. Fig. 4.29 shows the mixed mode surface of the ternary alloy in air where intergranular failure represented approximately 30% of the surface. The fracture surface in oxygen gas was shown in Fig. 4.30 and the amount of intergranular facets increased to roughly 50%. Fig. 4.31 and Fig. 4.32 show the fracture surface of the ternary alloy in hydrogen gas and vacuum, respectively. In both environments the amount of intergranular facets were 30%, similar to air. Note that the fracture surface of the ternary alloy was fairly independent of environment.

The fracture surface of 0.5%ZrC was found to be slightly sensitive to environment. Fig. 4.33 shows the mixed fibrous tearing and transgranular cleavage appearance in 21%rH air, where cleavage represented approximately 50% of the surface. An increase in humidity level had no major influence on the fracture surface. Fig. 4.34a and 4.34b show the mixed fibrous tearing and transgranular surface of 0.5%ZrC in 48%rH and 81%rH air, respectively.

In oxygen, the fracture surface was completely fibrous tearing, as seen in Fig. 4.35a. However, once the critical stress intensity was reached the fracture mode changed. The fracture mode shifted from complete fibrous tearing to mixed fibrous tearing and

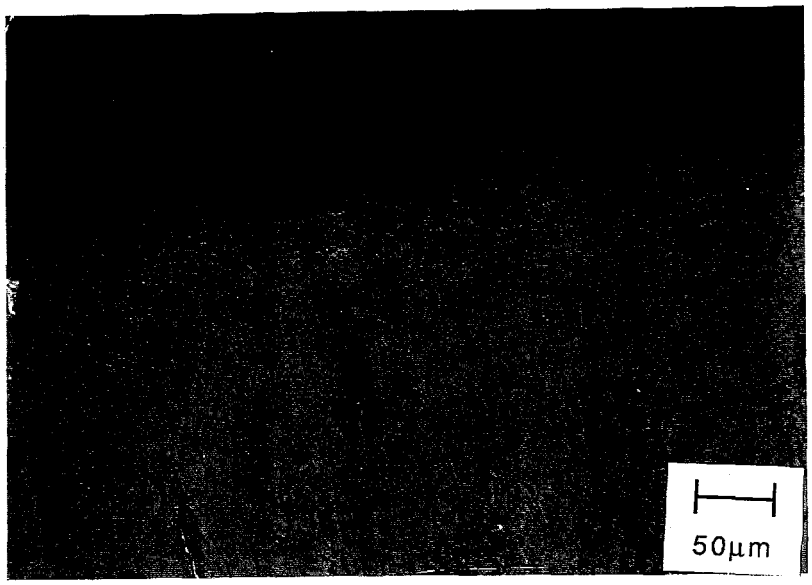

Fig. 4.28 Typical crack growth path in the iron aluminide FCG specimens.

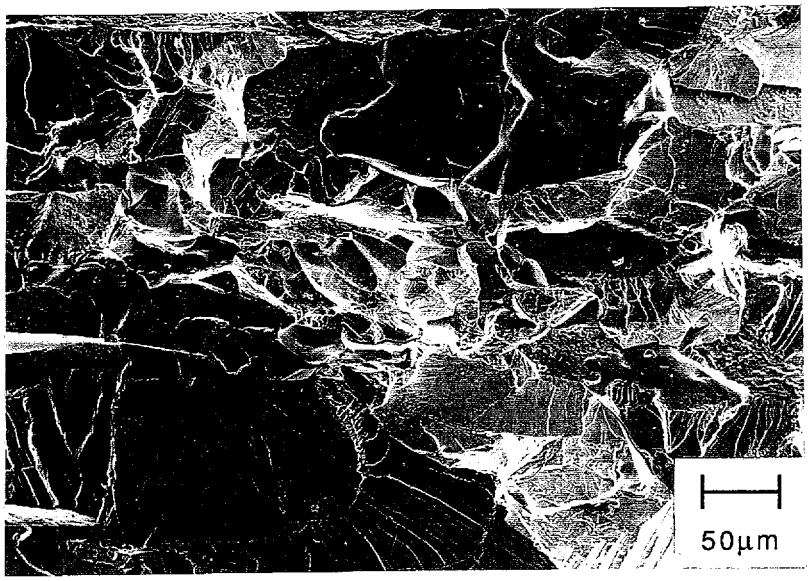

Fig. 4.29 Fracture surface of the ternary alloy fatigued in air at ΔK=18 MPa$\sqrt{m}$ showing cleavage and IG facets.

Fig. 4.30 Fracture surface of the ternary alloy fatigued in oxygen gas at ΔK=26 MPa$\sqrt{m}$ showing cleavage and IG facets.

Fig. 4.31 Fracture surface of the ternary alloy fatigued in hydrogen gas at ΔK=15 MPa$\sqrt{m}$ showing cleavage and IG facets.

Fig. 4.32 Fracture surface of the ternary alloy fatigued in vacuum at ΔK=30 MPa$\sqrt{m}$ showing cleavage and IG facets.

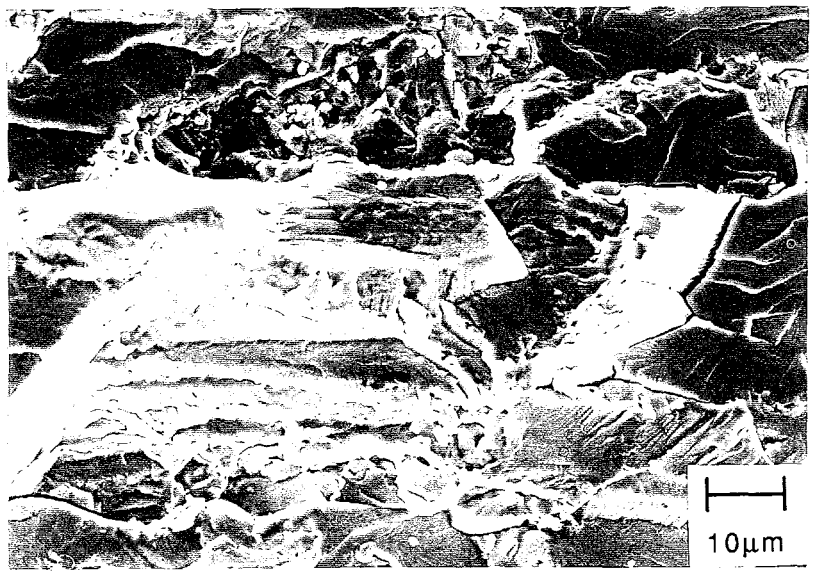

Fig. 4.33 Fracture surface of 0.5%ZrC fatigued in 21%rH air at ΔK=28 MPa$\sqrt{m}$ showing cleavage and fibrous tearing.

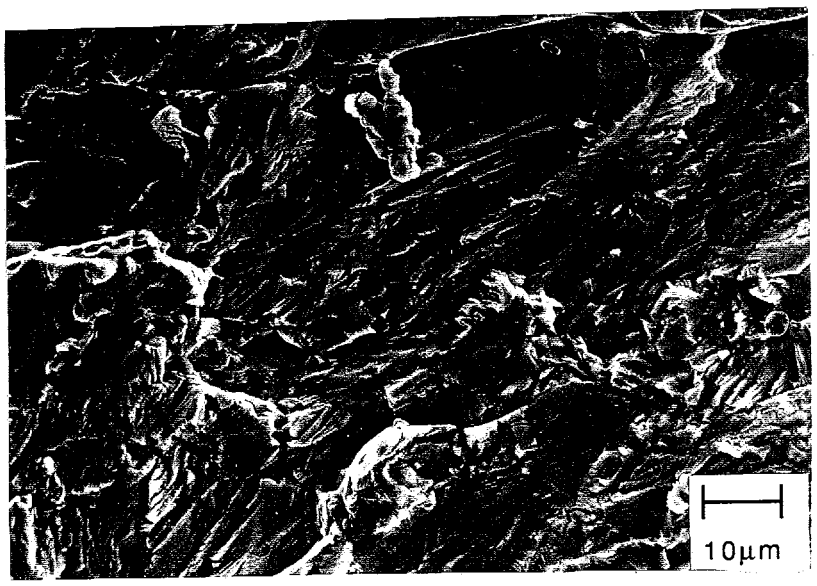

(a)

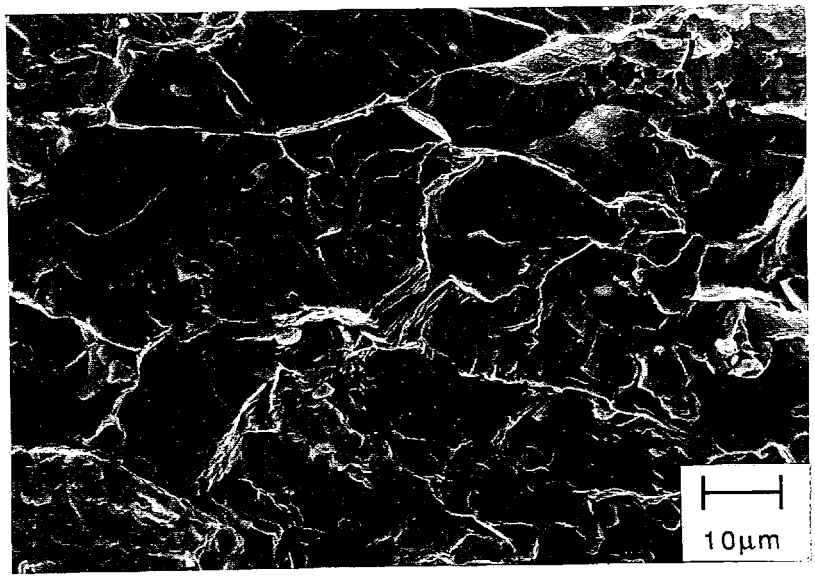

(b)

Fig. 4.34 Fracture surface of 0.5%ZrC fatigued (a) in 48%rH air at ΔK=27 MPa$\sqrt{m}$ and (b) 81%rH air at ΔK=24 MPa$\sqrt{m}$ showing cleavage and fibrous tearing.

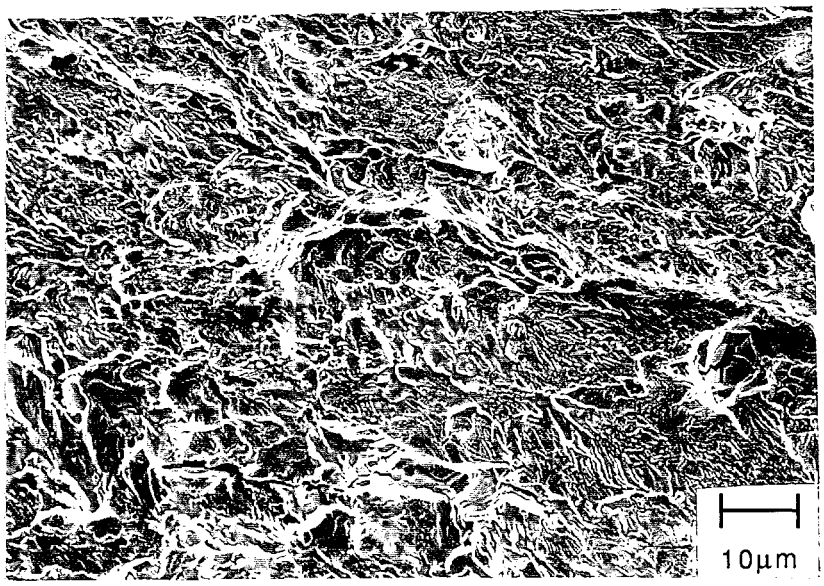

(a)

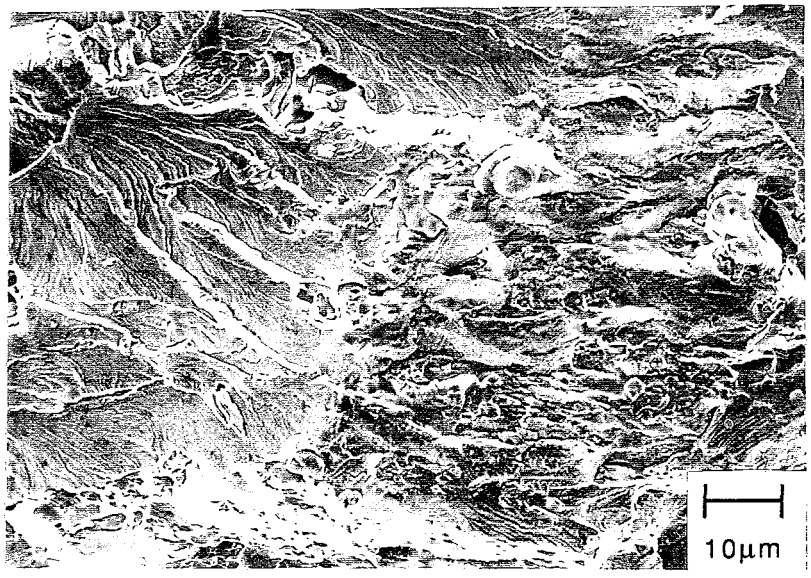

(b)

Fig. 4.35 Fracture surface of 0.5%ZrC fatigued (a) in oxygen gas at ΔK=35 MPa$\sqrt{m}$ showing fibrous tearing and (b) in the overload region at ΔK=60 MPa$\sqrt{m}$ showing fibrous tearing and cleavage.

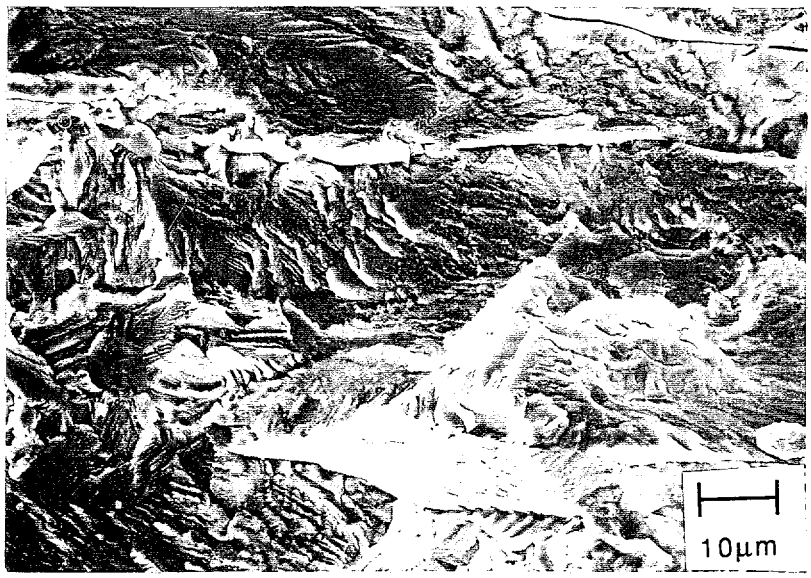

Fig. 4.36 Fracture surface of 0.5%ZrC fatigued in hydrogen gas at ΔK=21 MPa$\sqrt{m}$ showing cleavage and fibrous tearing.

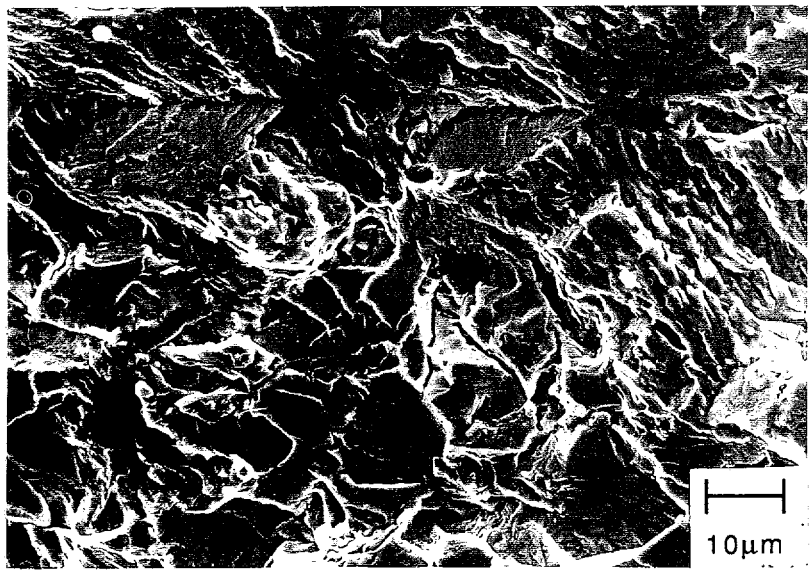

Fig. 4.37 Fracture surface of 0.5%ZrC fatigued in vacuum at ΔK=33 MPa$\sqrt{m}$ showing cleavage and fibrous tearing.

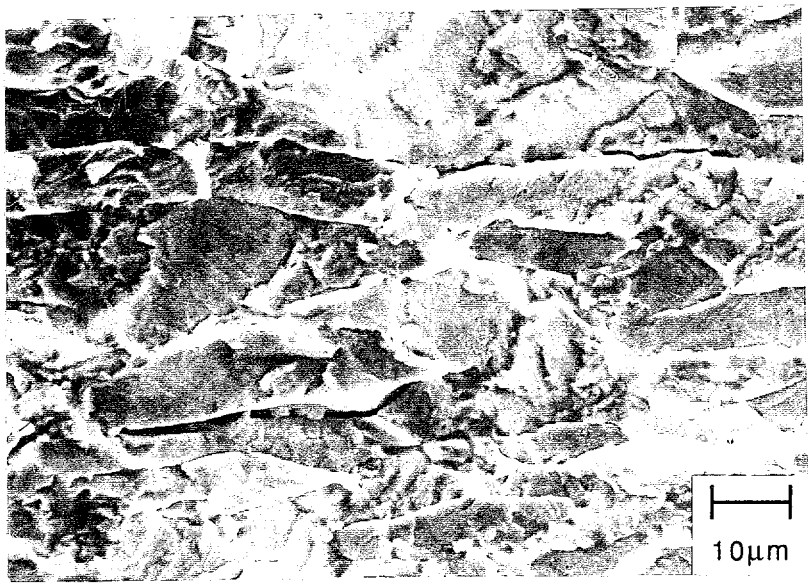

(a)

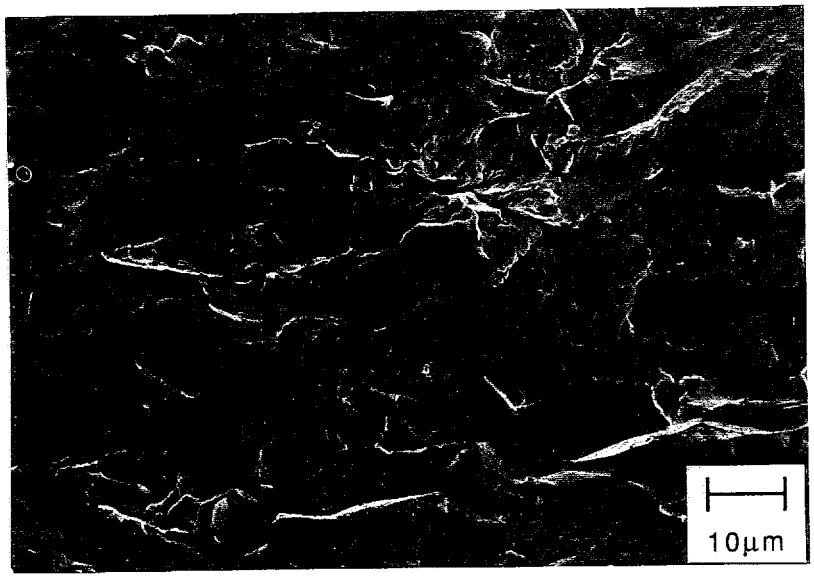

(b)

Fig. 4.38 (a) Fracture surface of 0.5%ZrC fatigued in 21%rH air at frequency=2.0Hz at ΔK=20 MPa$\sqrt{m}$ and (b) at frequency= 0.2Hz at ΔK=23 MPa$\sqrt{m}$.

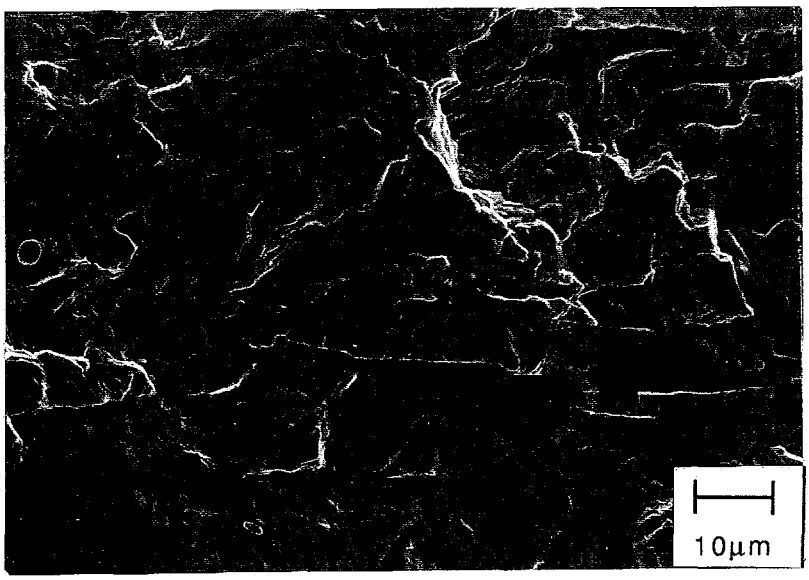

(c)

Fig. 4.38 continued — Fracture surface of 0.5%ZrC fatigued in 21%rH air (c) frequency=0.08Hz at ΔK=25 MPa$\sqrt{m}$.

transgranular cleavage where cleavage accounted for 50% of the surface. Fig. 4.35b shows the fracture surface of the overload region in 0.5%ZrC in oxygen. Fig. 4.36 shows the fracture surface in hydrogen. In hydrogen, the fracture surface was 70% fibrous tearing and 30% transgranular. The fracture surface in vacuum, Fig. 4.37, was also characterized by mixed fibrous tearing and transgranular cleavage, with roughly 50% being cleavage.

Decreasing the fatigue frequency of 0.5%ZrC in 21%rH air had no effect on the fracture surface. Figs. 4.38a-c show the fracture surface of the tests at 2.0, 0.2, and 0.08Hz, respectively. In all cases, the fracture appearance was mixed fibrous tearing and transgranular, similar to the 20Hz test.

In 0.5%ZrC, longitudinal cracking was observed in all environments at higher stress intensities. The crack plane of the compact tension specimens was the short-transverse plane, which is the plane perpendicular to the elongated direction of the grains. The longitudinal cracks ran along the longitudinal plane, which is parallel to the elongated direction of the grains.

0.5%Zr also showed some sensitivity to environment in the fracture mode. In 21%rH air, the fracture surface was mixed fibrous tearing and intergranular failure, as seen in Fig. 4.39. The fibrous tearing was predominant while a relatively small amount of intergranular facets were visible, approximately 20%. As the moisture content was increased, no corresponding change in the fracture surface was observed. Figs. 4.40a and 4.40b show the mixed fibrous tearing and intergranular failure surface of 0.5%Zr in 48% and 81%rH air, respectively.

In hydrogen, Fig. 4.41a, the fracture mode was again mixed. The mixed mode in hydrogen was transgranular cleavage and intergranular failure, as compared to the fibrous tearing and intergranular in air. The cleavage mechanism was predominant with 10% of

Fig. 4.39 Fracture surface of 0.5%Zr fatigued in 21%rH air at ΔK=28 MPa$\sqrt{m}$ showing IG facets and fibrous tearing.

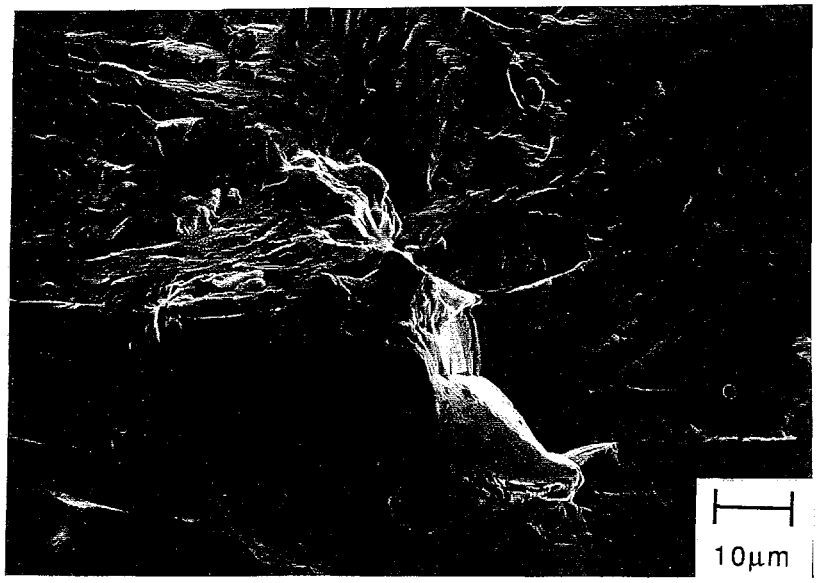

(a)

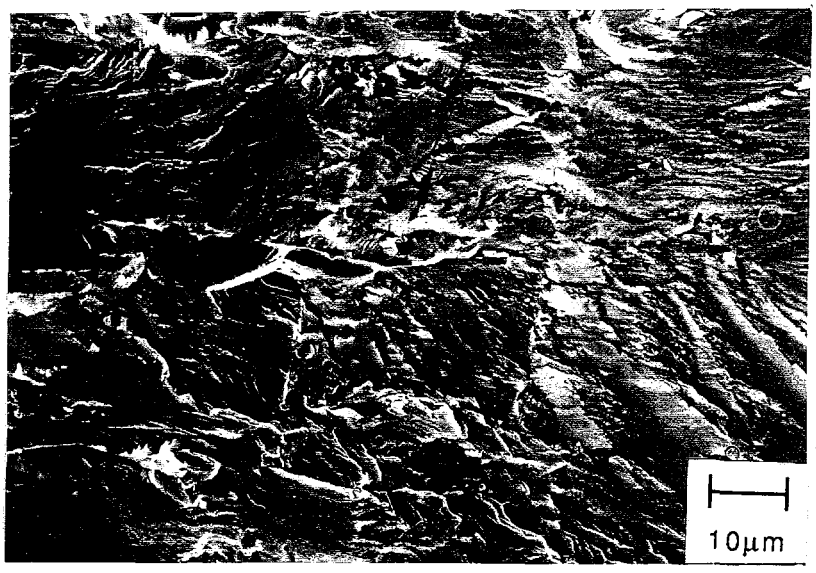

(b)

Fig. 4.40 Fracture surface of 0.5%Zr fatigued in (a) 48%rH air at ΔK=25 MPa$\sqrt{m}$ and (b) 81%rH air at ΔK=22 MPa$\sqrt{m}$ showing IG facets and fibrous tearing.

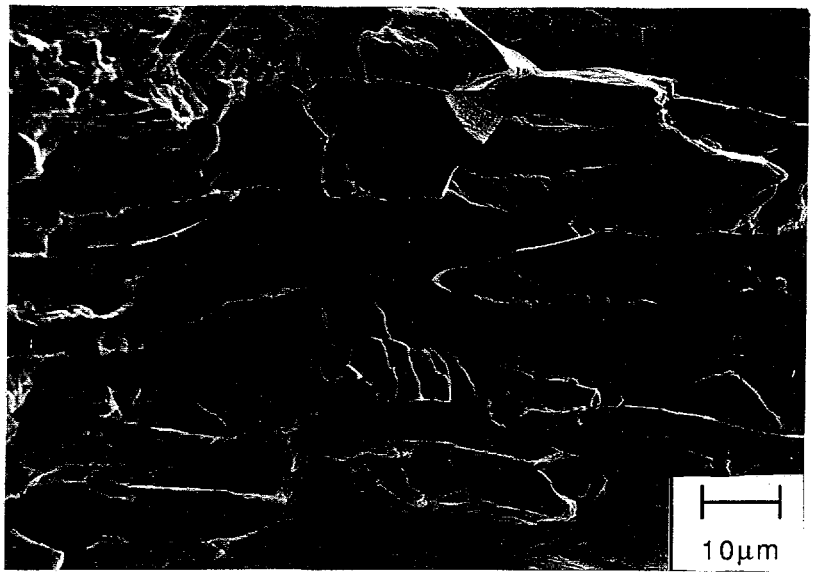

(a)

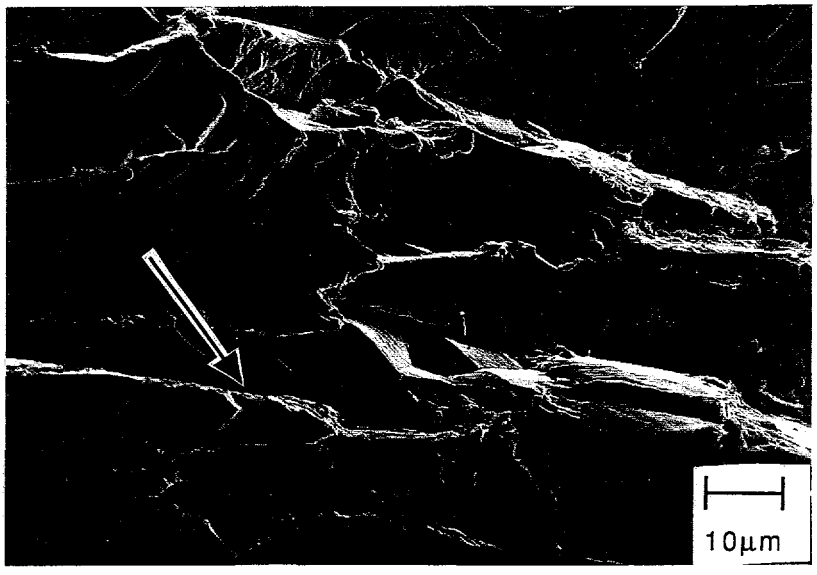

(b)

Fig. 4.41 Fracture surface of 0.5%Zr fatigued (a) in hydrogen gas at ΔK=22 MPa$\sqrt{m}$ showing cleavage and IG facets and (b) arrow showing longitudinal cracks at ΔK=26 MPa$\sqrt{m}$.

(a)

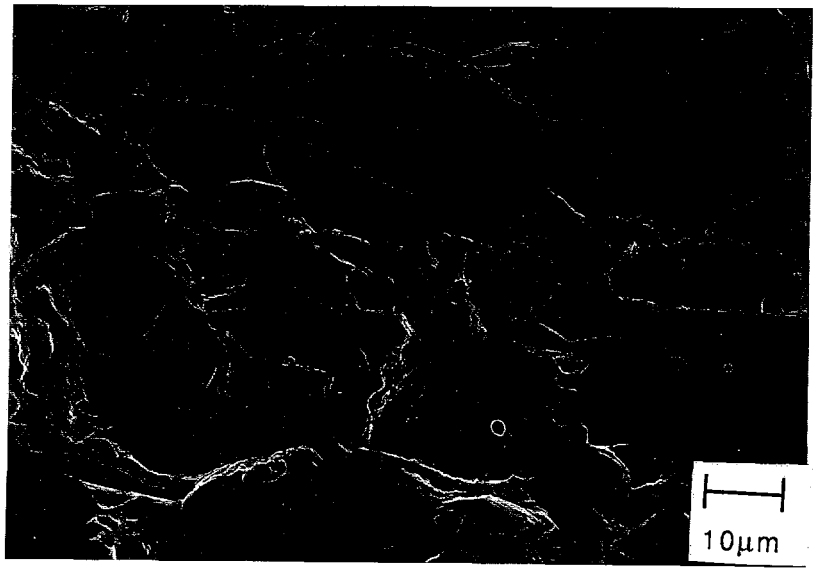

(b)

Fig. 4.42 Fracture surface of 0.5%Zr fatigued (a) in oxygen gas at ΔK=42 MPa$\sqrt{m}$ showing fibrous tearing and (b) in the overload region at ΔK=49 MPa$\sqrt{m}$ showing cleavage and fibrous tearing.

Fig. 4.43 Fracture surface of 0.5%Zr fatigued in vacuum at ΔK=34 MPa$\sqrt{m}$ showing IG facets and fibrous tearing.

the surface intergranular. 0.5%Zr also displayed some longitudinal cracking in hydrogen, as can be seen in Fig. 4.41b.

In oxygen, the fracture mode shifted to all fibrous tearing. Fig. 4.42a shows the fracture surface in oxygen gas. As seen in 0.5%ZrC, once the critical stress intensity was reached the fracture mode changed. The fracture mode shifted from complete fibrous tearing to mixed fibrous tearing and transgranular cleavage, where cleavage represents 50% of the surface. Fig. 4.42b shows the fracture surface of the overload region in 0.5%Zr in oxygen. Fig. 4.43 shows the fracture surface in vacuum. The fracture surface was similar to the overload region in oxygen with a mixture of fibrous tearing and transgranular cleavage. As in oxygen cleavage represents approximately 50% of the surface.

As in all the Zr-containing alloys, failure of 1%ZrC was found to be slightly sensitive to environment. Fig. 4.44 shows the fracture surface in 21%rH air. The fracture mode was seen to be mixed fibrous tearing and intergranular failure. The amount of intergranular failure was roughly 25% in 1%ZrC. The fracture mode was unchanged by an increase in humidity level. Fig. 4.45a shows the fracture surface in 48% rH air and Fig. 4.45b shows the fracture surface in 81%rH air.

In hydrogen, the failure mode was mixed transgranular cleavage and intergranular failure. Fig. 4.46 shows the fracture surface in hydrogen gas. The amount of intergranular failure in hydrogen was observed to be about 50%. Longitudinal cracks were also seen 1%ZrC in hydrogen.

The fracture mode shifted to one of fibrous tearing in oxygen, as can be seen in Fig. 4.47a. The fracture appearance was very similar in all Zr-containing alloys in oxygen. Fig. 4.47b shows the fracture surface in the overload region in oxygen. Similar to the other Zr-containing alloys, the fracture mode shifted but in the case of 1%ZrC it was mixed fibrous tearing, transgranular and intergranular failure. Fig. 4.48 shows the

fracture surface in vacuum. The fracture mode shifted back to a fibrous tearing with approximately 10% of intergranular failure.

A summary of the fracture appearance of the fatigue crack growth specimens is listed in Table 5.

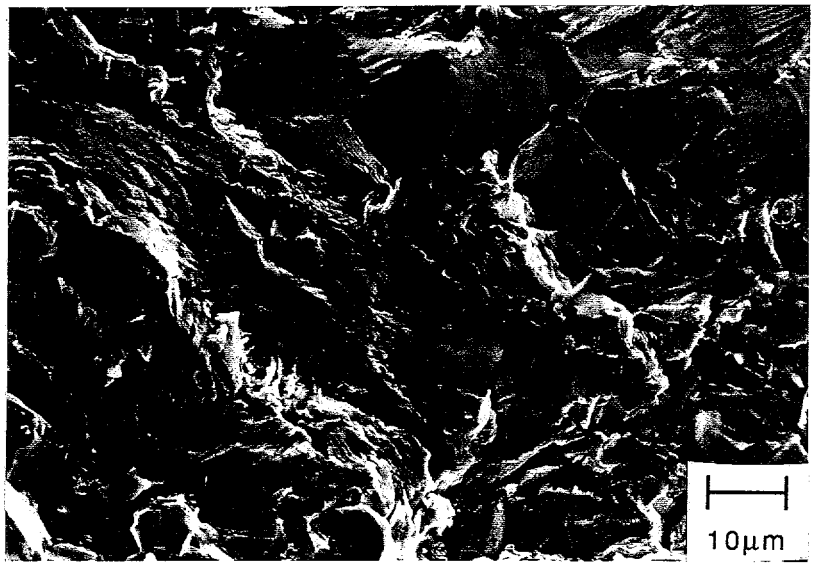

Fig. 4.44 Fracture surface of 1%ZrC fatigued in 21% rH air at ΔK=24 MPa$\sqrt{m}$ showing IG facets and fibrous tearing.

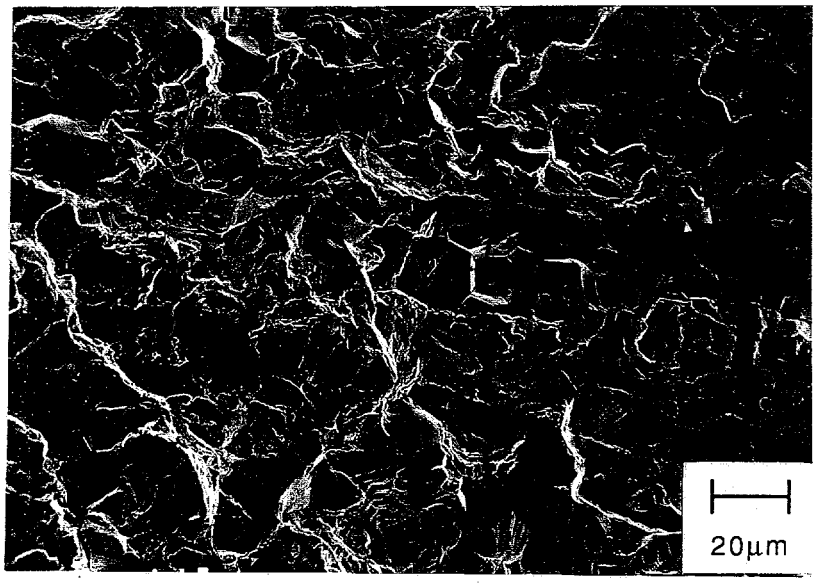

(a)

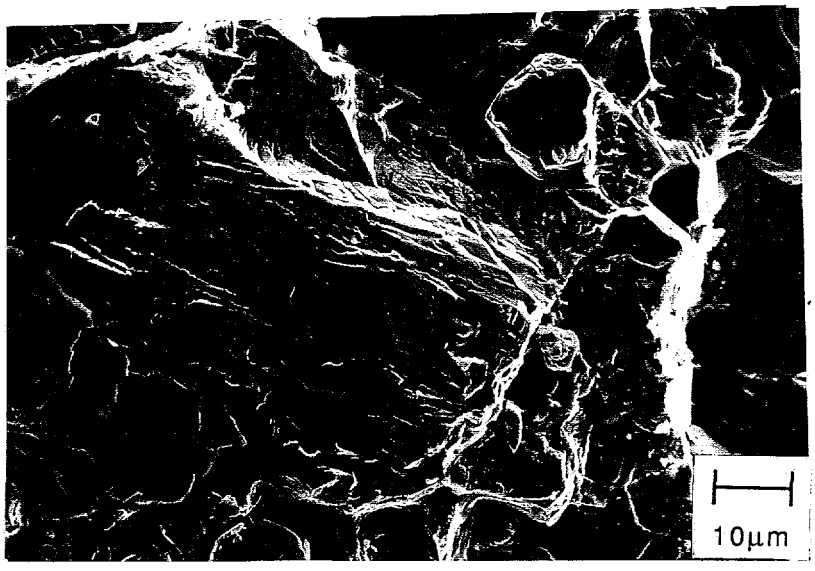

(b)

Fig. 4.45 Fracture surface of 1%ZrC fatigued (a) in 48%rH air at ΔK=26 MPa$\sqrt{m}$ and (b) in 81%rH air at ΔK=24 MPa$\sqrt{m}$ showing IG facets and fibrous tearing.

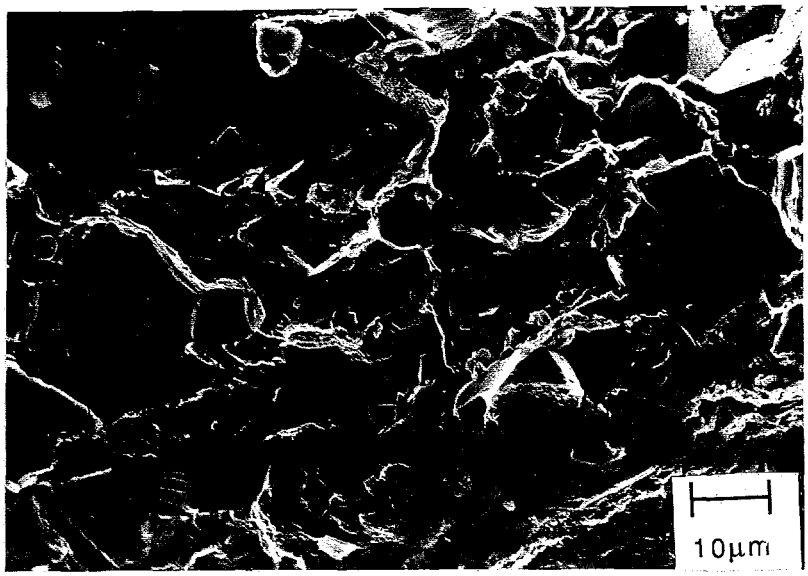

Fig. 4.46 Fracture surface of 1%ZrC fatigued in hydrogen gas at ΔK=21 MPa$\sqrt{m}$ showing cleavage and IG facets.

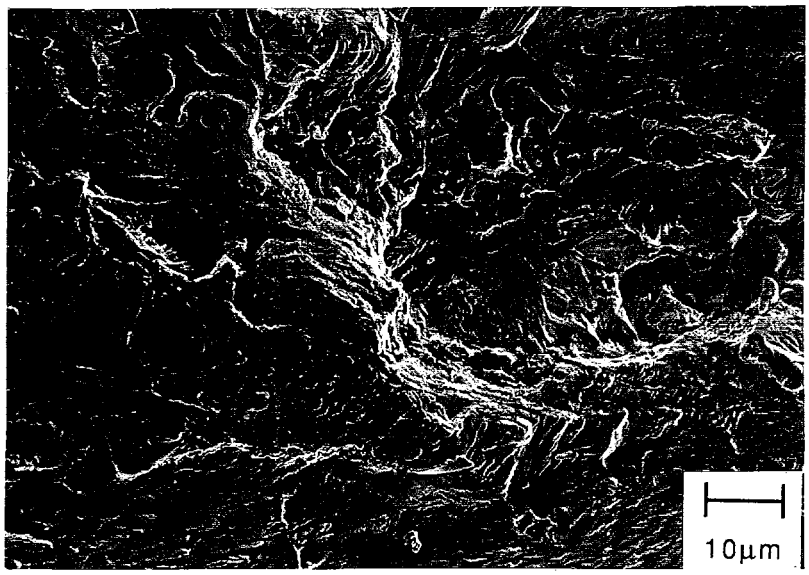

(a)

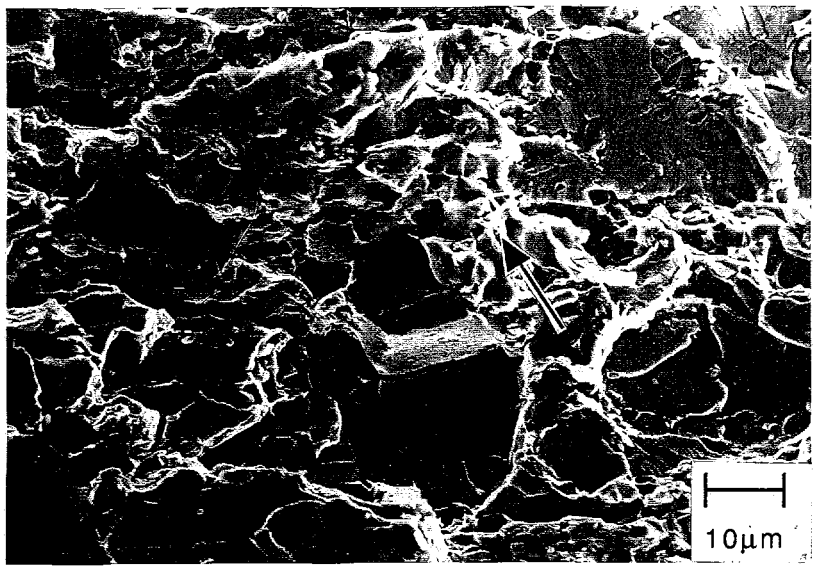

(b)

Fig. 4.47 Fracture surface of 1%ZrC fatigued in oxygen (a) at ΔK=35 MPa$\sqrt{m}$ showing fibrous tearing and (b) in the overload region at ΔK=36.5 MPa$\sqrt{m}$ showing cleavage, IG facets, and fibrous tearing; arrow indicates fibrous tearing.

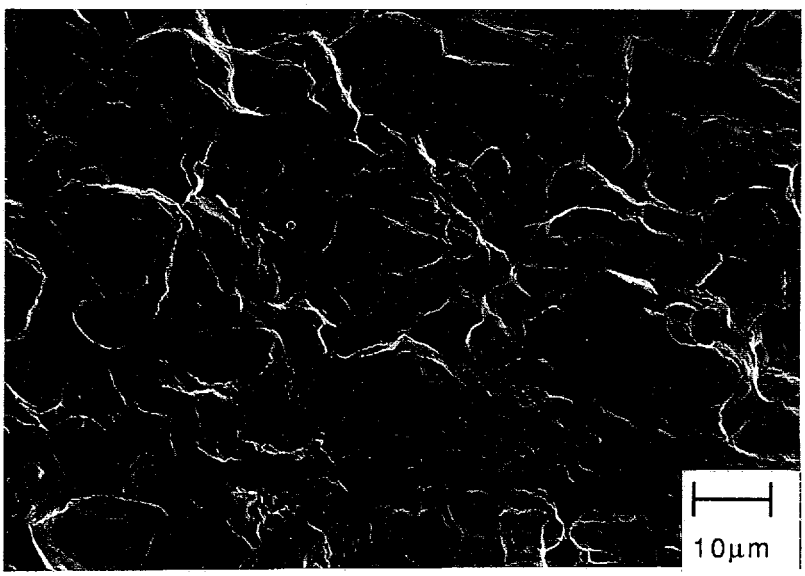

Fig. 4.48 Fracture surface of 1%ZrC fatigued in vacuum at ΔK=31 MPa$\sqrt{m}$ showing IG facets and fibrous tearing.

TABLE 5
Appearance of Fatigued Fracture Surface in Iron Aluminides

Alloy	Environment	Fracture Appearance
Ternary	Air (30% rH)	TG cleavage + 30% IG
Ternary	O_2	TG cleavage + 50% IG
Ternary	Vacuum	TG cleavage + 30% IG
Ternary	H_2	TG cleavage + 30% IG
0.5%Zr	Air (21% rH)	Fibrous tearing + 20% IG
0.5%Zr	Air (48% rH)	Fibrous tearing + 20% IG
0.5%Zr	Air (81% rH)	Fibrous tearing + 20% IG
0.5%Zr	O_2	Fibrous tearing
0.5%Zr	Vacuum	Fibrous tearing + 50% TG
0.5%Zr	H_2	TG + 10% IG
0.5%ZrC	Air (21% rH)	Fibrous tearing + 50% TG
0.5%ZrC	Air (48% rH)	Fibrous tearing + 50% TG
0.5%ZrC	Air (81% rH)	Fibrous tearing + 50% TG
0.5%ZrC	O_2	Fibrous tearing
0.5%ZrC	Vacuum	Fibrous tearing + 50% TG
0.5%ZrC	H_2	Fibrous tearing + 30% TG
1%ZrC	Air (21% rH)	Fibrous tearing + 25% IG
1%ZrC	Air (48% rH)	Fibrous tearing + 25% IG
1%ZrC	Air (81% rH)	Fibrous tearing + 25% IG
1%ZrC	O_2	Fibrous tearing
1%ZrC	Vacuum	Fibrous tearing + 10% IG
1%ZrC	H_2	TG + 50% IG

5 DISCUSSION

5.1 Plasticity Effects on Crack Growth

When measuring fracture toughness, the test specimen dimensions should be large enough that the material is in a state of plane strain. If this condition is not met, then plasticity effects may alter the measured toughness. ASTM fracture testing standards specify that to ensure that the specimen is in a predominantly plane strain condition, the thickness of the specimen, B, should be 50 times the plastic zone radius, R_y, expected for plane strain. If this condition is met, then plasticity effects are negligible. This condition can be expressed as:

$$R_y/B<0.02 \text{ to satisfy plane strain conditions} \qquad \text{Eq. 6}$$

If the plastic zone radius ahead of a fatigue crack under plane strain conditions is taken as stated by Irwin (91), then it can be expressed by:

$$R_y=\frac{1}{6\pi}\left(\frac{K_{max}}{\sigma'_{ys}}\right)^2 \qquad \text{Eq. 7}$$

where σ'_{ys} is the cyclic yield stress and can be approximated by twice the monotonic yield stress. The plasticity effects on crack growth can be determined by inserting Eq. 7 into Eq. 6 and determining if the conditions are satisfied.

The plastic zone size and the R_y/B ratio of the iron aluminide specimens fatigued in air and oxygen gas were calculated for three values of da/dN and are listed in Table 6.

TABLE 6
Plastic Zone Size Calculations

		da/dN=10^{-8} m/cycle			da/dN=10^{-7} m/cycle			da/dN=10^{-6} m/cycle		
Environment	σ'_{ys}	K_{max}	R_y	R_y/B	K_{max}	R_y	R_y/B	K_{max}	R_y	R_y/B
ternary										
Air	1000	34.4	62.7	0.015	40.2	85.7	0.019	47.0	117	0.027
O_2	1020	50.2	128	0.03	77.0	302	0.07	83.6	356	0.08
0.5%ZrC										
Air	1380	36.7	37.5	0.008	56.0	87.3	0.019	92.6	239	0.05
O_2	1360	38.0	41.4	0.009	84.6	205	0.04	136	531	0.1
0.5%Zr										
Air	1340	37.8	42.2	0.009	54.2	86.7	0.018	74.0	162	0.03
O_2	1340	41.0	49.6	0.01	86.6	221	0.05	-	-	-
1%ZrC										
Air	1020	32.7	54.5	0.014	44.8	102	0.025	-	-	-
O_2	1020	50.4	129	0.03	71.8	263	0.06	-	-	-

$\sigma'_{ys} = 2\sigma_{ys}$; in MPa

$R_y = \frac{1}{6\pi}\left(\frac{K_{max}}{\sigma'_{ys}}\right)^2$; in μm from (91)

K_{max} in MPa$\sqrt{m}$

None of the alloys tested completely met the plain strain condition for air or oxygen. In air, the condition was met, except at high crack growth rates, for all alloys. The plastic zone size and R_y/B ratio decreased significantly in air verses oxygen.

Due to the failure to meet ASTM criteria for plane strain, the crack growth rates measured in this study couldnot be quantitatively compared to those for other alloys. Since the ASTM criterion is conservative when predicting the onset of plane strain, the crack growth data can however, be compared among themselves without a large influence of plane strain.

5.2 Effect of Environment

Different environments often affect the fatigue crack growth behavior of a given material. An aggressive environment often decreases the threshold stress intensity and enhances crack nucleation during Stage I crack growth. In Stage II, it can influence crack growth rates and the Stage II slope, m, of the Paris equation (Eq. 5). In general, Stage III is often not affected by environmental changes. Stage III fatigue crack resistance more often is influenced by microstructure, mean stress, and specimen thickness.

However, the iron aluminides in this study displayed critical stress intensities that were slightly sensitive to environment. The critical stress intensities in all alloys tested were found to be lower in hydrogen, air, and even vacuum than in oxygen. The largest difference was found in the ternary alloy where ΔK_c decreased 53% when the environment was changed from oxygen to hydrogen.

This finding is similar to the results of several studies which have found environmental effects of critical stress intensities in iron aluminides and other ordered alloys. Castagna (63) found similar results in Fe-35Al and an Fe_3Al alloy where the critical stress intensity decreased in hydrogen gas and air as compared to oxygen. The

critical stress intensity of an ordered Fe-Ni-V alloy was found to increase almost 100% when the environment was changed from oxygen to hydrogen (55). A similar result was found by Pao et al (92) in ordered Ni_2Cr fatigued in air and aqueous NaCl. The critical stress intensity was found to decrease in NaCl as compared to air.

In all alloys the lowest fatigue crack growth rate was found in oxygen, with 0.5%ZrC having the highest resistance to crack growth of all. Both 0.5 at% Zr alloys had similar properties but 0.5%ZrC had a critical stress intensity that was 29% higher than 0.5%Zr. This is most likely due to the slightly smaller grain size of 0.5%ZrC which would result in a higher fracture toughness. It has been shown (37) that small additions of carbon act as grain refiners in iron aluminides. As can be seen in Figs. 4.1 and 4.2, the carbon addition did result in some grain refinement.

One interesting result of this work was the higher threshold values in vacuum. In all alloys the threshold stress intensity was found to be the highest in vacuum. This affect is most probably due to oxide-induced irreversibility of slip. In moisture and oxygen environments, when the stress cycle is reversed the formation of the Al_2O_3 layer hinders the reversal of slip. Thus a small freshly created surface at the crack tip is prevented from rejoining and the crack advances. This mechanism has been shown to explain the higher threshold values in vacuum when compared to air for a number of steel alloys (93, 94, 95).

But while the threshold stress intensity was higher in vacuum than in any other atmosphere, a cross-over of the curves in vacuum and oxygen occurred at crack growth rates between $7x10^{-8}$ to $4x10^{-8}$ m/cycle in all alloys studied. This is most likely a result of insufficient vacuum. It has been shown that a decrease in ductility results from as little as 1 Pa partial pressure of water vapor (47) and no influence was noted at a vacuum level of $1.3x10^{-4}$ Pa. In this study, the lowest vacuum attained was approximately $1x10^{-3}$ Pa. With a very low moisture content, the crack growth rate could be effected by the

hydrogen embrittlement mechanism attributed to iron aluminides while the threshold may not due to incomplete Al_2O_3 layer formation. Further indications that the vacuum level was insufficient was the similarity between the fracture path in air and vacuum for the Zr-containing alloys.

Another interesting result is that the Zr-containing alloys in this study exhibit an increase in the threshold stress intensity when fatigued in hydrogen as compared to oxygen. In 0.5%Zr, the threshold increased 9% when the environment was changed from oxygen to hydrogen, while in 0.5%ZrC and 1%ZrC ΔK_{th} increased 12% and 21%, respectively. It should be noted that the threshold stress intensity in hydrogen was similar in each Zr-containing alloy with a value of approximately 20 MPa$\sqrt{m}$. In section 5.4, it is shown that the rate limiting step in the hydrogen embrittlement during fatigue crack growth is dislocation-assisted diffusion. In preliminary transmission electron microscopy (TEM) studies of the Zr-containing alloys, Zr precipitates have been seen along the grain boundaries where dislocations pile up. Therefore, the precipitates could trap the hydrogen thereby lowering the hydrogen content on slip planes which could raise the threshold stress intensity.

5.3 Effect of Zirconium

The only compositional changes in this study were the addition of Zr and carbon to the base Fe-28Al-5Cr alloy. All specimens were tested in the same ordered condition, B2, so there would be no influence associated with different ordered structure. Therefore, all variations in the fatigue crack growth behavior of these alloys should be considered with respect to those alloying additions.

Fractographic evidence indicates two mechanisms by which the zirconium additions affect the crack growth rates in the Fe_3Al, Cr alloys. First, all the Zr-containing

alloys exhibited a fibrous tearing transgranular surface when fatigued in oxygen. This is typical of ductile materials. Only the ternary alloy exhibited a characteristically brittle fracture surface in oxygen, which consisted of mixed transgranular and intergranular failure. The indications from the shift in fracture mode of the Zr-containing alloys when compared to the ternary alloy is that the addition of zirconium strengthens the grain boundaries. Previous research (32) has shown that the addition of B and Zr shifted the fracture path of several iron aluminides from intergranular to transgranular, but it was believed that the boron addition had caused the grain boundary strengthening. In this study, the addition of 0.5 at.% Zr resulted in a shift of fracture mode which indicates that zirconium also strengthens grain boundaries in Fe_3Al.

Second was the observation of some intergranular failure in 0.5%Zr and 1%ZrC in hydrogen containing environments. These results are interesting as most studies on iron aluminides have shown no effect on the fracture path in alloys of less than 35% Al. The results of section 5.4 show that a dislocation-transport mechanism in iron aluminides is responsible for embrittlement. Such a mechanism would allow for increased hydrogen contents at the grain boundaries where the dislocations pile-up. Trapping of the hydrogen by precipitates along the grain boundaries could lead to premature failure, when compared to the bulk, due to localized embrittlement. The appearance of the intergranular facets in 0.5%Zr and 1%ZrC in hydrogen bearing environments, as compared fibrous tearing fracture in an inert environment, indicates that excess hydrogen is being delivered, or trapped, at the grain boundaries.

An increase in the amount of intergranular facets with increased Zr content was noticed. This may also be indicative of hydrogen trapping by the zirconium-containing precipitates. Several studies (96, 97) have noted that increased precipitation of high binding energy and high saturability traps, with respect to hydrogen, decreases the resistance to hydrogen embrittlement.

A third explanation for the increased resistance to embrittlement might lie in affects of zirconium on the oxidation behavior of these alloys. In oxidation studies (98, 99, 100) it has been shown that additions of a small amount of reactive elements, such as Zr, improves the oxidation resistance of the alloys. The amount of reactive elements needed have been shown to be between 0.1 and 0.2 at% and deterioration of scale adhesion was noted with additions of over 1 at%. While it has not been shown that this same effect is operable at room temperature, it is possible that zirconium could influence the Al_2O_3 layer which , in turn, could influence the hydrogen-metal reactions.

5.4 Frequency Effects

Previous research on the fatigue crack growth of iron aluminides has shown that dislocation-assisted diffusion is the rate limiting process in the hydrogen embrittlement during fatigue crack growth of iron aluminides (63). This phenomenon has been observed in a number of materials and is responsible for increased penetration depths of hydrogen over that of diffusion (68, 101, 102, 103). In this section, the model proposed by Castagna (63) will be applied to 0.5%ZrC.

In dislocation-assisted diffusion, an atmosphere of hydrogen develops about a dislocation generated near the crack tip. As the dislocation travels away from the tip, the hydrogen is dragged with it through the lattice. The penetration depth of hydrogen ahead of the crack tip is equal to the dislocation velocity times the time available per cycle, that is V/2f where V is the dislocation velocity and f the test frequency. In the model proposed by Tien and Richards (68), the predicted maximum dislocation velocity that can be achieved before the hydrogen atmosphere is stripped away from the dislocation is used to determine the maximum penetration depth for dislocation assisted transport. Tien and Richards expressed this maximum penetration, r_{max}, as:

$$r_{max} = V_{max}t = \frac{D}{kT}\frac{E}{30b}\frac{1}{2f} \qquad \text{Eq. 8}$$

where E is the binding energy of hydrogen to the dislocation, and is approximately 0.3eV, k is the Boltzman constant, D is the diffusion coefficient, and b is the burgers vector (taken as 3 Å). Table 7 lists the maximum penetration depth due to dislocation transport calculated from Eq. 8 for 0.5%ZrC for frequencies from 20 to 0.08 Hz. The diffusion coefficient used was $4x10^{-12}$ cm^2/sec as reported by Kasul and Heldt (48).

Castagna (63) showed that the corrosion-fatigue interaction term in Eq. 3 contains a stress intensity and frequency dependence which is:

$$\left(\frac{da}{dN}\right) = A\,\Delta K^m r^n \qquad \text{Eq. 9}$$

In Eq. 9, r is the penetration depth of hydrogen ahead of the crack tip, and A is a constant. Eq. 9 indicates that there is no embrittlement if either the applied stress intensity is zero or the internal hydrogen concentration is zero and the frequency effect is reflected in the penetration depth term as the depth will increase over one cycle as the frequency decreases. If it is assumed that the mechanical component of Eq.3 is independent of frequency and that the stress corrosion component is zero, the total crack growth rate in an embrittling environment, (da/dN), can then be expressed as a superposition of the response in the inert environment, $(da/dN)_i$, and the corrosion fatigue term as:

$$\left(\frac{da}{dN}\right) = \left(\frac{da}{dN}\right)_i + \left(\frac{da}{dN}\right)_{cf} \qquad \text{Eq. 10}$$

In order to verify the validity of Eq. 9, it can be rearranged as:

$$\text{Log}\left(\frac{da}{dN}\right)_{cf} = \text{Log(A)} + m\text{Log}(\Delta K) + n\text{Log(r)} \qquad \text{Eq. 11}$$

and a plot of $\text{Log}(da/dN)_{cf}$ vs. $\text{Log}(r_{max})$ at constant ΔK should yield a straight line with a slope of n and an intercept of $\text{Log(A)} + m\text{Log}(\Delta K)$. In order to create this plot, the

TABLE 7
Penetration Depth of Hydrogen Due to Dislocation Transport in 0.5%ZrC

Frequency (Hz)	r_{max} (m)
20	1.29×10^{-8}
2	1.29×10^{-7}
0.2	1.29×10^{-6}
0.08	3.24×10^{-6}

corrosion-fatigue term must be determined from Eq. 10. This is done assuming that (da/dN) can be taken as the response in the inert oxygen environment. The crack growth data for 0.5%ZrC in air have been broken down into the purely mechanical component and the corrosion-fatigue component, $(da/dN)_{cf}$ at the frequencies of 20 to 0.08 Hz and are shown in Table 8. The plots of Eq. 11 are shown in Fig. 5.1 for ΔK = 27, 29, and 31 MPa$\sqrt{m}$.

As can be seen in Fig. 5.1, the correlation is excellent, and from the least squares fit the exponent n in Eq. 9 is 0.74. To find the values of A and m in Eq. 9, the latter is rearranged into:

$$\text{Log}\left[\frac{\left(\frac{da}{dN}\right)_{cf}}{r_{max}^{0.74}}\right] = \text{Log(A)} + m\text{Log}(\Delta K) \qquad \text{Eq. 12}$$

TABLE 8
Effect of Frequency on $(da/dN)_{mech}$ and $(da/dN)_{cf}$ in 0.5%ZrC

	20Hz	2Hz	0.2Hz	0.08Hz
		$\Delta K = 27$ MPa$\sqrt{m}$		
$(da/dN)_{mech}$	9.8×10^{-8}	3.0×10^{-7}	1.25×10^{-6}	3.05×10^{-6}
$(da/dN)_{cf}$	5.0×10^{-8}	2.5×10^{-7}	1.2×10^{-6}	3.0×10^{-6}
		$\Delta K = 29$ MPa$\sqrt{m}$		
$(da/dN)_{mech}$	1.5×10^{-7}	5.6×10^{-7}	2.9×10^{-6}	6.6×10^{-6}
$(da/dN)_{cf}$	1.0×10^{-7}	5.0×10^{-7}	2.8×10^{-6}	6.5×10^{-6}
		$\Delta K = 31$ MPa$\sqrt{m}$		
$(da/dN)_{mech}$	3.1×10^{-7}	1.3×10^{-6}	5.9×10^{-6}	1.51×10^{-5}
$(da/dN)_{cf}$	2.5×10^{-7}	1.25×10^{-6}	5.8×10^{-6}	1.5×10^{-5}

da/dN in m/cycle

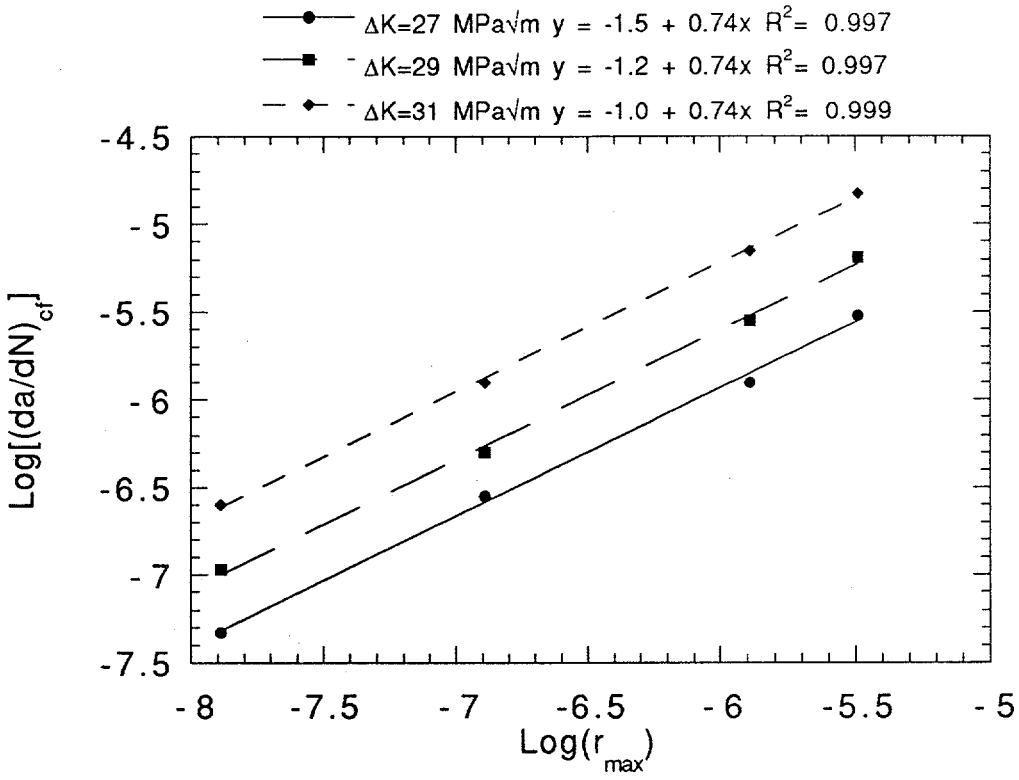

Fig. 5.1 Log-log plot of $(da/dN)_{cf}$ vs. maximum hydrogen penetration depth due to dislocation transport in 0.5%ZrC fatigued in 21%rH air.

Plotting Eq. 12 for all values of ΔK and frequencies (Fig. 5.2) yields a single frequency-modified curve and from a least squares fit the values of A and m are 4.9×10^{-19} and 11.7, respectively, and again the correlation is excellent.

As a final check, a plot of $(da/dN)_{cf}$ vs. $(r_{max})^{0.74}$ should result in a straight line for each applied stress intensity. Fig. 5.3 shows the result of this plot. Once again the correlation is excellent and shows that in fatigued 0.5%ZrC hydrogen moves into the lattice ahead of the crack tip by a dislocation-assisted transport mechanism.

It should be noted that even though the degree of embrittlement increased dramatically with decreased frequency the exponent, n, was unchanged. This indicates that the embrittlement does little to change the mobility, ease of generation , or hydrogen carrying capacity of the dislocations in 0.5%ZrC. Due to this any hydrogen-metal interaction which involves a change in dislocation mobility, such as hydrogen enhanced plasticity or inhibited dislocation motion in the presence of hydrogen, can be ruled out.

To gain a better understanding of the physical meanings of the values obtained with this model, a comparison should be made between the exponents and constants obtained for 0.5%ZrC with the ones found by Castagna (63) in his study on a similar Fe_3Al alloy, FA-129. The physical meaning of the exponent, n, in Eq. 9 has been described as either related to the quantity of hydrogen dislocations can carry into the plastic zone and the concentration of hydrogen required to enhance crack growth, or related to the distribution of penetration depths of the hydrogen-bearing dislocations (63). Table 9 lists the values found for the two alloys. 0.5%ZrC is found to have higher exponents and a lower constant. As shown in section 5.5, 0.5%ZrC also has a higher fatigue crack growth resistance than does FA-129.

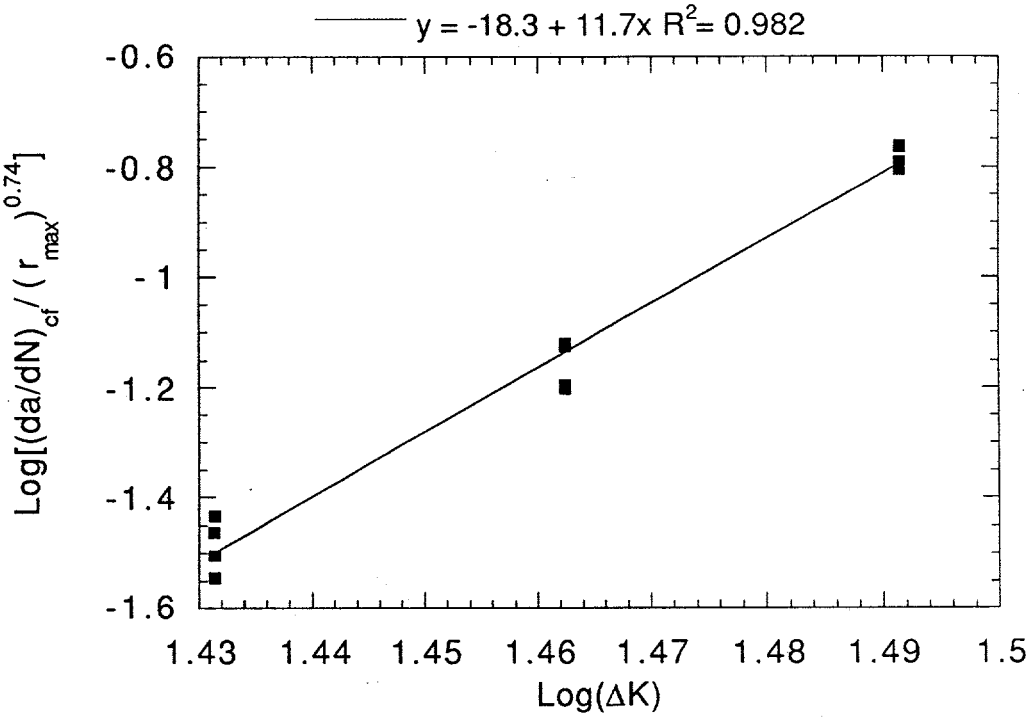

Fig. 5.2 Log-log plot of ratio of $(da/dN)_{cf}$ to hydrogen penetration depth vs. applied stress intensity in 0.5%ZrC fatigued in 21%rH air.

TABLE 9
Comparison of Values for 0.5%ZrC and FA-129

Values	0.5%ZrC	FA-129
n	0.74	0.52
m	11.7	10.3
A	4.9×10^{-19}	3.8×10^{-18}

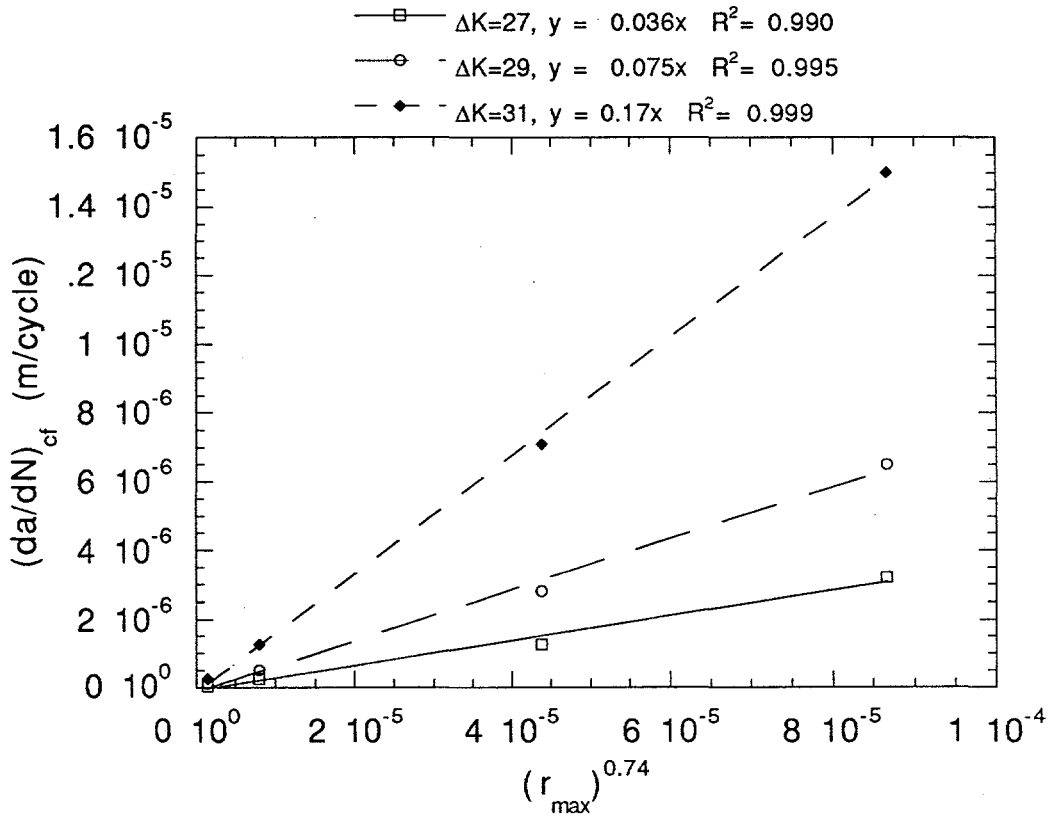

Fig. 5.3 $(da/dN)_{cf}$ vs. hydrogen depth raised to the 0.74 power in 0.5%ZrC fatigued in 21%rH air.

Based on the comparison between the work of Castagna and the work reported in this study, the physical meaning of the exponent, n, is probably related to the distribution of penetration depths of the hydrogen-bearing dislocations. It appears that the exponent relates the maximum theoretical penetration depth to the average actual penetration depth. The difference in penetration depths arises from the fact that before the hydrogen-bearing dislocation can reach a depth of r_{max} the hydrogen atoms can be stripped away at a trap, or the dislocation may be pinned. The exponent, and the crack growth resistance, for 0.5%ZrC was found to be greater than FA-129 which can be justified if the actual penetration depth of the hydrogen-bearing dislocations in 0.5%ZrC is lower than that of FA-129. The fractography and the TEM analysis indicate that the addition of zirconium results in precipitates which tend to form along the grain boundaries and appear to act as traps. These observations support the possibility for lower actual penetration depth of hydrogen-bearing dislocations in zirconium-containing alloys. No such evidence was found in FA-129.

The transport of hydrogen ahead of the crack tip by dislocation motion depends on the assumption that crack growth is continuous and does not occur in a step-wise mode. No indications of discontinuous crack growth were observed in this study, so the assumption of continuous crack growth is justified. As will be mentioned in the future work section of chapter 6, continuous crack growth should be confirmed for the alloys examined in this study.

5.5 Comparison to FCG Resistance in Other Alloys

The iron aluminide alloys in this study all displayed high threshold stress intensities or good resistance to initiation of fatigue cracks. However, the crack growth rates quickly increased and the slopes of the da/dN vs. ΔK curves were generally higher

than those of other structural iron-based alloys. Normalized fatigue crack growth curves for a couple of other Fe_3Al alloys along with a couple of typical iron alloys are plotted together with the data from this study in Fig. 5.4. With the exception of the ferritic steel, the R ratios and frequency are the same as those used in this study (R = 0.5, frequency = 20Hz).

The normalized threshold stress intensity measured in the ternary alloy is similar to B2 ordered FA-129 and much higher than that of FAP-Y, low alloy ferritic steel, and 9 1/4Cr-1Mo, while the normalized threshold stress intensity of 0.5%ZrC falls between FA-129, the ternary alloy and FAP-Y. At higher stress intensities, the ternary alloys performance dropped with only FAP-Y performing worse. While the curve for 0.5%ZrC had a lower normalized threshold stress intensity than the ternary alloy the curves crossed-over at a da/dN value of $1x10^{-7}$, with 0.5%ZrC having a lower crack growth rate. 0.5%ZrC also performed better than the other Fe_3Al alloys and displayed behavior similar to the ferritic steel.

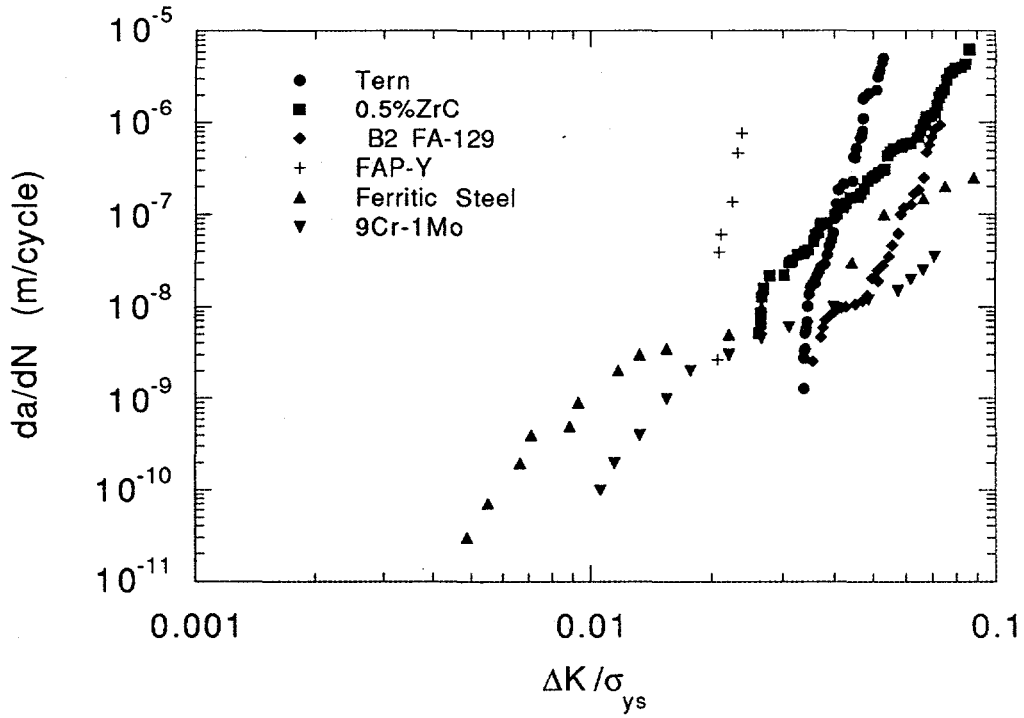

FA-129: Composition = 15.8%Al, 5.45%Cr, 0.96%Nb, 0.05%C balance Fe
(63) R=0.5 freq.=20Hz env.=25°C air GS=PR

FAP-Y: Composition = 8.5%Al, 5.5%Cr, 2.0%Mo, 0.2%Zr, 0.03%C,
(63) 0.1%Y balance Fe
R=0.5 freq.=20Hz env.=25°C air GS=42μm

Ferritic steel: Composition = 0.9%C, 0.38%Si, 1.46%Mn, 0.02%Cr, 0.25%Ni, 0.03%V,
(104) 0.025%Nb, balance Fe
R=0.5 freq.=50Hz env.=25°C air GS=*

9 Cr-1Mo: Composition = 0.12%C, 8.9%Cr, 1.09%Mo, 0.7%Si, 0.49%Mn, 0.17%Ni,
(105) 0.14%Cu, balance Fe
R=0.5 freq.=20Hz env.=25°C air GS=25μm

composition given in weight percent PR indicates partially recrystallized
* indicates not given in reference

Fig. 5.4 Comparison of fatigue crack growth in the ternary and 0.5%ZrC with other Fe_3Al and iron-based structural alloys.

6 CONCLUSIONS

The major conclusions of this work are:

1. The susceptibility to moisture-induced hydrogen embrittlement in Fe_3Al,Cr alloys is reduced by the addition of zirconium. This reduction in embrittlement is evidenced by the increased ductility and lowered crack growth rates displayed by 0.5%ZrC.

2. The beneficial effects of zirconium on the ductility and fatigue crack growth resistance of Fe_3Al,Cr alloys are limited to below 1 at.%. Zr. Evidence of this is seen by increased tensile ductility in air in the 0.5 at.% Zr alloys as compared to the 1 at.% Zr alloy, as well as, increased fatigue crack growth resistance in the 0.5 at.% alloys over that exhibited by the 1 at.% Zr alloy.

3. No critical level of humidity was found above which fatigue crack growth resistance was not influenced. But, fatigue crack growth resistance was seen to decrease with increased moisture content.

4. The possible mechanisms for increased resistance to moisture-induced hydrogen embrittlement due to the addition of zirconium are; a) increased grain boundary strength, b) trapping of hydrogen by zirconium rich precipitates, and c) effects on the oxidation behavior.

5. The zirconium to carbon ratio greatly influences the ductility, as proposed by Sikka (106), and fatigue crack growth behavior in iron aluminides. This was seen in increased tensile ductility in the 0.5%Zr-0.05%C alloy as compared to the 1%Zr-0.05%C alloy, and lowered fatigue crack growth rates in the 0.5%Zr-0.05%C alloy while the 1%Zr-0.05%C alloy exhibited behavior similar to the base alloy.

6. Dislocation-assisted transport is responsible for the motion of hydrogen atoms through the lattice of 0.5%ZrC, and this process is the rate limiting step in the hydrogen embrittlement that occurs during fatigue crack growth.

7. 0.5%ZrC exhibits the highest fatigue crack growth resistance in both inert and embrittling environments compared to the ternary alloy, 0.5%Zr, 1%ZrC and to all other Fe_3Al alloys previously tested in the laboratory.

Suggested Future Work

- Determine the optimum zirconium level and zirconium to carbon ratio for high ductility and crack growth resistance.
- Determination of the exact mechanisms by which zirconium increases the susceptibility to embrittlement in Fe_3Al, Cr alloys.
- Examine the effect of long range order on the FCG resistance of Zr-containing alloys.
- Confirm that crack growth occurs continuously.

7 REFERENCES

1. J. H. DeVan, in Oxidation of High-Temperature Intermetallics(TMS, Warrendale, PA, 1989) pp. 107-115.

2. N. Ziegler, AIME Trans., vol. 100, pp. 267 (1932).

3. W. R. Kerr, Met. Trans. A, vol. 17A, pp. 2298-2300 (1986).

4. C. T. Liu, E. H. Lee and C. G. McKamey, Scr. Metall., vol. 23, pp. 875-880 (1989).

5. C. T. Liu, C. G. McKamey and E. H. Lee, Scr. Metall., vol. 24, pp. 385-390 (1990).

6. C. G. McKamey, J. A. Horton and C. T. Liu, J. Mater. Res., vol. 4, pp. 1156-1163 (1989).

7. V. K. Sikka, SAMPE qrt., vol. 22, pp. 2-10 (1991).

8. R. G. Bordeau, Air Force Wright Aeronautical Laboratories, Development of Iron Aluminides, AFWAL-TR-87-4009 (1987).

9. G. Culbertson and C. S. Kortovich, Air Force Wright Aeronautical Laboratories, Development of Iron Aluminides, AFWAL-TR-85-4155 (1986).

10. C. T. Sims, N. S. Stoloff and W. C. Hagel, Superalloys II. (John Wiley & Sons, Inc., New York, 1987).

11. B. D. Cullity, Elements of X-ray Diffraction. (Addison-Wesley, Reading, MA, 1978).

12. M. J. Marcinkowski and N. Brown, Acta Met., vol. 9, pp. 764-786 (1961).

13. R. C. Crawford and I. L. F. Ray, Phil. Mag., vol. 35, pp. 549-565 (1977).

14. Y. Hayashi, N. Iwai and N. Ohtani, Z. Physik, Chemie Neue Folge, vol. 114, pp. 213-220 (1979).

15. M. G. Mendiratta, S. K. Ehlers, D. K. Chatterjee and H. A. Lipsitt, Met. Trans. A, vol. 18A, pp. 283-291 (1987).

16. T. B. Massalski, Binary Alloy Phase Diagrams. (ASM, Metals Park, OH, 1986).

17. H. Inouye, in High Temperature Ordered Intermetallic Alloys C. C. Koch, C. T. Liu, N. S. Stoloff, Eds. (MRS, Pittsburgh, PA, 1985), vol. 39, pp. 255-261.

18. C. G. McKamey, J. A. Horton and C. T. Liu, in High Temperature Ordered Intermetallic Alloys II N. S. Stoloff, C. C. Koch, C. T. Liu, O. Izumi, Eds. (MRS, Pittsburgh PA, 1987), vol. 81, pp. 321-327.

19. M. Shea, A. Castagna and N. S. Stoloff, in High-Temperature Ordered Intermetallic Alloys IV L. A. Johnson, D. P. Pope, J. O. Stiegler, Eds. (MRS Symp. Proc., Pittsburgh, Pa, 1990), vol. 213, pp. 609-616.

20. C. G. McKamey and C. T. Liu, Scr. Metall., vol. 24, pp. 2119-2122 (1990).

21. D. B. Kasul and L. A. Heldt, Environmetnal Effects on the Mechanical Properties of an Fe-24.6Al Alloy, (TMS/ASM, 1990),

22. M. G. Mendiratta, S. K. Ehlers, D. M. Dimiduk, W. R. Kerr, S. Mazdiyasni and H. A. Lipsitt, in High Temperature Ordered Intermetallic Alloys II N. S. Stoloff, C. C. Koch, C. T. Liu, O. Izumi, Eds. (MRS, Pittsburgh PA, 1987), vol. 81, pp. 393-404.

23. C. G. McKamey, P. J. Maziasz and J. W. Jones, J. Mater. Res., vol. 7, pp. 2089-2106 (1992).

24. A. Castagna and N. S. Stoloff, Scr. Metall., vol. 26, pp. 673-678 (1992).

25. C. G. McKamey and D. H. Pierce, Scr. Metall., vol. 28, pp. 1173-1176 (1993).

26. V. Viswanathan, B. R. Shelton, J. K. Wright and V. K. Sikka, Scr. Metall., vol. 29, pp. 589-594 (1993).

27. C. T. Liu, C. L. White and J. A. Horton, Acta Metall., vol. 33, pp. 213-229 (1985).

28. D. J. Gaydosh and M. V. Nathal, Scripta Metall., vol. 24, pp. 1281-1284 (1990).

29. C. T. Liu and E. P. George, Scripta Metall., vol. 24, pp. 1285-1290 (1990).

30. J. A. Horton, C. T. Liu and C. C. Koch, in High Temperature Alloys: Theory and Design J. O. Stiegler, Ed. (TMS/AIME, Warrendale PA, 1984) pp. 309-321.

31. D. J. Gaydosh, S. L. Draper and M. V. Nathal, Met. Trans. A, vol. 20A, pp. 1701-1714 (1989).

32. C. G. McKamey, P. J. Maziasz, G. M. Goodwin and T. Zacharia, Mater. Sci. Eng., vol. 174, pp. 59-70 (1994).

33. R. S. Diehm and D. E. Mikkola, in High Temperature Ordered Intermetallics II N. S. Stoloff, C. C. Koch, C. T. Liu, O. Izumi, Eds. (MRS Symp. Proc., Pittsburgh, Pa, 1987), vol. 81, pp. 329-334.

34. D. M. Dimiduk, M. G. Mendiratta, D. Banerjee and H. A. Lipsitt, Acta Metall., vol. 36, pp. 2947-2958 (1988).

35. R. T. Fortnum and D. E. Mikkola, Mat. Sci. Eng., vol. 91, pp. 223-231 (1987).

36. H. P. Longworth and D. E. Mikkola, Mat. Sci. Eng., vol. 96, pp. 213-229 (1987).

37. C. G. McKamey, J. H. DeVan, P. F. Tortorelli and V. K. Sikka, J. Mater. Res., vol. 6, pp. 1779-1805 (1991).

38. P. J. Maziasz and C. G. McKamey, Mater. Sci. Eng., vol. A152, pp. 322-334 (1992).

39. C. G. McKamey, J. A. Horton and C. T. Liu, Scr. Metall., vol. 22, pp. 1679-1681 (1988).

40. D. G. Morris, M. M. Dadras and M. A. Morris, Acta. Metall. Mater., vol. 41, pp. 97-111 (1993).

41. P. R. Munroe and I. Baker, J. Mater. Sci., vol. 28, pp. 2299-2303 (1993).

42. R. Balasubramaniam, Scripta Mater., vol. 34, pp. 127-133 (1996).

43. A. Agarwal and R. Balasubramaniam, Bulletin of Mater. Sci., vol. 19, pp. 91-102 (1996).

44. J. H. Zhu, S. B. Huang and X. J. Wan, Scri. Metall., vol. 32, pp. 1399-1404 (1995).

45. Y. Liu, T. Takasugi, O. Izumi and T. Yamada, Acta Metall., vol. 37, pp. 507-517 (1989).

46. A. Castagna and N. S. Stoloff, Mat. Sci. & Eng., vol. A192/193, pp. 399-406 (1995).

47. C. G. McKamey and E. H. Lee, in High-Temperature Ordered Intermetallic Alloys V I. Baker, R. Darolia, J. D. Whittenberger, M. H. Yoo, Eds. (MRS Symp. Proc., Pittspurgh, Pa, 1993), vol. 288, pp. 983-988.

48. D. B. Kasul and L. A. Heldt, Met. Trans. A, vol. 25A, pp. 1285-1290 (1994).

49. R. J. Lynch, L. A. Heldt and W. W. Milligan, Scripta Metall., vol. 25, pp. 2147-2151 (1991).

50. R. J. Lynch and L. A. Heldt, in Processing, Properties, and Applications of Iron Aluminides J. H. Schneibel, M. A. Crimp, Eds. (TMS, Warrendale, PA, 1994) pp. 287-300.

51. D. B. Kasul and L. A. Heldt, Scripta Metall., vol. 25, pp. 1047-1051 (1991).

52. D. A. Alven, . (Rensselaer Polytechnic Institute, unpublished work, 1996),

53. R. J. Lynch, W. W. Milligan and L. A. Heldt, in Parkins Symposium on Fundamental Aspects of Stress Corrosion Cracking S. M. Bruemmer, E. I. Meletis, R. H. Jones, W. W. Gerberich, F. P. Ford, R. W. Staehle, Eds. (TMS, Warrendale PA, 1992) pp. 117-130.

54. G. Camus, D. J. Duquette and N. S. Stoloff, J. Mater. Res., vol. 5B, pp. 950 (1990).

55. A. K. Kuruvilla, Ph.D. Thesis, Rensselaer Polytechnic Institute (1985).

56. T. Takasugi and O. Izumi, Scripta Metall., vol. 19, pp. 903-907 (1985).

57. T. Takasugi and O. Izumi, Acta Metall., vol. 34, pp. 607-618 (1986).

58. X. J. Wan, J. H. Zhu and K. L. Jing, Scripta Metall., vol. 26, pp. 473-477 (1992).

59. X. J. Wan, J. H. Zhu and K. L. Jing, Scripta Metall., vol. 26, pp. 479-484 (1992).

60. A. K. Kuruvilla and N. S. Stoloff, Scripta Metall., vol. 19, pp. 83-87 (1985).

61. E. P. George, C. T. Liu and D. P. Pope, Scripta Metall., vol. 30, pp. 37-42 (1994).

62. A. K. Kuruvilla and N. S. Stoloff, Met. Trans. A, vol. 16A, pp. 815-820 (1985).

63. A. Castagna, Ph.D. Thesis, Rensselaer Polytechnic Institute (1995).

64. H. J. Gudladt and J. Petit, Scripta Metall., vol. 25, pp. 2507-2512 (1991).

65. P. J. Cotterill and J. E. King, Int. J. Fatigue, vol. 13, pp. 447-452 (1991).

66. J. D. Landes and R. P. Wei, J. Eng. Mater. Tech., vol. 93, pp. 2-9 (1973).

67. B. A. Graville, R. G. Baker and F. Watkinson, Brit. Weld. J., vol. 14, pp. 337-342 (1967).

68. J. K. Tien and R. J. Richards, Scripta Metall., vol. 9, pp. 1097-1101 (1975).

69. G. S. Ansell and R. M. Vennet, Hydrogen Embrittlement, Contract Report # AT (30-1)-3479 (1968).

70. R. E. Ricker and D. J. Duquette, Met. Trans. A, vol. 19A, pp. 1775-1783 (1988).

71. C. Zapffe and C. Simms, Trans. AIME, vol. 145, pp. 225 (1941).

72. A. S. Tetelman, Fundamental Aspects of Stress Corosion Cracking, Fundamental Aspects of Stress Corosion Cracking (NACE, 1969), pp. 446.

73. R. A. Oriani and P. H. Josephic, Acta Metall., vol. 22, pp. 1065 (1974).

74. N. J. Petch, Phil. Mag., vol. 1, pp. 331 (1956).

75. R. P. Gangloff and R. P. Wei, Met. Trans., vol. 8A, pp. 1043 (1977).

76. J. G. Morlet, H. H. Johnson and A. R. Troiano, J. Iron and Steel Inst., vol. 189, pp. 37-44 (1958).

77. R. O. Oriani and P. H. Josephic, Acta Metall., vol. 25, pp. 979 (1977).

78. H. K. Birnbaum, in Hydrogen Effects on Material Behavior N. R. Moody, A. W. Thompson, Eds. (TMS, Warrendale, PA, 1990) pp. 639-658.

79. H. H. Uhlig and R. W. Revie, Corrosion and Corrosion Control, (John Wiley and Sons, New york, 1985).

80. N. Masahashi, T. Takasugi and O. Izumi, Acta Metall., vol. 36, pp. 1823-1836 (1988).

81. J. J. Scott, M.S. Thesis, Rensselaer Polytechnic Institute (1992).

82. A. Shan and D. Lin, Scr. Metall., vol. 27, pp. 95-99 (1992).

83. H. K. Birnbaum and H. Wadley, Scripta Metall., vol. 9, pp. 1113 (1975).

84. A. J. McEvily and R. C. Boettner, Acta Metall., vol. 11, pp. 725-743 (1963).

85. B. H. Kear, Acta Metall., vol. 12, pp. 555-569 (1964).

86. R. C. Boettner, N. S. Stoloff and R. G. Davies, Trans. AIME, vol. 236, pp. 131-133 (1966).

87. A. J. McEvily and R. P. Wei, in Corrosion-Fatigue: Chemistry, Mechanics, and Microstructure O. F. Devereux, A. J. McEvily, R. W. Staehle, Eds. (NACE, Houston, 1972), vol. NACE-2, pp. 381-395.

88. R. P. Wei, Int. J. of Fract., vol. 4, pp. 159-170 (1968).

89. R. P. Wei, Eng. Fract. Mech., vol. 1, pp. 633-657 (1970).

90. ASTM, in 1993 Annual Book of ASTM Standards(ASTM, Philadelphia, Pa., 1993), vol. 03.01, pp. 569-596.

91. G. R. Irwin, Eng. Fract. Mech., vol. 1, pp. 241-257 (1968).

92. P. S. Pao, S. J. Gill, C. R. Feng and D. J. Michel, Mat. Sci. Eng., vol. A153, pp. 532-537 (1992).

93. M. N. James and J. F. Knott, Scripta Metall., vol. 19, pp. 189 (1985).

94. J. E. King, Fatigue Eng. Mater. Struct., vol. 5, pp. 177 (1982).

95. J. E. King and P. J. Cotterill, Mat. Sci. Eng., vol. 6, pp. 19-31 (1990).

96. B. G. Pound, Acta Metall. Mater., vol. 38, pp. 2373-2381 (1990).

97. B. G. Pound, Acta Metall. Mater., vol. 42, pp. 1551-1559 (1994).

98. P. Y. Hou and J. Stringer, Mater. Sci. Eng., vol. 202, pp. 1-10 (1995).

99. A. M. Huntz, Mat. Sci. Eng., vol. 87, pp. 251-260 (1987).

100. J. Stringer, Mater. Sci. Eng., vol. 120, pp. 129-137 (1989).

101. J. Albrecht, I. M. Bernstein and A. W. Thompson, Met. Trans. A, vol. 13A, pp. 811-820 (1982).

102. M. R. Louthan, G. R. Caskey, J. A. Donovan and D. E. Rawl, Mat. Sci. Eng., vol. 10, pp. 357 (1972).

103. J. K. Tien, A. W. Thompson, I. M. Bernstein and R. J. Richards, Metall. Trans. A, vol. 7A, pp. 821-829 (1976).

104. H. J. Roven and E. Nes, Acta Metall., vol. 39, pp. 1735-1754 (1991).

105. P. J. Cotterill and J. F. Knott, Acta Metall., vol. 40, pp. 2753-2764 (1992).

106. V. K. Sikka, . (Oak Ridge National Laboratory, unpublished work, 1996),

NEW ALLOYS DISTRIBUTION

AIR PRODUCTS AND CHEMICALS
P.O. Box 538
Allentown, PA 18105
S. W. Dean

ALBERTA RESEARCH COUNCIL
Oil Sands Research Department
P.O. Box 8330, Postal Station F
Edmonton, Alberta
Canada T6H5X2
L. G. S. Gray

ALLISON GAS TURBINE DIVISION
P.O. Box 420
Indianapolis, IN 46206-0420
P. Khandelwal (Speed Code W-5)
R. A. Wenglarz (Speed Code W-16)

AMAX R&D CENTER
5950 McIntyre Street
Golden, CO 80403
T. B. Cox

ARGONNE NATIONAL LABORATORY
9700 S. Cass Avenue
Argonne, IL 60439
W. A. Ellingson

ARGONNE NATIONAL LABORATORY-WEST
P.O. Box 2528
Idaho Falls, ID 83403-2528
S. P. Henslee

BABCOCK & WILCOX
Domestic Fossil Operations
20 South Van Buren Avenue
Barberton, OH 44023
M. Gold

BETHLEHEM STEEL CORPORATION
Homer Research Laboratory
Bethlehem, PA 18016
B. L. Bramfitt
J. M. Chilton

BRITISH COAL CORPORATION
Coal Technology Development Division
Stoke Orchard, Cheltenham
Glocestershire, England GL52 4ZG
J. Oakey

CANADA CENTER FOR MINERAL & ENERGY TECHNOLOGY
568 Booth Street
Ottawa, Ontario
Canada K1A OG1
R. Winston Revie
Mahi Sahoo

COLORADO SCHOOL OF MINES
Department of Metallurgical Engineering
Golden, CO 80401
G. R. Edwards

DOE
DOE OAK RIDGE OPERATIONS
P. O. Box 2008
Building 4500N, MS 6269
Oak Ridge, TN 37831
M. H. Rawlins

DOE
DOE OAK RIDGE OPERATIONS
P. O. Box 2001
Oak Ridge, TN 37831
Assistant Manager for
Energy Research and Development

DOE
Federal Energy Technology Center
3610 Collins Ferry Road
P.O. Box 880
Morgantown, WV 26507-0880
D. C. Cicero
F. W. Crouse, Jr.
R. A. Dennis
N. T. Holcombe
W. J. Huber
T. J. McMahon
J. E. Notestein

DOE
OFFICE OF FOSSIL ENERGY
FE-72
19901 Germantown Road
Germantown, MD 20874-1290
F. M. Glaser

DOE
OFFICE OF BASIC ENERGY SCIENCES
Materials Sciences Division
ER-131 GTN
Washington, DC 20545
H. M. Kerch

DOE
Federal Energy Technology Center
626 Cochrans Mill Road
P.O. Box 10940
Pittsburgh, PA 15236-0940
A. L. Baldwin
G. V. McGurl
L. A. Ruth
T. M. Torkos

EC TECHNOLOGIES INC.
3614 Highpoint Drive
San Antonio, TX 78217
D. J. Kenton

ELECTRIC POWER RESEARCH INSTITUTE
P.O. Box 10412
3412 Hillview Avenue
Palo Alto, CA 94303
W. T. Bakker
J. Stringer

EUROPEAN COMMUNITIES JOINT RESEARCH CENTRE
Petten Establishment
P.O. Box 2
1755 ZG Petten
The Netherlands
M. Van de Voorde

FOSTER WHEELER DEVELOPMENT CORPORATION
Materials Technology Department
John Blizard Research Center
12 Peach Tree Hill Road
Livingston, NJ 07039
J. L. Blough

IDAHO NATIONAL ENGINEERING LABORATORY
P.O. Box 1625
Idaho Falls, ID 83415
A. B. Denison
R. N. Wright

LAWRENCE BERKELEY LABORATORY
University of California
Berkeley, CA 94720
Ian Brown

LAWRENCE LIVERMORE NATIONAL LABORATORY
P.O. Box 808, L-325
Livermore, CA 94550
W. A. Steele

LEHIGH UNIVERSITY
Materials Science & Engineering
Whitaker Laboratory
5 E. Packer Avenue
Bethlehem, PA 18015
J. N. DuPont

NATIONAL MATERIALS ADVISORY BOARD
National Research Council
2101 Constitution Avenue
Washington, DC 20418
K. M. Zwilsky

OAK RIDGE NATIONAL LABORATORY
P.O. Box 2008
Oak Ridge, TN 37831
P. T. Carlson
G. M. Goodwin
F. D. Johnson **(4 copies)**
R. R. Judkins
C. T. Liu
C. G. McKamey
J. H. Schneibel
V. K. Sikka
R. W. Swindeman
P. F. Tortorelli
M. R. Upton
I. G. Wright

PACIFIC NORTHWEST LABORATORY
P. O. Box 999, K3-59
Battelle Boulevard
Richland, WA 99352
R. N. Johnson

SHELL DEVELOPMENT COMPANY
WTC R-1371
P.O. Box 1380
Houston, TX 77251-1380
W. C. Fort

THE JOHNS HOPKINS UNIVERSITY
Materials Science & Engineering
Maryland Hall
Baltimore, MD 21218
R. E. Green, Jr.

THE MATERIALS PROPERTIES COUNCIL, INC.
United Engineering Center
345 E. Forty-Seventh Street
New York, NY 10017
M. Prager

THE TORRINGTON COMPANY
Advanced Technology Center
59 Field Street
Torrington, CT 06790
W. J. Chmura

UNION CARBIDE CORPORATION
Linde Division
P.O. Box 44
175 East Park Drive
Tonawanda, NY 14151-0044
Harry Cheung

UNIVERSITY OF WASHINGTON
Department of Materials Science
and Engineering
101 Wilson, FB-10
Seattle, WA 98195
T. G. Stoebe

UNIVERSITY OF TENNESSEE AT
KNOXVILLE
Materials Science and Engineering
Department
Knoxville, TN 37996
P. Liaw
C. D. Lundin

WEST VIRGINIA UNIVERSITY
Department of Physics
Morgantown, WV 26506-6315
B. R. Cooper

WESTERN RESEARCH INSTITUTE
365 N. 9th Street
P.O. Box 3395
University Station
Laramie, WY 82071
V. K. Sethi